4-3-2015

Control and Integration Strategies for Bidirectional and Unidirectional Converters in Residential Distributed Power Systems

Sung Min Park
goobota@gmail.com

Control and Integration Strategies for Bidirectional and Unidirectional Converters in Residential Distributed Power Systems

Sung Min Park, PhD

University of Connecticut, 2015

Reactive power compensation is important not only for power system stability but also efficient use of the power transmitted through the electric grid. Although many power electronics-based technologies such as flexible alternating current transmission systems and active power filters have emerged to overcome the shortcomings of traditional passive shunt compensation methods, they may not be the best solution for improvement of power quality of an entire power system due to high capital and operating costs, as well as additional inherent power losses.

Usually, unidirectional power factor correction converters are utilized in many commercial applications as front-end circuitry in order to minimize the effects of harmonics distortion and poor power factor. Since these converters are commonly used, they have great potential as huge reactive power compensators in distribution level power systems. However, the distortion of input current as a result of reactive power compensation cannot be avoided due to intrinsic topology limitations. This drawback can be mitigated by employing bidirectional converters which would be incorporated in electric vehicles and photovoltaic systems, which are becoming increasingly available as residential distributed generation systems.

The objective of this dissertation is to investigate reactive power capabilities of aggregated unidirectional converters and to propose cost-effective residential distributed generation systems with maximized local reactive power support capabilities. The proposed

approaches are as follows: 1) to investigate functionalities of unidirectional converters as active power filers, 2) to analyze and design control algorithms for unidirectional and bidirectional converters in residential distributed power systems, and 3) to harmonize unidirectional and bidirectional converters in order to obtain harmonic-free reactive power support. The current distortion of the unidirectional converter under reactive power compensation is analytically explained and the performance of unidirectional converters as an active power filter is evaluated. Power control methods of bidirectional converters in photovoltaic and vehicle-to-grid systems are investigated. Finally, an integration strategy for controlling bidirectional and unidirectional converters is proposed. The outcome of this dissertation is to get free reactive power support using the existing resources without harmonic pollution in residential distributed generation systems.

Control and Integration Strategies for Bidirectional and Unidirectional Converters in Residential Distributed Power Systems

Sung Min Park

B.Eng., Korea University, **2001**

M.Eng., Korea University, **2003**

A Dissertation
Submitted in Partial Fulfillment of the
Requirements for the Degree of

Doctor of Philosophy

at the

University of Connecticut

2015

APPROVAL PAGE

Doctor of Philosophy Dissertation

Control and Integration Strategies for Bidirectional and Unidirectional Converters in Residential Distributed Power Systems

Presented by

Sung Min Park, B.Eng., M.Eng.

Major Advisor _____
Sung-Yeul Park

Associate Advisor_____
Ali M. Bazzi

Associate Advisor _____
Peter B. Luh

University of Connecticut

2015

This page internationally left blank.

To my family

Eunkyung Kwag, Minkun Park, Seoyoon Park

Acknowledgments

I would like to express my sincere appreciation and gratitude to Prof. Sung-Yeul Park for his guidance, support and encouragement throughout my study at the University of Connecticut.

I would also like to thank Prof. Ali Bazzi and Prof. Peter Luh for serving as members of my Ph.D advisory committee, for making valuable comments that helped me make this work better.

My appreciation goes to the former and current colleagues at Smart Energy and Power Electronics Laboratory (SEPEL) and Advanced Power Electronics and Electric Drives Laboratory (APEDL), Tai-Sik Hwang, Xiao Zhou, Matthew Tarca, Yong-Duk Lee, Joshua Ivaldi, Michael Kelley, Jen-Guey Chen, Shawn Maxwell, Dr. Soo-Bin Han, Dr. Joon-Young Choi, Mr. Myung-Geun Lee, Dr. Young-Soo Yoon, Weiqiang Chen, Amruta Kulkarni, Yiqi Liu.

I would also like to give my special thanks to my colleagues in Power Electronics group of United Technologies Research Center (UTRC), Dr. Vladmir Blasko, Dr. Brian McCabe, Dr. Shashank Krishnamurthy and other members of a group for their encouragement and support during my research work.

My thanks are extended to Dr. Krishnan Ramu, Dr. Nimal Lobo and Dr. Hyong-Yeol Yang for their warm encouragement and assistance during my time at Ramu Inc, Blacksburg, VA.

In addition, I wish to specifically emphasize my gratitude for all the help from the Rev. Hojun Chang and church family at Storrs Korean Church.

Importantly, I would like to express the deepest and warmest gratitude to my parents and my parents-in-law and my wonderful lovely wife, Eunkyung Kwag, for their great sacrifices during my study at the University of Connecticut. I also should thank my children, Minkun and Seoyoon, for the special happiness they brought to us.

Table of Contents

List of Figures

List of Tables

Chapter 1. Introduction

1.1 Motivation

Reactive power has long been considered as an element of electric grid control. It should be properly maintained in order to enhance voltage stability and transmission efficiency in ac power systems. Due to voltage fluctuations and power intermittency caused predominantly by poorly controlled reactive power flow, the end user of electric systems in the U.S. suffers from losses of billions of dollars every year [1], [2]. Although many power electronics-based technologies such as flexible alternating current transmission systems and active power filters have emerged to overcome the shortcomings of traditional passive reactive compensation methods, these solutions are limited for improvement of power quality of an entire power system, due to high capital and operating costs, as well as their additional inherent power losses.

The purpose of this dissertation is to investigate reactive power capabilities of existing aggregated unidirectional converters and to propose a cost-effective solution for reactive power compensation through control and integration strategies for unidirectional and bidirectional converters in residential distributed power systems as shown in Figure 1.1. Usually, unidirectional power factor correction converters are utilized in many commercial applications such as laundry machines, air conditioners, and battery chargers as front-end circuitry in order to minimize the effects of harmonic distortion and poor power factor caused by their respective nonlinear loads. Since these converters are ubiquitous, they have great potential as reactive power resources in distribution level power systems if they possess reactive power compensation functionality functionalities. However, the distortion

of input current as a result of reactive power compensation cannot be avoided due to intrinsic topology limitations of unidirectional converters. These harmonic distortions can be mitigated by employing bidirectional converters soon to be available in residential distributed generation systems such as vehicle-to-grid and photovoltaic systems. As a result, free reactive power support without additional costs and harmonic pollutions can be obtained through integration of bidirectional and unidirectional converters. Ultimately, residential power systems will possess the ability to act as large reactive power compensators, resulting in more efficient and stable electric power distribution system.

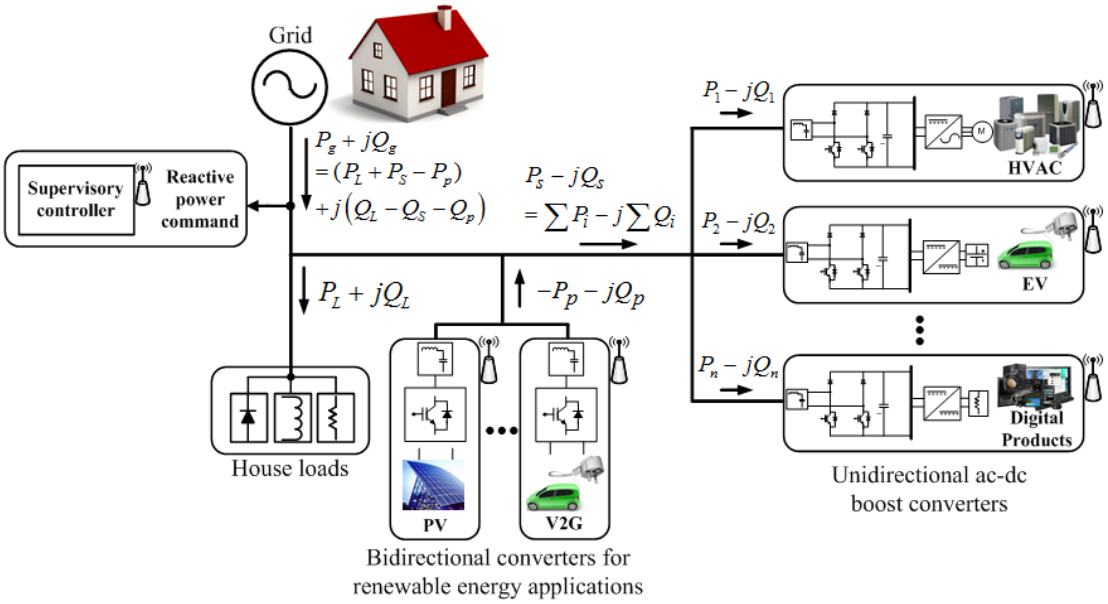

Figure 1.1 Proposed residential distributed power system.

1.2 Overview of the present state of technologies

Traditional reactive power compensation methods include rotating synchronous condensers and fixed or mechanically switched capacitors or inductors. However, there are

limitations in both dynamic and steady-state performance, because these methods use mechanical devices with little or no high-speed controllability. In addition, these mechanical devices cannot be switched frequently due to their low durability. To overcome the demerits of traditional technologies, several power electronics-based technologies have been developed to enhance the controllability and power transfer capability in transmission and distribution systems.

Flexible alternating current transmission systems (FACTS), mostly having high power capacities along with remote VAR transmission, have been studied by industrial and academic researchers since the 1990's [3], [4]. Among these FACTS technologies, the static VAR compensator (SVC), and static synchronous compensator (STATCOM) mainly focus on compensating reactive power by injecting current of a desired phase into the system [5], [6] as shown in Figure 1.2.

Active power filters (APF) shown in Figure 1.3 are another sophisticated compensation method. APFs are configurable with various power stage topologies and have been developed to resolve power quality problems by employing harmonic current compensation (HCC) and reactive power compensation (RPC) [8], [9].

Although SVCs, STATCOMs and APFs have outstanding performance, they may not be the best solution to improve the power quality of an entire power system due to high capital and operating costs related to space and installation, as well as additional inherent power losses. Moreover, a local supply of reactive power from distribution systems or microgrids in response to local voltage signals is more desirable and economical rather than

remote VAR transmission methods, because local reactive power supply can significantly reduce feeder losses [10].

(a) 64 Mvar static VAR compensator

(b) Six 4.5 Mvar static synchronous compensator

Figure 1.2 Flexible alternating current transmission systems [7].

Figure 1.3 Active power filters [11].

To find better economical solutions, the demands of power quality mitigation have continuously encouraged power electronics engineers to include HCC and RPC capabilities in power converters typically used for renewable energy conversion systems such as wind turbines, photovoltaic (PV) and fuel cell systems [12], [13]. These may have HCC and RPC functionalities as ancillary services, usually typical of converters capable of bidirectional power flow. As power converters for renewable energy sources become more popular in ac power systems, the potential for HCC and RPC will greatly increase, as these control schemes can be employed in existing topologies without hardware changes, while simultaneously sending generated energy back to the grid. Despite the increased utility and cost savings, the number of renewable power converters capable of fulfilling these functions is still limited.

Alternatively, vehicle-to-grid (V2G) technology shown in Figure 1.4 has recently emerged for incorporation of electric vehicles into the electric grid as energy storages [14] which can mitigate power quality as an ancillary service. This will result in enhanced reliability and performance of the power system. However, V2G require a bidirectional power converter [15], [16], which increases system cost and complexity compared to that of a unidirectional power converter. For this reason, a unidirectional topology is a preferable configuration for level 1 battery chargers in electric vehicle (EV) and plug-in electric vehicle (PHEV) applications, meant for residential interconnections, whereas V2G utilizing bi-directional converters is more applicable for level 2 battery chargers [17].

Power factor correction (PFC) converters are embedded in the commercial products such as home appliances, EV/PHEV battery chargers, switched mode power supplies to

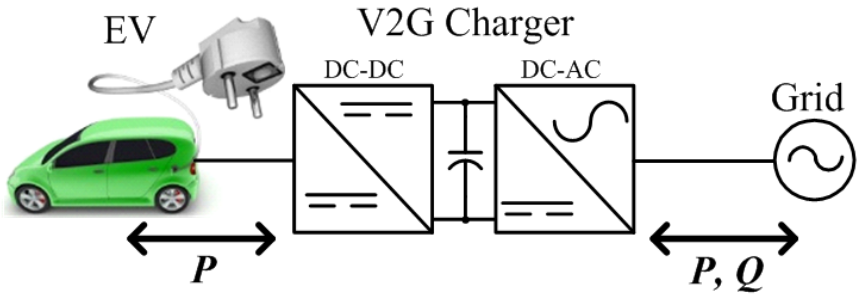

Figure 1.4 Conceptual diagram of vehicle to grid.

regulate the input current to be sinusoidal waveform in phase with the grid voltage in unidirectional power flow capability [18]-[22]. Since numerous unidirectional converters are connected with ac power systems, if we can utilize the reactive power capacity of PFC circuits, then existing unidirectional ac-dc boost converters have great potential to improve substantially the stability of ac power systems.

In recent years, few papers have detailed HCC and RPC functionalities using unidirectional PFC converters in [17], [23], [24]. In [17], battery charger topologies used for EV/PHEV applications have been reviewed for providing reactive power support to the grid, but the RPC capability in unidirectional converters was mentioned briefly and any further analysis was not conducted. In [23], the feasibility of HCC functionality using a boost converter was presented as a low cost solution, but RPC functionality was not considered. In [24], the reactive power support capabilities of the unidirectional converter within V2G applications were studied through simulation results without detailed analysis regarding input current distortions.

1.3 Dissertation outline

Chapter 1 gives the introduction of the research background regarding reactive power compensation methods. The proposed system utilizing the combination of the unidirectional and bidirectional converters can provide cost-effective reactive power compensation method to power systems, so that it will improve overall performance of power system stability and efficiency.

In chapter 2, a brief review of the unidirectional ac-dc converters is presented and typical control method with a voltage feedforward controller is discussed. The input impedance and current (IIC) feedforward control scheme is proposed to improve input power quality under limited bandwidth feedback current controller. Small-signal input admittances are derived and presented and detailed comparisons are carried out and discussed. MATLAB/Simulink simulation results comparing the performance of the three control methods are show and experimental verification of the proposed approach is presented.

In chapter 3, the feasibility and limitations of the unidirectional ac-dc boost PFC converter, when it is employed for active power filter functionalities, are explored. Due to the inherent limitations of the unidirectional ac-dc boost converter, the grid current will be distorted during reactive power compensation. Therefore, an approach for estimating the distortion levels of the current under reactive power compensation modes is analytically justified. MATLAB/Simulink simulation and experimental results are presented in order to validate the proposed approach.

In chapter 4, a brief review of the bidirectional ac-dc converters in PV and V2G applications is presented. The bidirectional converter modeling approach using the averaged state-space and control method to improve the seamless power transfer capability are proposed and investigated in PV applications. Additionally, a simple power control method of a bidirectional power converter is proposed for V2G applications especially utilizing the cycloconverter-type high frequency link converter. The proposed method yields the trigonometric-based current references using the sine and cosine terms of the grid phase from existing PLL algorithms. The amplitudes of these sine and cosine terms are calculated not only for active power control but also reactive power and anti-islanding algorithms, resulting in a reduced number of calculation steps and producing a simpler current reference generator. These advantages allows the use of fixed point digital signal processors rather than high cost, high performance digital signal processors in single phase bi-directional converter applications. The effectiveness of the proposed power control is validated through the experimental results using the cycloconverter-type high frequency linked converter.

In chapter 5, an integration strategy of unidirectional converters and bidirectional converters is proposed in order to provide free reactive power support in residential applications. Through this method, these converters cooperatively generate reactive power locally without polluting the grid. MATLAB/Simulink simulation results describe the performance of the proposed strategy of unidirectional and bidirectional converter control and operations.

Chapter 6 will give a summary followed by contribution to this dissertation.

Chapter 2. Unidirectional converters

2.1 Introduction

Nonlinear loads can be defined when the current is drawn in abrupt short pulses rather than in a smooth sinusoidal manner due to the physical properties of the loads such as adjustable speed drives, electronic lighting ballasts or solid state rectifiers. Thus, the current waveform is non-sinusoidal, and is called “distorted current” [25]. This distorted current can be decomposed into a weighted sum of sinusoids whose frequencies are integer multiples of the fundamental frequency. These component frequencies are called harmonics. Harmonics cause disturbances and interferences to other electric facilities, resulting in malfunction or conductor heating. Therefore, it is desired to reduce these harmonics in distribution power systems.

Conventionally many power electronics applications such as inverter-based motor drives, battery chargers or power supplies necessarily require constant dc energy typically provided by a diode rectifier and bulky electrolytic capacitor. Due to periodical charging and discharging operations of large electrolytic capacitor, however, the ac input current is severely distorted and thus a power factor correction (PFC) circuit is additionally required to meet harmonic regulations which are mandatory in some Asia and European countries. Standard IEC 1000-3-2 [26] and EN 61000-3-2 [27] apply to equipment with a rated current up to 16 Arms to be connected to low voltage distribution power systems. Figure 2.1 shows PFC circuits in commercial products such as air-conditioning systems, battery chargers in EV application and general power supplies.

PFC technology has been applied widely in industrial and commercial products for

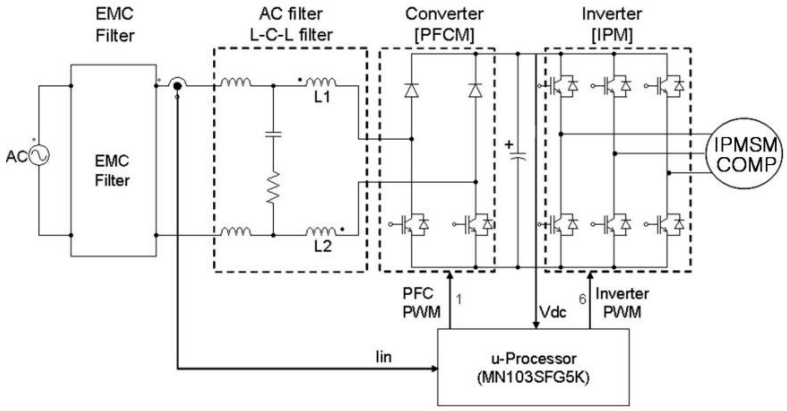

(a) Air-conditioner [28]

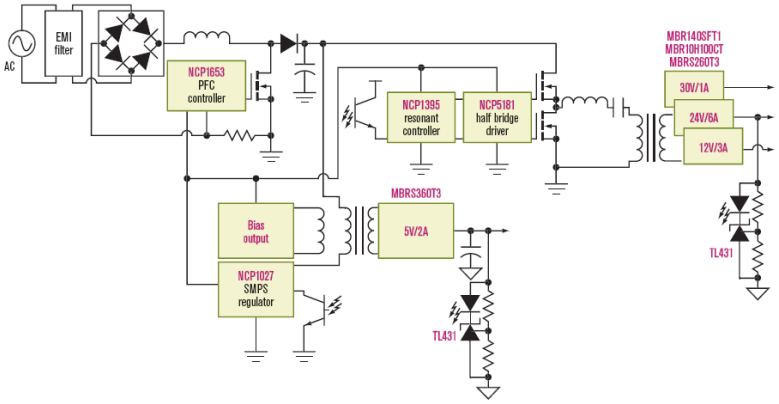

(b) Power supply [29]

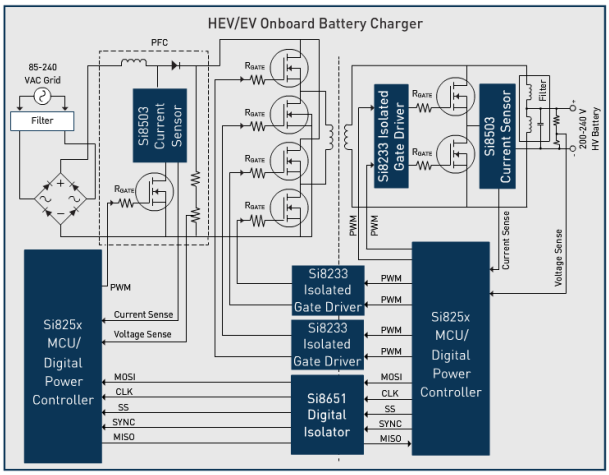

(c) PHEV/EV battery Charger [30]

Figure 2.1 Unidirectional converter applications.

ac-dc power conversion to eliminate input current harmonics. Nevertheless, PFC technology may be considered a mature discipline in terms of high efficiency and high power quality. It can be achieved through advanced circuit topologies and control algorithms by dedicated efforts through an immense amount of research [19], [31], [32].

In general, when converters are designed, there are tradeoffs between high efficiency and high power quality in terms of switching frequency. Higher switching frequency synchronized with the sampling rate yields lower total harmonic distortion (THD) because of the high bandwidth of the current-loop compensator, but the efficiency can be reduced by the increased switching losses. In contrast, low switching frequency may reduce the power quality of the line current. This is caused by the low bandwidth of the current-loop controller but results in lower switching losses. Reducing switching losses while using high switching frequency is fairly restricted by the electrical characteristics of semi-conductors unless a new paradigm of power devices, such as silicon carbide devices are considered [33]. Therefore, it is desirable to use the lowest possible switching frequency to increase the converter efficiency if the low bandwidth current-loop issue is circumvented.

This chapter starts with a brief review of the conventional feedforward control based on input voltage. The proposed IIC feedforward control scheme and small-signal input admittances are derived and presented in Section 2.2. Detailed comparisons of each control method are carried out and briefly discussed in Section 2.3. MATLAB/Simulink simulation results comparing the performance of the three control methods are shown in Section 2.4. Experimental verification of the proposed approach using a 1.2kW dual boost PFC converter is presented in Section 2.5. Finally, Section 2.6 concludes the chapter.

2.2 Control algorithms

A simple control method through nonlinear-carrier (NLC) that allows operation in continuous conduction mode (CCM) without a source voltage sensor has been described in [34]. This approach is more suitable in analog implementations. As extended versions of NLC for digital implementations, digital nonlinear carrier (DNLC) methods have been proposed in [35]-[37]. [35] and [36] used only an instantaneous input current and a proportional gain for controlling the dc-link voltage where the partial switching operation can reduce switching losses in [36] and a low-cost solution using a low-resolution DPWM and low-resolution A/D converters has been proposed in [36]. Also, DNLC with a variable slope ramp has been presented in [37] to reduce complexity of integrated circuit realization. However, these methods excluded the current loop compensation, and might not guarantee stable operation during transients, or protect devices and circuits from overcurrent in unexpected fault conditions.

Predictive current control for single-phase ac-dc boost converters have been presented in [38]-[40]. The desired next duty ratio to yield the current reference can be predicted through calculations based on sensed or observed state if the mathematical model of the system is known. However, as the performance highly depends on circuit parameters which might be sensitive to temperature changes, it requires estimating accurate parameter values under uncertainties.

Leading-phase admittance cancellation (LPAC) techniques have been presented in [41], [42] to improve the current control and to eliminate the leading-phase of line current

through a properly designed admittance compensator without increasing the bandwidth of the current-loop compensator. Nevertheless, these methods considered only leading phase admittance and the complexity of designing admittance compensator makes it less attractive.

The attempts to eliminate zero-crossing distortion of input current through voltage feedforward control methods have been suggested in [28], [43]-[46]. A voltage feedforward duty ratio signal is adopted to effectively produce an average switch voltage over a switching cycle, hence reducing the control proportions of a regular feedback current-loop compensator [43]. Based on [43], [44] employs the full feedforward control signal consisting of the instantaneous line voltage and the derivative of the reference current. Sensorless control methods of PFC without input voltage and current sensors have been presented in [28], [45] and the plug-in repetitive control scheme was investigated in [46] under the voltage feedforward control method. However, these methods might not accomplish unity power factor due to lagging-phase admittances if the current-loop compensator does not have enough bandwidth. Recently, many papers tend to focus on low-cost PFC solutions through usage of low-performance controller and elimination of sensors such as current [47]-[49] and voltage sensors [50], [51] rather than improving input power quality.

Most control methods reported in the literature for improving input current quality have focused on the compensation methods for leading-phase effects with a well-regulated current compensator in spite of the advent of lagging-phase admittances in some conditions where low switching frequency is used in high-line frequency.

This chapter proposes an input impedance and current (IIC) feedforward control method. It employs a simple modification of the conventional voltage feedforward control method which is popularly used in PFC applications. The dual boost PFC converter is utilized to reduce conduction losses [22], [28], [52]-[53] while the proposed method also reduces switching losses with a low bandwidth current-loop compensator. By applying the IIC feedforward control scheme, the proposed feedforward signal can cancel undesirable leading phase admittances as well as lagging- phase admittances, even with a low bandwidth current-loop compensator. Thus, it provides more applicable solutions for ac-dc boost converters in low switching sampling frequency and high-line frequency applications.

2.2.1 Voltage feedforward

A. Derivation of the conventional voltage feedforward control

The conventional voltage feedforward control method has been discussed in [28], [43]-[46] and has been used as a standard practice to improve input power quality of converters in digital implementations. From the dual boost converter, as shown in Figure 2.2 and Figure 2.3, with an input inductor, L, and its parasitic resistor, R, Kirchhoff's voltage law with the source voltage, v_s, the switch voltage, v_d and the input line current, i_s, yields,

$$v_s = Ri_s + L\frac{di_s}{dt} + v_d \tag{2.1}$$

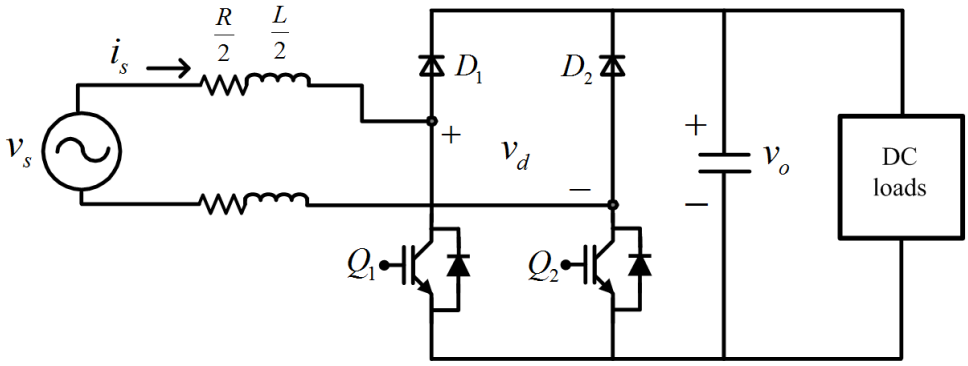

Figure 2.2 Dual boost PFC converter.

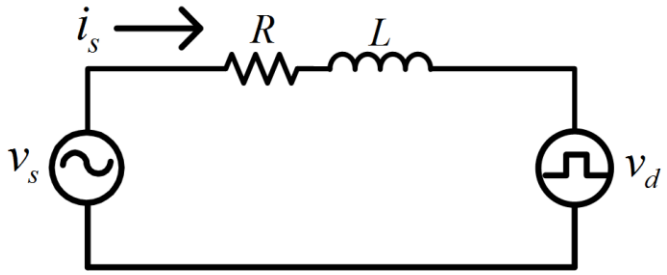

Figure 2.3 Simplified circuit of a dual boost PFC converter.

where v_d is the only active control variable in the circuit. The switch voltage is always a major factor in determining the waveform of the input current. In other words, when producing a sinusoidal input current, the switch voltage has to emulate the source voltage identically, with the exact phase difference due to input impedance. The average switch voltage over a switching cycle at a positive source voltage in CCM, can be expressed as

$$v_d = (1-d)v_o \tag{2.2}$$

where, d is the average on-time duty ratio of the switches and v_o is the dc output voltage shown in Figure 1. Combining (2.1) and (2.2), and rearranging in terms of d, the duty ratio equation can be obtained as

$$d = \underbrace{\frac{1}{v_o}\left(Ri_s + L\frac{di_s}{dt}\right)}_{d_{FB}} + \underbrace{\left(1 - \frac{v_s}{v_o}\right)}_{d_{FF}} \tag{2.3}$$

Theoretically, the duty ratio in (2.3) should be generated for the ideal switch voltage as accurately as possible through adequate converter compensators to yield pure sinusoidal input current. Under the assumption that the phase difference by the input impedance is relatively small, the two voltage waveforms should be almost identical [43]. However, this assumption may lead to lagging-phase shift problems of the input current if a large inductance and a low bandwidth current-loop compensator are employed at a high-line frequency.

B. Problems in low switching and high-line frequency applications

The duty ratio, d of the system in (2.3) consists of the feedback duty ratio d_{FB} and the feedforward duty ratio d_{FF}. d_{FB} contributes to the generation of the exact phase difference between the source voltage and the average switch voltage, which can be obtained through a simple proportional-integral (PI) compensator. d_{FF} produces the inverse of the source voltage waveform as the average switch voltage. If the feedforward controller is not used, the compensator is heavily burdened with producing the total duty value ($d_{FB} + d_{FF}$) in (2.3) and the system will require a high bandwidth compensator.

Figure 2.4 asserts that the phase difference between v_s and v_d (not shown but represented with d as shown in (2.2) and (2.3)), becomes significantly larger when the boost inductance and line frequency increase. It is necessary that d_{FB} is more accurately generated as the feedback controller's contribution increases.

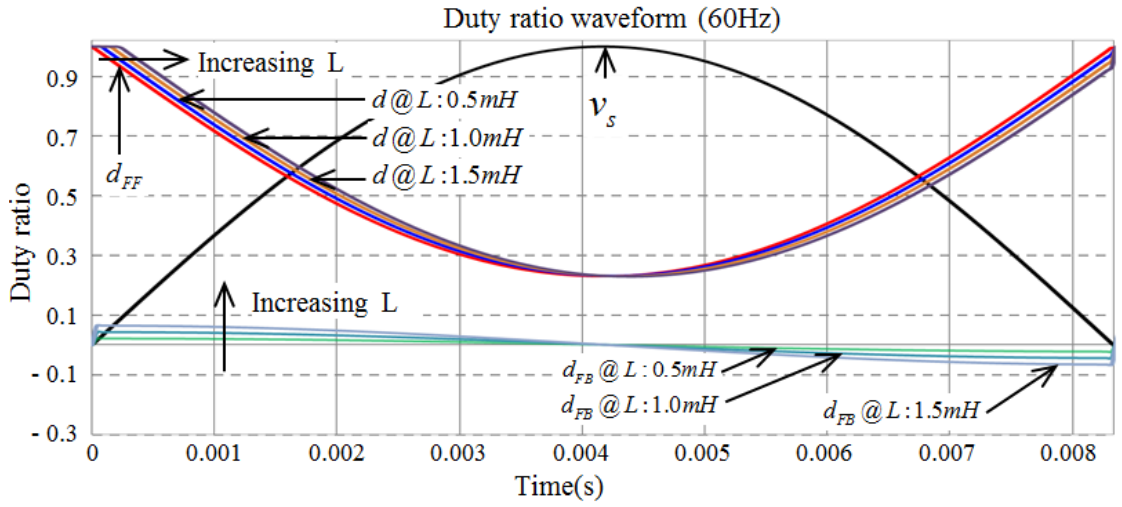

(a) Line frequency-60Hz

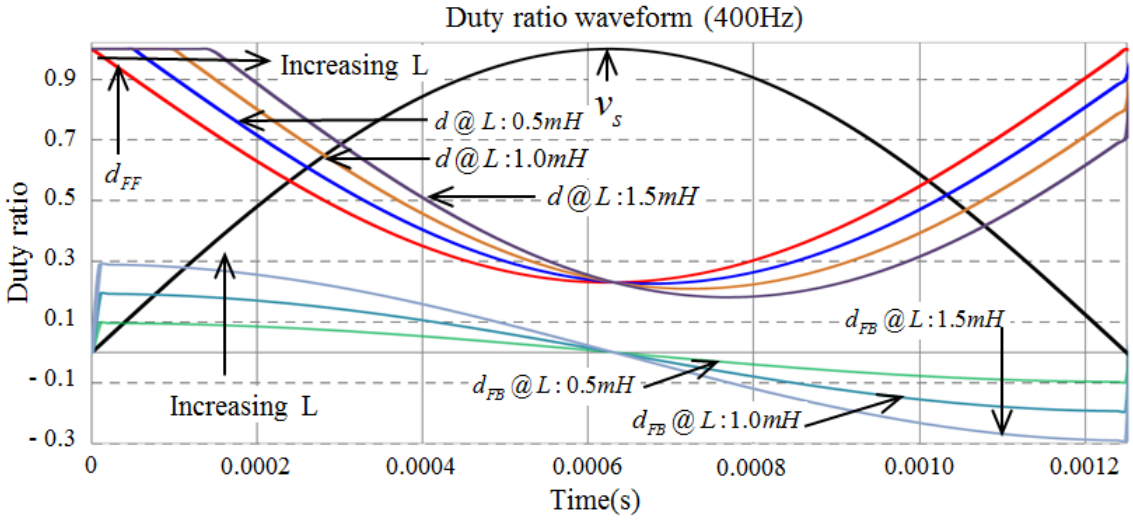

(b) Line frequency-400Hz

Figure 2.4 Duty waveforms of feedback and feedforward controllers.

If the limited current-loop compensator yielding d_{FB} compensates the phase difference incompletely, then this condition causes lagging-phase input admittance. Finally, this may yield undesired input current distortion and displacement of phase. [41]-[44] focused mainly on ameliorating distortions of input admittances in the leading-phase region caused by dynamics of the current-loop and they did not mention the issue of lagging phase caused by the boost inductor and the limited bandwidth current-loop compensator. The lagging region addressed in [41]-[44], [46] was located at the high frequency range from 3 kHz to 10 kHz, and did not cause an issue due to high bandwidth of the current-loop compensator and low input inductance.

In the conventional voltage feedforward scheme, (2.3) indicates that d_{FF} does not exhibit compensator terms to reduce lagging-phase effects, and remains unchanged regardless of leading or lagging input current because d_{FF} is related to the input and output voltages. The conventional scheme depends on only the performance of the current-loop compensator to eliminate lagging-phase effects. As a result, the converter encounters a non-unity power factor if the bandwidth of the current-loop compensator is limited.

2.2.2 Current feedforward

The proposed IIC feedforward control method is based on surveying the phase information of the input current to know whether it is lagging or leading with respect to the source voltage. Combining simple current control law and conventional voltage feedforward control duty, a new feedforward control signal can be expressed under the assumption that the power factor value is unity [35], [36], [54].

$$d_{IIC} = 1 - \frac{v_s}{v_o} = 1 - \frac{1}{G_e \cdot v_o} \cdot i_s = 1 - \frac{v_{s,rms}^2}{P_{in} \cdot v_o} \cdot i_s \tag{2.4}$$

where, $G_e = \frac{i_s}{v_s} = \frac{P_{in}}{v_{s,rms}^2}$

G_e is the emulated input admittance, $v_{s,rms}$ is the *RMS* value of source voltage, and P_{in} is the input power of the PFC rectifying stage. Furthermore, the input power can be expressed in terms of *RMS* values of the source voltage and input current $i_{s,rms}$ as

$$P_{in} = v_{s,rms} \cdot i_{s,rms} \tag{2.5}$$

By combining (2.4) and (2.5), the proposed IIC feedforward duty equation can be obtained as

$$d_{IIC} = 1 - \frac{v_{s,rms}}{i_{s,rms} \cdot v_o} \cdot i_s \tag{2.6}$$

To exemplify how significantly the proposed feedforward controller reduces the control portion of the feedback controller, the duty ratio equations can be compared in the Laplace domain. Taking the Laplace transform of the source voltage and input current

$$v_s(s) = V_s \frac{\omega}{s^2 + \omega^2} \tag{2.7}$$

$$i_s(s) = I_s \frac{\omega \cos\phi + s \sin\phi}{s^2 + \omega^2} \tag{2.8}$$

where, V_s and I_s are the peak magnitude values and ω is the line angular frequency and ϕ is the phase difference between the source voltage and input current. Using (2.3), (2.7) and

(2.8), the duty ratio using the conventional voltage feedforward term can be written in (2.9). In a similar manner, the duty ratio using the proposed IIC feedforward term can be written in (2.10).

$$d_{FB}(s)+d_{FF}(s) = \frac{(I_s L\sin\phi)s^3+(v_o+I_s R\sin\phi+I_s\omega L\cos\phi)s^2+(I_s\omega R\cos\phi-V_s\omega)s+v_o\omega^2}{v_o s^3+(v_o\omega^2)s} \quad (2.9)$$

$$d_{FB}(s)+d_{IIC}(s) = \frac{(I_s L\sin\phi)s^3+(v_o-V_s\sin\phi+I_s R\sin\phi+I_s\omega L\cos\phi)s^2+(I_s\omega R\cos\phi-V_s\omega\cos\phi)s+v_o\omega^2}{v_o s^3+(v_o\omega^2)s} \quad (2.10)$$

The feedback duty portions of the total duty for the two feedforward methods can be defined as

$$\rho_{VF}(s)=\frac{d_{FB}(s)}{d_{FB}(s)+d_{FF}(s)} \quad (2.11)$$

$$\rho_{IIC}(s)=\frac{d_{FB}(s)}{d_{FB}(s)+d_{IIC}(s)} \quad (2.12)$$

where $\rho_{VF}(s)$ is the feedback duty portions of the total duty with the conventional voltage feedforward and $\rho_{IIC}(s)$ is the feedback duty portions of the total duty with the proposed IIC feedforward. Using (2.9)-(2.12), (2.11) and (2.12) can be rewritten as in (2.13) and (2.14).

$$\rho_{VF}(s)=\frac{(I_s L\sin\phi)s^3+(I_s R\sin\phi+I_s\omega L\cos\phi)s^2+(I_s\omega R\cos\phi)s}{(I_s L\sin\phi)s^3+(v_o+I_s R\sin\phi+I_s\omega L\cos\phi)s^2+(I_s\omega R\cos\phi-V_s\omega)s+v_o\omega^2} \quad (2.13)$$

$$\rho_{IIC}(s) = \frac{(I_s L \sin\phi)s^3 + (I_s R \sin\phi + I_s \omega L \cos\phi)s^2 + (I_s \omega R \cos\phi)s}{(I_s L \sin\phi)s^3 + (v_o - V_s \sin\phi + I_s R \sin\phi + I_s \omega L \cos\phi)s^2 + (I_s \omega R \cos\phi - V_s \omega \cos\phi)s + v_o \omega^2} \quad (2.14)$$

If a high-bandwidth current-loop compensator is implemented, the phase difference ϕ is zero. As a result, both (2.13) and (2.14) are identical. Otherwise, ϕ is nonzero and both (2.13) and (2.14) behave differently.

Figure 2.5(a) shows the Bode plot generated at ϕ=0º for (2.13) and (2.14) which are the same when ϕ=0º. The feedback duty portion at a line frequency of 60Hz increases from 2% to 5% as the boost inductance increases from 0.5mH to 1.5mH, whereas this value at 400Hz increases from 13% to 34%. In reference to Figure 2.4, the phase shift of the feedback duty portion is almost 90º at 60Hz, and less than 90º at 400Hz. Figure 2.5(b) shows a reference value from Figure 2.5(a) at ϕ=0º in addition to ϕ=-30º for (2.13) and (2.14) at 60Hz and 400Hz. It is important to note to characteristics in Figure 2.5(b): 1) The phase of (2.14) in the proposed IIC feedforward method remains unchanged with the phase of the reference, but the phase of (2.13) in the conventional voltage feedforward method becomes greater than the ideal value; and 2) The magnitude of (2.14) representing the feedback duty portion to the total duty is lower than one of (2.13), which can be distinguished at 400Hz. As a result, the proposed method reduces the control portion of the compensator compared to the conventional method, indicating that the proposed method is less dependent on the performance of its current-loop compensator.

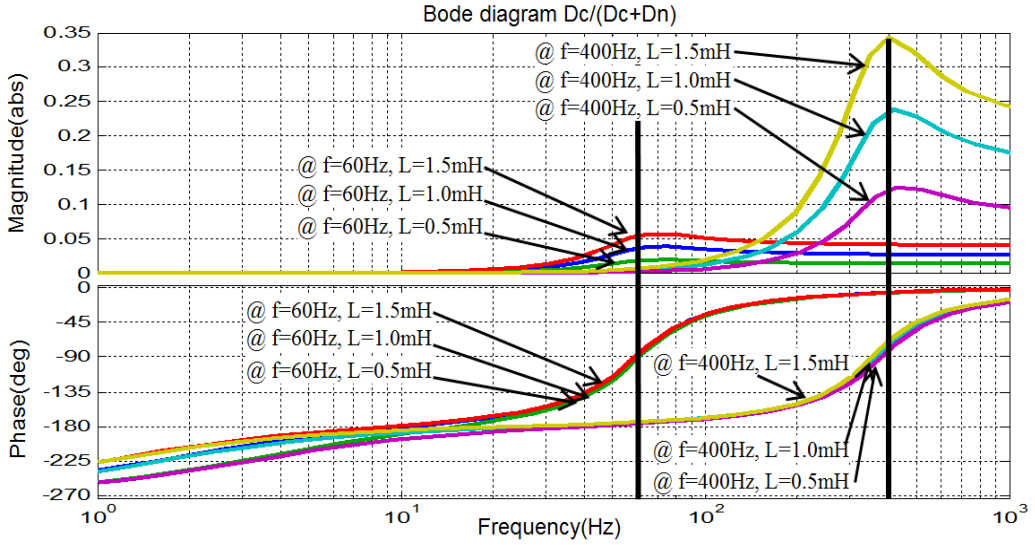

(a) ϕ=0° with different inductor values

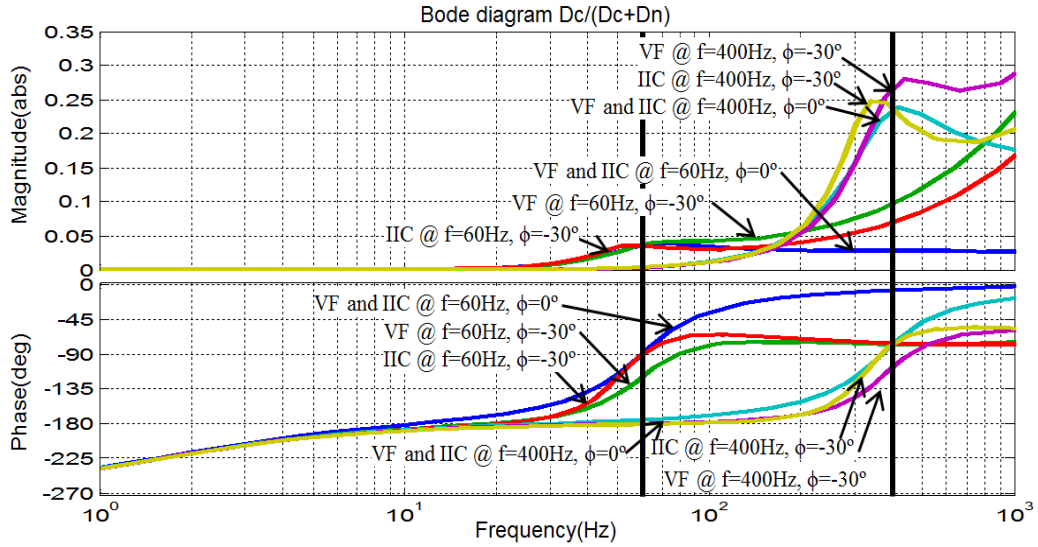

(b) ϕ=-30° with 1.0mH inductor and ϕ=0° as reference value.

Figure 2.5 Feedback duty portion of the total duty.

2.2.3 Input admittances for three control methods

The benefits of the proposed IIC feedforward controller can be also verified by analyzing input admittances in the frequency domain. Recent papers [43], [44], [54] assist to predict the behaviors of input admittances for designing control algorithms. Figure 2.6 depicts the control block diagram including the regular current-loop compensator and the feedforward controller.

Figure 2.7 describes the three control methods; "without any feedforward", "with the conventional voltage feedforward", and "with the proposed IIC feedforward".

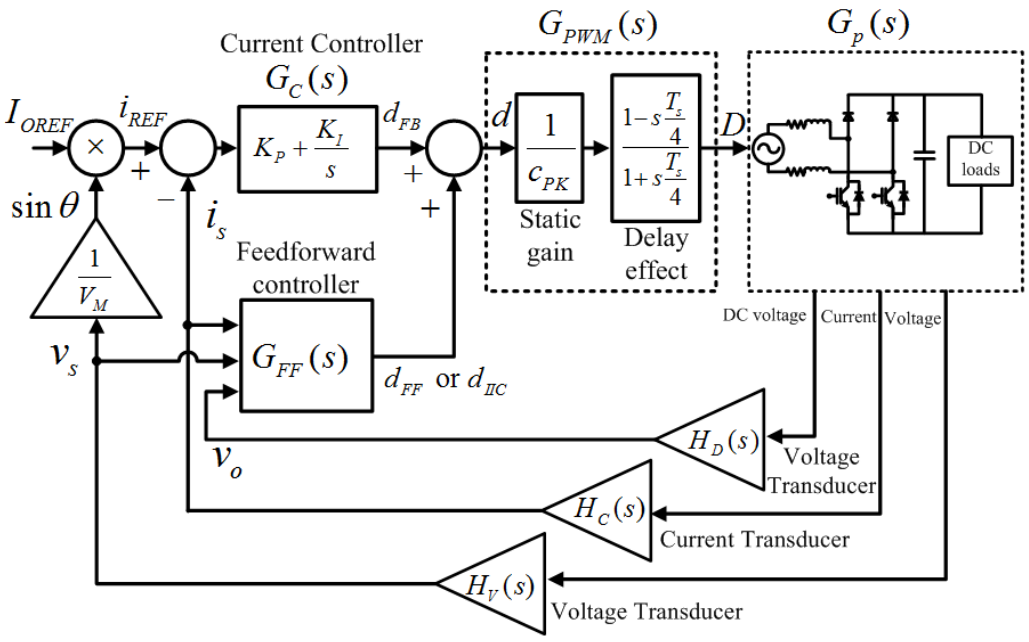

Figure 2.6 Control block diagram with feedforward controllers.

By employing the linearized input admittances, the input current quality can be assessed and the harmonic distortion can be predicted at different input frequency ranges. Using (2.2) in (2.1) and applying small perturbations, the response of the ac-dc boost converter can be expressed as

$$\hat{v}_s(s) = (sL + R)\hat{i}_s(s) + (1 - D)\hat{v}_o(s) + V_o\hat{d}(s) \tag{2.15}$$

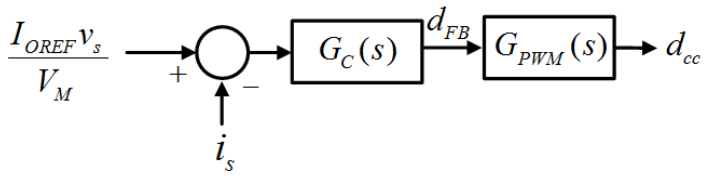

(a) without any feedforward

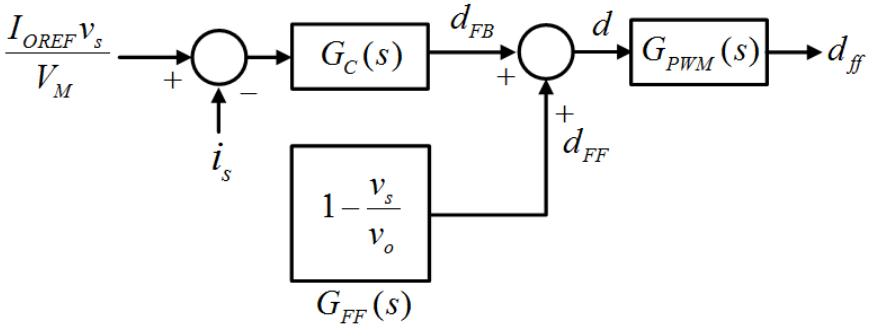

(b) with the conventional voltage feedforward

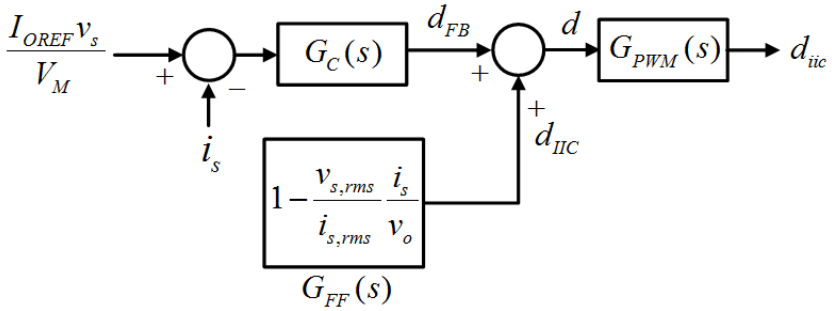

(c) with the proposed IIC feedforward

Figure 2.7 Three control methods.

where the capital letters are values of system variables at a steady-state operating point and hatted lowercase letters are small perturbations from a steady state. The linearized version of the feedback duty $d_{FB}(s)$, the voltage feedforward duty $d_{FF}(s)$ and the proposed IIC feedforward duty $d_{IIC}(s)$ can be obtained as

$$\hat{d}_{FB}(s)=\left(\frac{I_{OREF}}{V_M}\hat{v}_s(s)-\hat{i}_s(s)\right)G_c(s) \tag{2.16}$$

$$\hat{d}_{FF}(s)=\frac{V_s}{V_o}\hat{v}_o(s)-\frac{1}{V_o}\hat{v}_s(s) \tag{2.17}$$

$$\hat{d}_{IIC}(s)=\frac{1}{G_e}\left(\frac{I_s}{V_o}\hat{v}_o(s)-\frac{1}{V_o}\hat{i}_s(s)\right) \tag{2.18}$$

From Figure 2.7, the small-signal transfer functions of the final output duties to three control methods can be obtained as

$$\hat{d}_{cc}(s)=\hat{d}_{FB}(s)\cdot G_{PWM}(s)=\left(\frac{I_{OREF}}{V_M}\hat{v}_s(s)-\hat{i}_s(s)\right)G_c(s)G_{PWM}(s) \tag{2.19}$$

$$\begin{aligned}\hat{d}_{ff}(s)&=\left(\hat{d}_{FB}(s)+\hat{d}_{FF}(s)\right)\cdot G_{PWM}(s)\\&=\left(\left(\frac{I_{OREF}}{V_M}\hat{v}_s(s)-\hat{i}_s(s)\right)G_c(s)+\frac{V_s}{V_o}\hat{v}_o(s)-\frac{1}{V_o}\hat{v}_s(s)\right)G_{PWM}(s)\end{aligned} \tag{2.20}$$

$$\begin{aligned}\hat{d}_{iic}(s)&=\left(\hat{d}_{FB}(s)+\hat{d}_{IIC}(s)\right)\cdot G_{PWM}(s)\\&=\left(\left(\frac{I_{OREF}}{V_M}\hat{v}_s(s)-\hat{i}_s(s)\right)G_c(s)+\frac{1}{G_e}\left(\frac{I_s}{V_o}\hat{v}_o(s)-\frac{1}{V_o}\hat{i}_s(s)\right)\right)G_{PWM}(s)\end{aligned} \tag{2.21}$$

where $\hat{d}_{cc}$(s), $\hat{d}_{ff}$(s) and $\hat{d}_{iic}$(s) are the small-signal duty transfer functions of the ac-dc boost converter with only the regular current-loop compensator, the conventional voltage feedforward duty, and the proposed IIC method, respectively.

The following derivations are performed under the assumption that the output of the dc voltage compensator is constant and the delay from the transducers is small when calculating the input impedance in the high-frequency region. Using (2.19)-(2.21) in the duty term of (2.15), respectively, to eliminate duty terms, the small-signal input admittances of the ac-dc converter using the three control strategies can be obtained as

$$G_{cc}(s)=\frac{\hat{i}_s(s)}{\hat{v}_s(s)}=\frac{1+\dfrac{I_{OREF}V_oG_c(s)G_{PWM}(s)}{V_M}}{sL+R+V_oG_c(s)G_{PWM}(s)} \tag{2.22}$$

$$G_{ff}(s)=\frac{\hat{i}_s(s)}{\hat{v}_s(s)}=\frac{1-G_{PWM}(s)+\dfrac{I_{OREF}V_oG_c(s)G_{PWM}(s)}{V_M}}{sL+R+V_oG_c(s)G_{PWM}(s)} \tag{2.23}$$

$$G_{iic}(s)=\frac{\hat{i}_s(s)}{\hat{v}_s(s)}=\frac{1+\dfrac{I_{OREF}V_oG_c(s)G_{PWM}(s)}{V_M}}{sL+R+V_oG_c(s)G_{PWM}(s)+\dfrac{V_M}{I_{OREF}}G_{PWM}(s)} \tag{2.24}$$

In (2.22)-(2.24), $G_{cc}(s)$, $G_{ff}(s)$, $G_{iic}(s)$ are the small-signal input admittance transfer functions of the ac-dc boost converter with only the regular current-loop compensator, the conventional voltage feedforward duty, and the proposed IIC method, respectively. Furthermore, if the delay influence of the PWM is negligible over frequency ranges of interest and the static gain is unity, $G_{PWM}(s)$ can be modeled as a constant unity gain under average current control. Hence, the small-signal input admittances can be approximated by

$$G_{cc}(s)\approx\frac{1+G_eT(s)}{sL+R+T(s)} \tag{2.25}$$

$$G_{ff}(s) \approx \frac{G_e T(s)}{sL + R + T(s)} \tag{2.26}$$

$$G_{iic}(s) \approx \frac{G_e\left(T(s) + \frac{1}{G_e}\right)}{sL + R + \left(T(s) + \frac{1}{G_e}\right)} \tag{2.27}$$

where, $T(s) = V_o G_c(s) G_{PWM}(s)$, $G_e = \frac{I_{OREF}}{V_M}$

It can be observed in (2.25)-(2.27) that if it is assumed that the impedance of boost inductors is negligible over the low frequency ranges of interest, $G_{cc}(s)$ approaches $1/T(s)+G_e$, which is the leading-phase effect caused by dynamics of the current-loop compensator [54]. $G_{ff}(s)$ and $G_{iic}(s)$ both approach the constant G_e. This implies that they act in a purely resistive manner. For such a reason, higher quality of input current can be obtained through feedforward control schemes.

2.3 Comparisons of small-signal input admittances

In this section, the distortion and contribution factors are introduced to explain the effectiveness of the proposed IIC feedforward controller. The deviation in actual impedance from the expected impedance is referred to as the distortion factor. The distortion factors of the input admittances for the aforementioned control methods are defined by

$$A_{cc}(s) = \frac{G_{cc}(s)}{G_e} = \frac{1/G_e + T(s)}{sL + R + T(s)} \tag{2.28}$$

$$A_{ff}(s) = \frac{G_{ff}(s)}{G_e} = \frac{T(s)}{sL + R + T(s)} \tag{2.29}$$

$$A_{iic}(s) = \frac{G_{iic}(s)}{G_e} = \frac{T(s) + 1/G_e}{sL + R + T(s) + 1/G_e} \tag{2.30}$$

It can be observed that the three distortion factors in (2.28)-(2.30) are identical if the total input impedance ($1/G_e$) of the converters approaches zero. Similarly, if the inductance and parasitic resistance ($sL+R$) of the boost inductor are ignored, as assumed in [43], the other two distortion factors for the feedforward controllers are at unity and there is no distortion. However, the boost inductor impedance term in the denominators of the distortion factors becomes overwhelming and forces the distortion factors into a lagging-phase as the line frequency rises. In low switching frequency applications, the zero-phase crossover occurs at a lower frequency and thus, the boost inductor impedance term is no longer negligible. The boost inductor impedance term should be eliminated by a high bandwidth current-loop compensator. Due to this phenomenon, the conventional voltage feedforward control may not be a suitable approach when the current-loop compensator has limited bandwidth.

Ideally, it is desired to achieve a distortion factor magnitude close to unity at a zero phase difference, yielding ideal power factor correction. Figure 2.8 shows the magnitude and phase response of distortion factors when the input impedance increases where the input frequency is 400 Hz and the bandwidth of current-loop compensator is 1 kHz. It can be observed that the magnitude and phase of $A_{iic}(s)$ approaches the ideal value closer as the

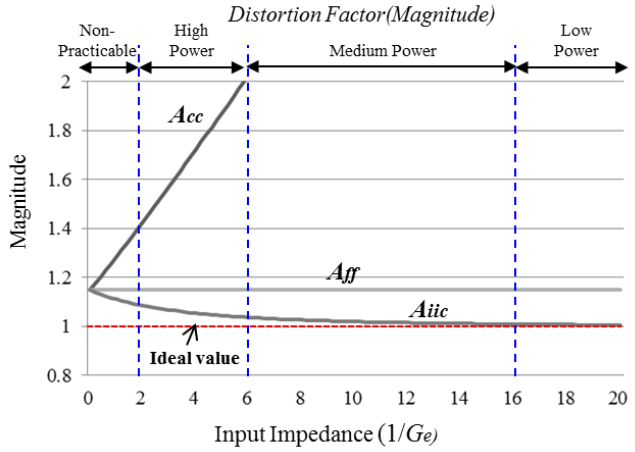

(a) maginitude response

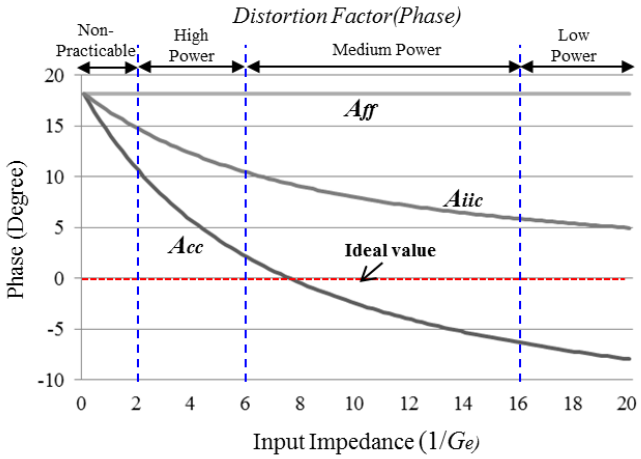

(b) phase response

Figure 2.8 Distortion factors for three control methods vs. input impedance (line frequency: 400Hz, the bandwidth of current loop controller: 1000Hz).

input impedance increases while $A_{ff}(s)$ has some deviations to the ideal value due to unsatisfied current-loop compensator regardless of the input impedance. Figure 2.9 shows the Bode plots of distortion factors in frequency ranges. By employing the proposed method, the input admittance is more constant and the lag is reduced in both G_e=1/31 and G_e=1/10.3.

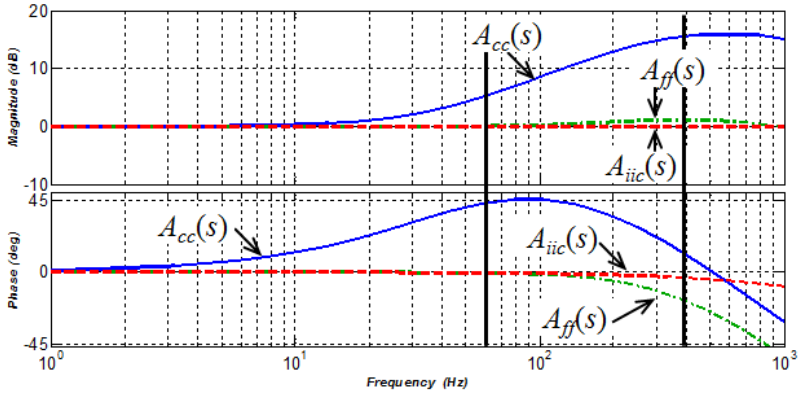

(a) G_e = 1/31

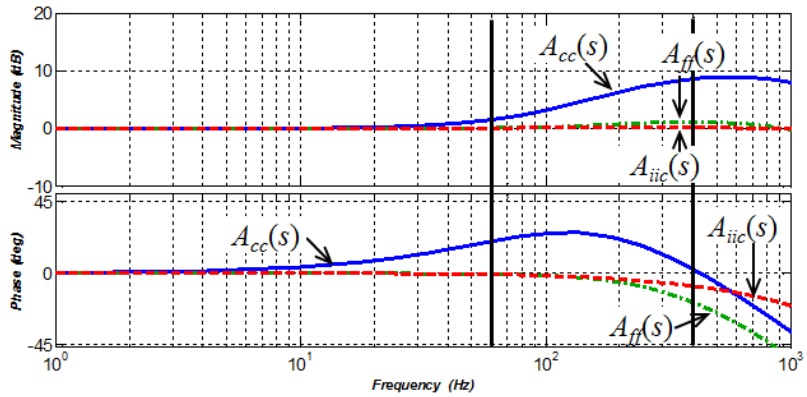

(b) G_e = 1/10.3

Figure 2.9 Bode plots of distortion factor (BW= 1kHz).

As another comparison factor, the contribution factors are introduced to figure out how the proposed IIC feedforward method can effectively reduce undesired input admittance.

$$K_{ff}(s) = \frac{G_{ff}(s)}{G_{cc}(s)} = \frac{G_e T(s)}{1 + G_e T(s)} \tag{2.31}$$

$$K_{iic}(s) = \frac{G_{iic}(s)}{G_{cc}(s)} = \frac{sL + R + T(s)}{sL + R + T(s) + \frac{1}{G_e}} \tag{2.32}$$

Figure 2.10 shows the Bode plots of contribution factors $K_{ff}(s)$ and $K_{iic}(s)$ to the input admittance $G_{cc}(s)$. It should be noted that the phase of $G_{cc}(s)$ is changed from leading phase to lagging phase around 300Hz in Figure 2.10(a) and 450Hz in Figure 2.10(b), respectively. Thus, the lagging input admittance appears in the lower frequency range as the bandwidth of the compensator becomes more limited. It can be noted that these controllers show similar features for eliminating the undesired input admittance of $G_{cc}(s)$ below 100 Hz, but $K_{iic}(s)$ cancels the distorted and displaced input admittance more properly than $K_{ff}(s)$. In other words, the proposed IIC feedforward controller can compensate for an inductive input admittance as the line frequency increases, and a capacitive input admittance as the line frequency decreases. The superiority of the proposed method becomes significantly distinguished from the conventional one as the performance of the current-loop compensator becomes worse.

In addition, it can be seen in (2.31) and (2.32) that the contribution factor of the proposed IIC feedforward method includes inductor impedance in both of numerator and

denominator, from which it can be inferred that $G_{iic}(s)$ is less sensitive to inductance variations. Figure 2.11 shows $G_{ff}(s)$ and $G_{iic}(s)$ under boost inductance (L) variations to compare sensitivity and uncertainties. As expected, the deviation of $G_{ff}(s)$ is significant under inductance variations from 50% to 200%, as shown in Figure 2.11(a) while $G_{iic}(s)$ is less sensitive as shown in Figure 2.11(b).

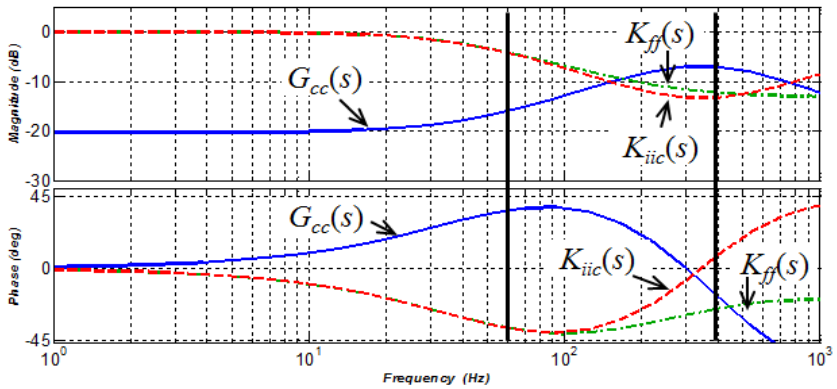

(a) Bandwidth of current loop controller : 500Hz

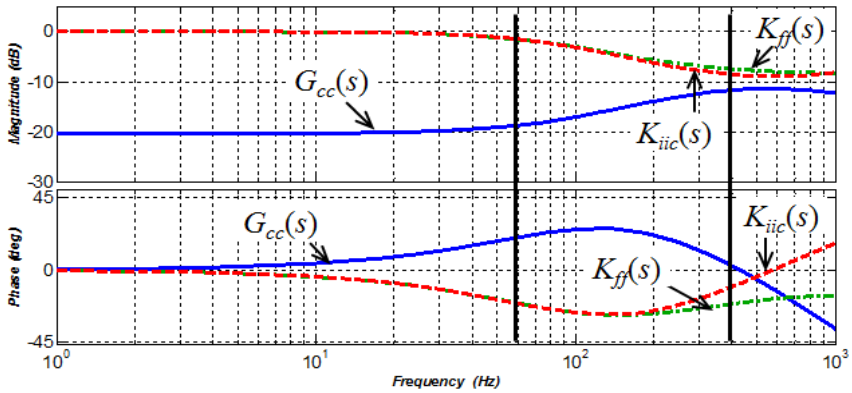

(b) Bandwidth of current loop controller : 1 kHz

Figure 2.10 Bode plots for contribution terms of feedforward controllers.

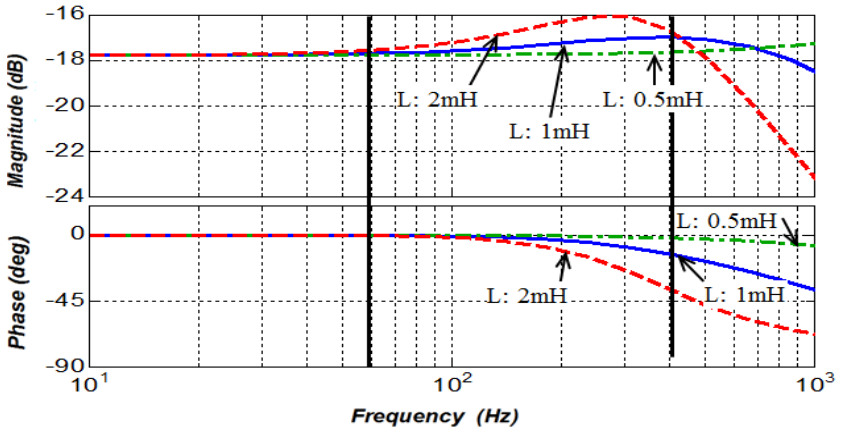

(a) Conventional voltage feedforward

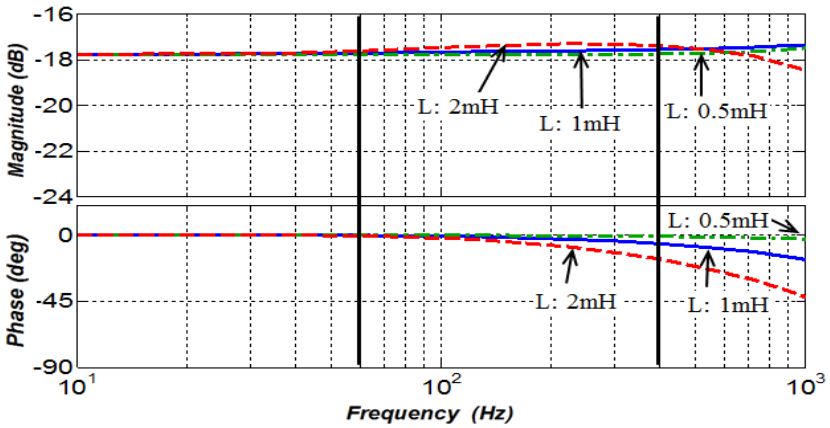

(b) Proposed IIC feedforward

Figure 2.11 Bode plots for input admittance under inductance variations.

2.4 Simulation results

The dual boost PFC converter model is implemented in MATLAB/Simulink environment to investigate the effectiveness and the performance of the proposed IIC feedforward control. For the evaluations of performances, the converter operation under three control strategies with 1 kHz bandwidth of current-loop compensator was simulated: 1) without employing any feedforward controllers, 2) the conventional voltage feedforward control, 3) the proposed IIC feedforward control.

Figure 2.12 the compares steady state input current waveforms obtained in the condition the source voltage is 110Vrms/60Hz. It can be noted that with only current-loop compensator having limited bandwidth, the leading-phase effects and the zero-crossing distortions of the input current are observed at the nominal input frequency (60 Hz), as shown in Figure 2.12(a), but completely these distortion factors disappear shown in Figure 2.12(b) and Figure 2.12(c) when the feedforward methods are applied. Similarly, at the high input frequency (400Hz), the distortion and displacement factors of input current is significantly degraded shown in Figure 2.13(a) and 2.13(b) due to lagging-phase effects, meanwhile significant reduction in terms of the displacement value has been achieved in the proposed IIC feedforward controller compared to the conventional voltage feedforward controller, as shown in Figure 2.13(c). The simulation results indicate the proposed method’s superiority in the time domain, as Figure 2.9 displays this in the frequency domain.

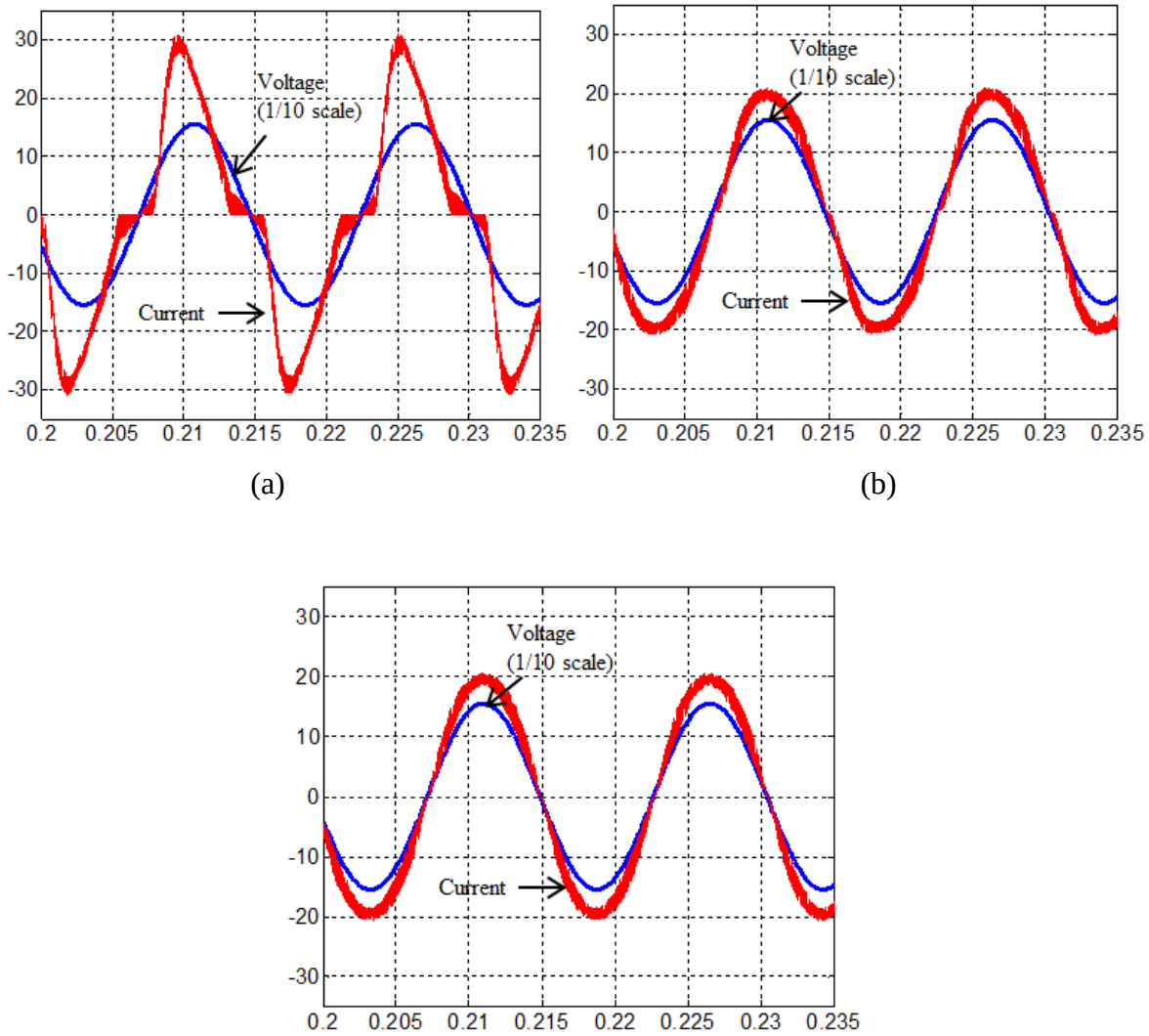

(a) (b)

(c)

Figure 2.12 Simulation results; line frequency : 60Hz.
(a) without any feedforward control (PF: 0.93, THD:33.4%),
(b) the conventinal voltage feedforward (PF: 0.99, THD: 4.5%)
(c) the proposed IIC feedforward (PF: 1.0, THD:2.1%).

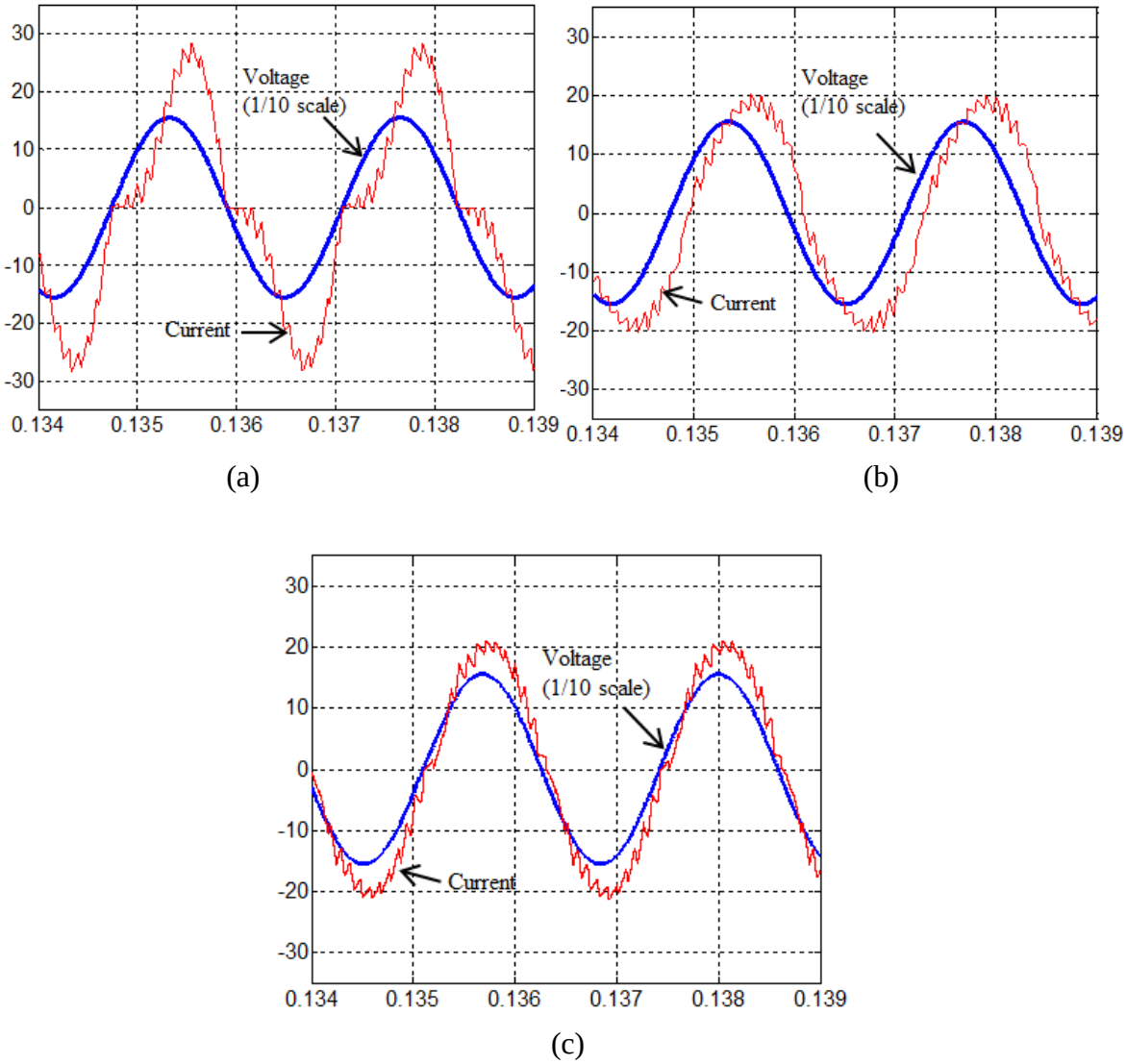

Figure 2.13 Simulation results; line frequency : 400Hz.
(a) Without any feedforward control (PF: 0.89, THD:28.7%)
(b) Conventinal voltage feedforward (PF: 0.86, THD: 10.1%)
(c) Proposed IIC feedforward (PF: 0.98, THD:7.3%).

2.5 Experimental results

Figure 2.14 shows the prototype ac-dc and dc-dc converter for a battery charger. For an ac-dc converter, a single-phase dual boost converter based on low-cost digital control was used to verify the proposed IIC feedforward control. Table 2.1 lists some important experimental values.

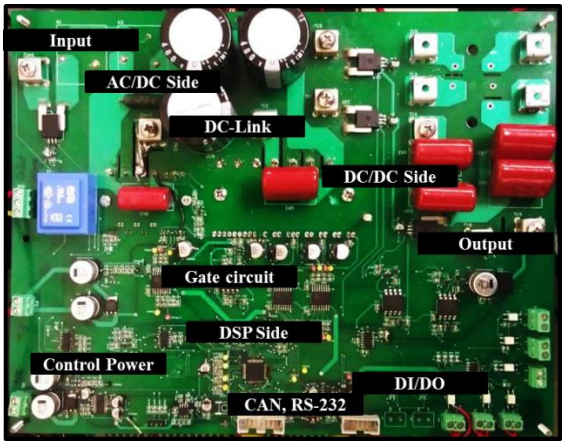

Figure 2.14. Proto-type dual boost PFC converter with a dc-dc converter.

TABLE 2.1 Experimental setup

System parameter	***Values***
AC Source Voltage	110 Vrms / 60Hz and 400Hz
Rated Power	1.2 kW
Switching Frequency	15 kHz
Sampling time	75 us
Boost Inductor	0.9mH (split into two in series)
DSP	TMS320F28035(60MHz)
Power device	FPDB60PH60B (FAIRCHILD)
Load	Resistive dc loads
Grid emulator	Programmable AC source

Figure 2.15 and Figure 2.16 show experimental results comparing the performances of the conventional feedforward controller and the proposed IIC feedforward controller, both with a 1 kHz bandwidth current compensator. Figure 2.15 show the input current and voltage at the nominal input frequency (60Hz). When feedforward controllers are employed, exceptionally high performance with low distortion factor and low displacement factor can be seen. However, input current shown in Figure 2.16(a), using the conventional feedforward controller is displaced significantly at the high input frequency (400Hz) because of the effect of uncompensated lagging-phase admittance. Meanwhile, input current shown in Figure 2.16(b), using the proposed IIC feedforward control is less displaced and still has acceptable PFC performance with a low bandwidth compensator indicating a reduced ratio of switching frequency to input frequency.

The results for THD and power factor between the two feedforward methods are compared in Table 2.2. The proposed IIC feedforward control has superior performance where it result in 17% improvement in the displacement factor and 0.3% improvement in the distortion factor when the ac-dc boost converter has a limited-bandwidth current compensator at 400Hz line frequency. This can be explained with the analytical results in Figure 2.9—the input admittances of two feedforward control methods behave similarly with input admittance at 60Hz, whereas the proposed method has a distinguishably reduced lagging-phase at 400Hz in the phase domain. Compared to the conventional method, the proposed method fares better in terms of displacement factor rather than in THD. In conclusion, the experimental results demonstrate that the proposed IIC feedforward

controller is an enhanced solution for power factor correction at low switching/sampling frequency operation.

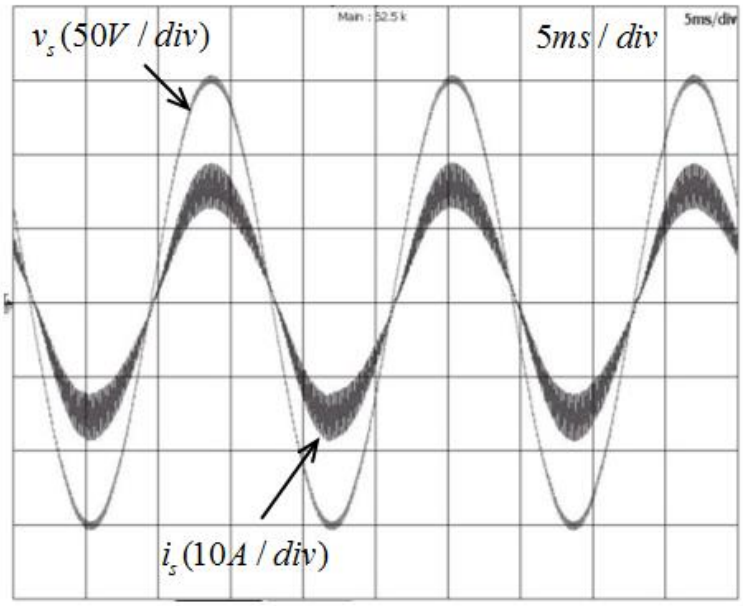

(a) Conventional feedforward control

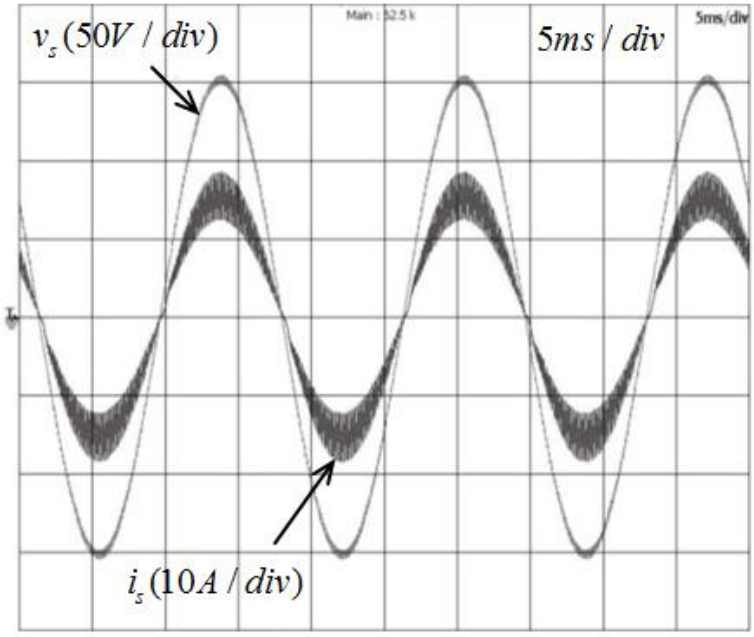

(b) Proposed feedforward control

Figure 2.15 Experimental results (line frequency: 60Hz).

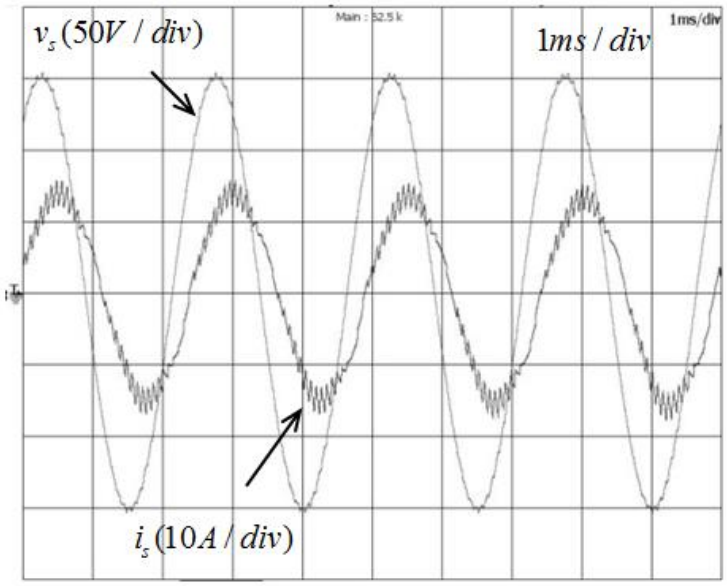

(a) Conventional feedforward control

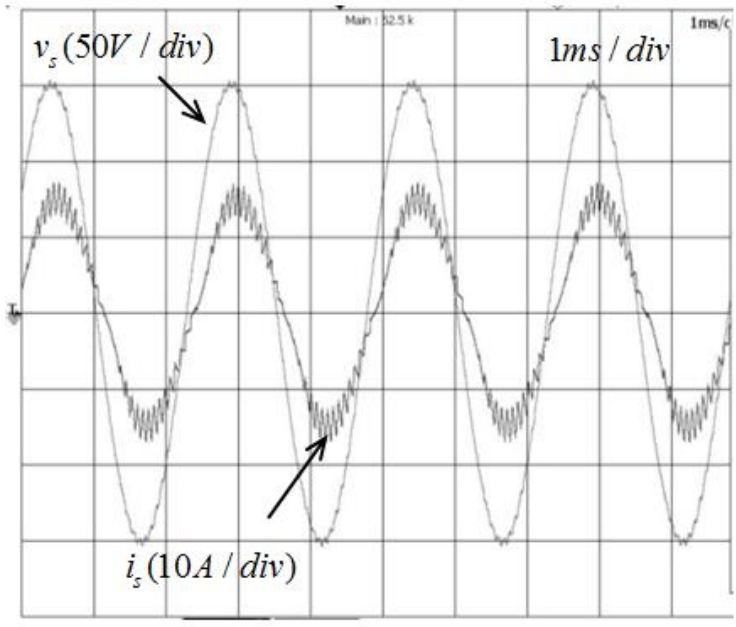

(b) Proposed feedforward control

Figure 2.16 Experimental results (line frequency: 400Hz).

TABLE 2.2 Summary of Experimental Results

Method	***60Hz line frequency***		***400Hz line frequency***	
	THD	***P.F***	***THD***	***P.F***
Conventional	4.0%	1.0	5.3%	0.80
Proposed IIC	3.0%	1.0	5.0%	0.97

2.6 Summary

This chapter has presented the input impedance and current (IIC) feedforward control method to solve the phase shift problems of the input current caused by lagging-phase admittances in low switching/sampling and high line frequency applications. The proposed method can reduce the undesired effects of input admittances over wide frequency ranges as a leading-lagging phase admittance cancellation. The effectiveness of the proposed method was analyzed through small input admittances, the distortion and contribution factors. Simulation and experimental results show that input power quality is improved through the proposed IIC feedforward control, which supporting the theoretical analysis. In addition, the proposed IIC feedforward method can be utilized easily with simple modification of the existing voltage feedforward equation. Consequently, these features make the proposed IIC feedforward method extremely fit for digital implementation in ac-dc boost converters with limited bandwidth.

Chapter 3. Active power filter functionalities using unidirectional converters

3.1 Introduction

Power quality analysis in ac power systems is concerned with deviations of the voltage or current from the desired, ideal sinusoid of constant amplitude and frequency [25]. Most residential loads are not purely resistive, often producing harmonics due to their nonlinearity; while linear loads consume or generate reactive power, which reduces the active power available. Unfiltered harmonics cause interferences in other electric facilities, creating abnormal and undesirable behavior of electrical equipment and transformer overheating [8]. Uncontrolled reactive power increases transmission conduction losses and deteriorates the performance of voltage regulation [55]. Therefore, it is desired to reduce these effects through adequate means in power systems, i.e., harmonic current compensation (HCC) and reactive power compensation (RPC) [8], [9], [55], [56].

The focus of this chapter is to investigate a cost-effective power quality mitigation solution for residential power systems by utilizing existing commercial unidirectional converters [18], [19], [57] typically used for home appliances and battery chargers with unidirectional power flow, even though HCC and RPC in these applications conflicts with the basic purpose and premise of maximizing the power factor of these products. Since an immense number of these unidirectional converters are present within residential power systems, these unidirectional converters, operating in unison, have a high potential as alternative HCC and RPC units, and thus these converters can act in place of larger, more costly HCC and RPC equipment if they possess these functionalities.

In recent years, few papers have detailed HCC and RPC functionalities using unidirectional PFC converters in [17], [23], [24]. In [17], authors broadly reviewed battery charger topologies used for EV/PHEV applications for providing reactive power support to the grid, but the RPC capability in unidirectional converters was mentioned briefly and any further analysis was not conducted. In [23], the feasibility of HCC functionality using a boost converter was presented as a low cost solution, but RPC functionality was not considered. In [24], the reactive power support capabilities of the unidirectional converter within V2G applications were studied through simulation results, but detailed analysis regarding input current distortions was not performed.

In this chapter, the feasibility and limitations of the unidirectional ac-dc boost PFC converter are explored for HCC and RPC. In addition, an approach for estimating the distortion levels of the current under reactive power compensation modes is analytically justified. This chapter starts with descriptions of control modes and analysis of local loads for the proposed system in Section 3.2. The distortion levels on the input currents when the unidirectional ac-dc boost converter is employed for RPC are analytically explained in Section 3.3. MATLAB/Simulink simulation results are shown in Section 3.4. Experimental results using a 1.2-kW dual boost PFC converter are presented in order to validate the proposed approach in Section 3.5. Finally, Section 3.6 concludes the chapter.

3.2 Control algorithms

The dual boost PFC converter [22], [28], [46], [52], [53], often called the bridgeless PFC converter, is one of the most popular unidirectional ac-dc boost converters. There are a few commercial power modules including IGBTs, gate circuits and protection circuits,

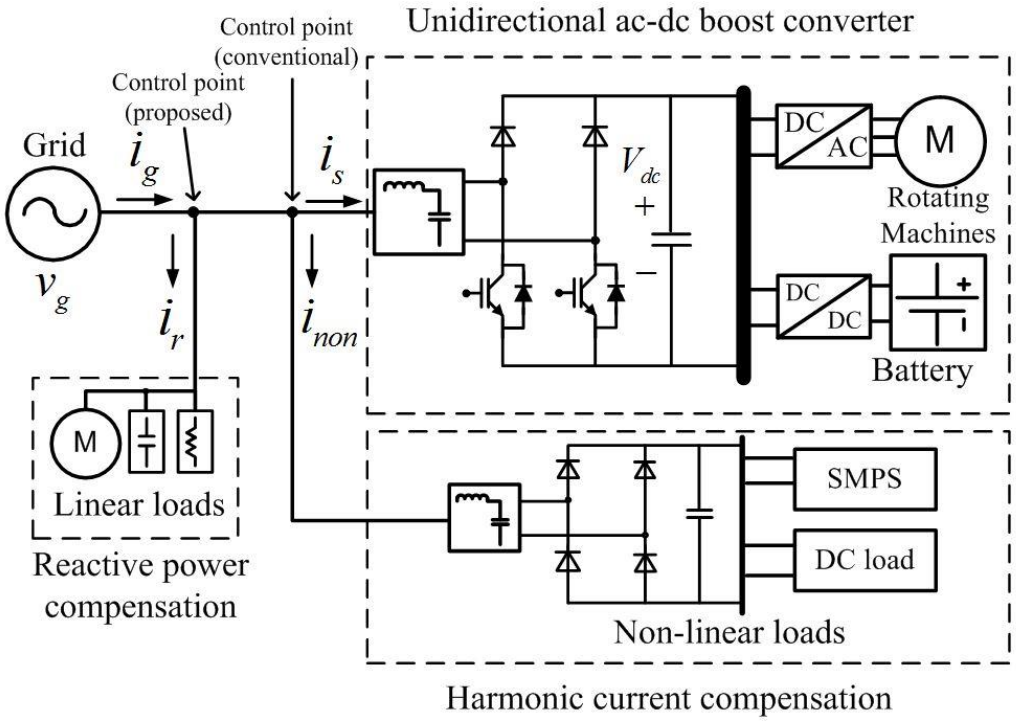

Figure 3.1 Proposed unidirectional ac-dc boost converter systems.

which accelerates the application of this topology to home appliances and digital products [20]-[22], [28]. The control algorithms of the dual boost PFC converter are almost identical to any conventional ac-dc converter using a diode rectifier and step-up chopper, except that the dual boost PFC converter controls ac input current while the conventional one controls rectified output current. Figure 3.1 shows a prevalent application of unidirectional ac-dc boost converters. The investigated loads are a non-linear load with harmonic current and a linear load with a poor power factor, which results in reduced power quality. Conventional

PFC converters consider the input current to be a purely sinusoidal waveform which is completely in phase with the input voltage. The proposed control method can ameliorate harmonic current and reactive power for improved grid power quality as well as regulation of dc-bus voltage. Even though the capacity of HCC and RPC is limited compared to APFs, this control strategy will contribute to a more stable power system without additional costs. The proposed versatile control of unidirectional ac-dc boost converter has three modes of operation, *i.e.*, PFC, HCC and RPC. Also, both HCC and RPC can operate simultaneously to improve the distortion and the displacement factors of the grid current.

3.2.1 Harmonic current compensation

The distorted current due to nonlinear loads can be decomposed into a weighted sum of sinusoids whose frequencies are integer multiples of the fundamental frequency via the Fourier series [25]. Figure 3.2 shows the current waveform of a typical nonlinear load in a single-phase diode rectifier. Generally, the distorted load current, i_{non}, can be written in terms of its fundamental components, i_{fn}, and harmonic components, i_{hn}, as

$$i_{non} = i_{fn} + i_{hn} = I_1 \sin(\omega_1 t + \theta_1) + \sum_{n=2,3,\ldots}^{\infty} I_n \sin(n\omega_1 t + \theta_n) \tag{3.1}$$

where ω_1 is the line angular frequency and θ_n is the phase difference between the source voltage and input current. Assume that the input current from the unidirectional ac-dc boost converter operating in PFC mode is a purely sinusoidal waveform. The grid current i_g includes i_{hn} from a nonlinear load as shown in Figure 3.3(a). These harmonics are undesirable and should be removed. If the unidirectional ac-dc boost converter can generate the harmonic current capable of canceling the harmonics of the nonlinear load, the grid

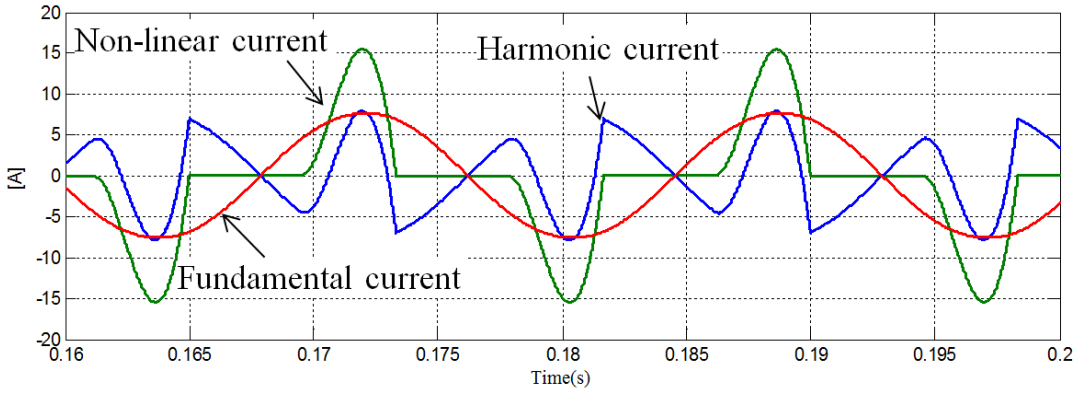

Figure 3.2 Example for non-linear load current.
(THD: 80%, PF: 0.705, P: 550W, Q: 200 Var)

current will be comprised of only fundamental components of the converter current and load current as shown in Figure 3.3(b). Therefore, the new current reference for the current controller of the converter from Figure 3.4 can be expressed as

$$i_s^* = I_s^* \sin(\omega t) - i_{hn} \tag{3.2}$$

where I_s^* is the magnitude reference provided by the dc-bus voltage controller. The harmonic current at the load side can be obtained by subtracting the measured load current from the fundamental load current which can be estimated by employing a band pass filter in real implementations.

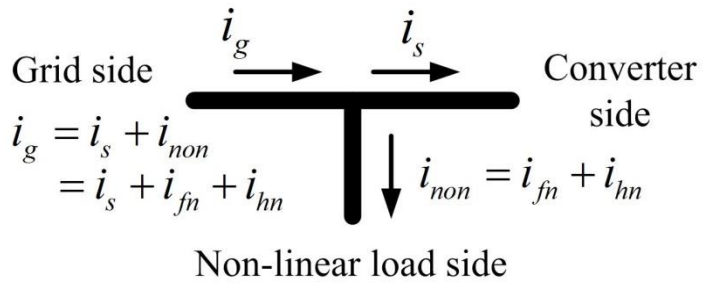

(a) Without HCC

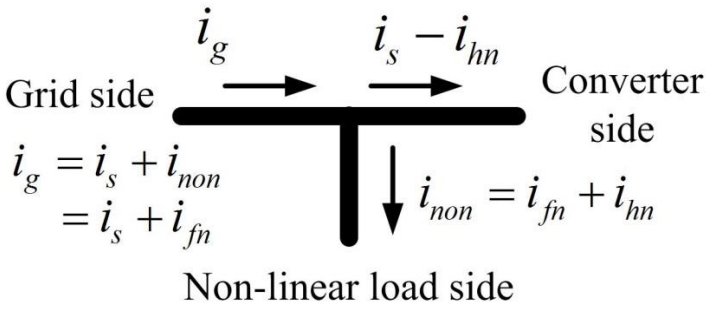

(b) With HCC

Figure 3.3 Harmonic current flow diagrams.

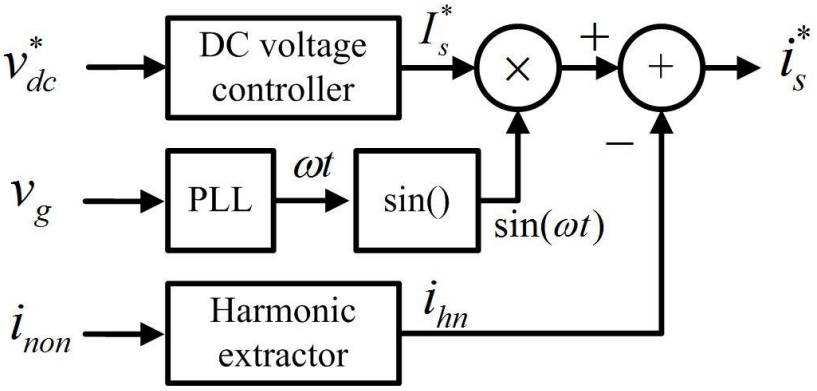

Figure 3.4 Current reference generator block for HCC.

3.2.2 Reactive power compensation

Unlike non-linear loads, the current waveform of a linear load is sinusoidal at the frequency of the power system [25], but the power factor can be significantly exacerbated when the load is capacitive or inductive. This reactive power increases the total current unnecessarily in power systems, which causes increased conduction losses or reduced performance of voltage regulation at PCC. Therefore, the compensation of reactive power is required. Figure 3.5 shows the current waveform of a typical inductive load in a single-phase induction motor. The current flow, consisting of the converter current with RPC and the load current i_r consuming reactive power, shown in Figure 3.6, can be written respectively as

$$i_s = i_{s\alpha} - j i_{s\beta} \tag{3.3}$$

$$i_r = i_{r\alpha} + j i_{r\beta} \tag{3.4}$$

$$i_g = i_{r\alpha} + i_{s\alpha} + j(i_{r\beta} - i_{s\beta}) \tag{3.5}$$

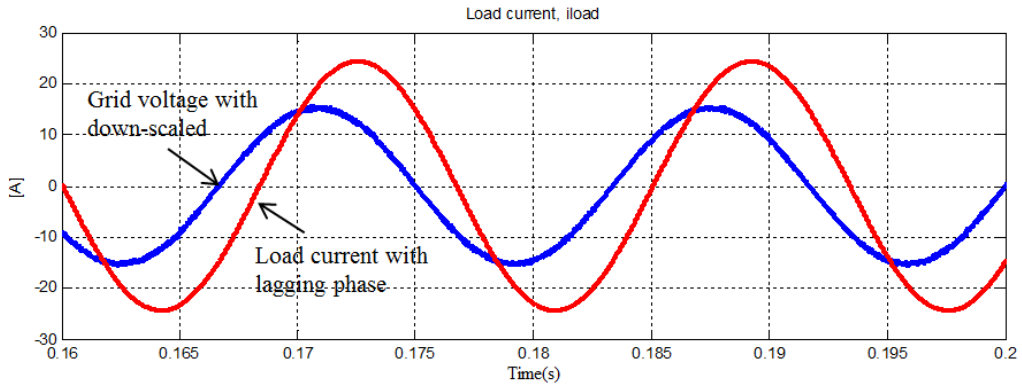

Figure 3.5 Example for linear load current (THD: 0.5%, PF:0.8, active power: 1500W, reactive power: 1100 Var).

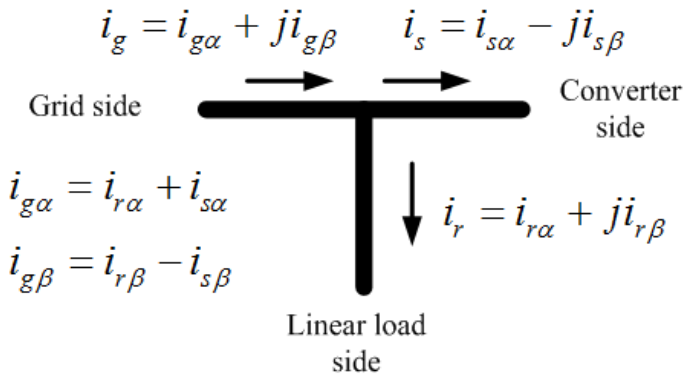

Figure 3.6 Current flow diagram in RPC mode at the PCC.

As a result, the grid power factor at the PCC can be improved by injecting reactive power from the converter as shown in Figure 3.7. However, it should be considered that the input current of the unidirectional converter becomes distorted due to the natural commutation of diodes, thus the amount of reactive power generated by an individual converter should be restricted [J1],[C3],[24]. Since the current waveform of the converter in RPC mode is not sinusoidal, the required phase angle of the current cannot be calculated by a simple reactive power equation. Thus, the phase angle reference to the input converter current needs to be generated by employing a proportional integral (PI) compensator as shown in Figure 3.8 and can be represented as

$$\phi = K_{pc}(Q^* - Q) + K_{ic}\int (Q^* - Q)dt \tag{3.6}$$

$$i_s^* = I_s^* \sin(\omega t + \phi) \tag{3.7}$$

where K_{pc} and K_{ic} are proportional gain and integral gain of the reactive power compensator, respectively and ϕ is the desired phase to be adjusted from the original current reference. As an alternative method, the look-up table for generating a proper phase angle can be applied in an open loop manner. It should be noted in (3.7) that the current magnitude reference I_s^* will be adjusted through the dc-bus voltage controller to feed active power to the dc load. The reactive power will be adjusted by changing the phase angle, ϕ. Thus, initially I_s^* is determined by the dc link voltage controller and actual active power will change as result of generating reactive power with respect to the dc link command. However, since I_s^* will be updated by the dc link voltage compensator, as the phase angle ϕ changes, the dc link voltage will be maintained.

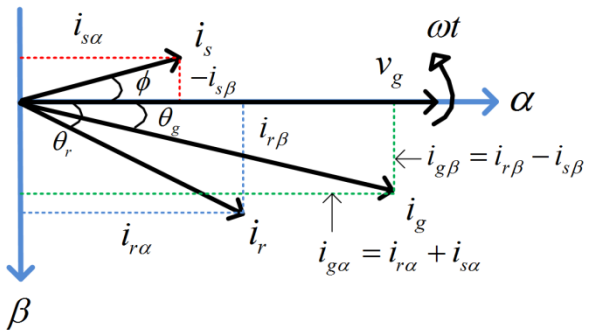

Figure 3.7 Phase diagram of the grid voltage and current during RPC.

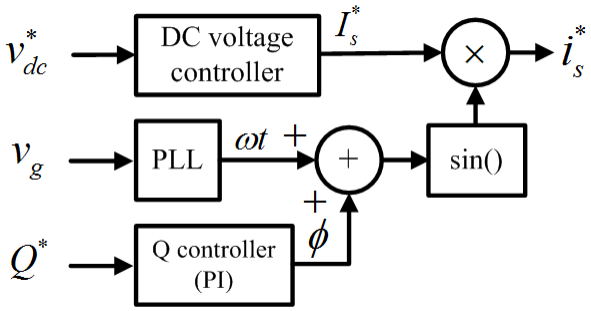

Figure 3.8 Current reference generator block for RPC.

3.2.3 Control strategy for APF functionality

The proposed control strategy of the unidirectional ac-dc converter including a feedforward controller, HCC, and RPC is shown in Figure 3.9. Two control blocks for HCC and RPC have been added to the conventional control algorithm. Thus, the final current reference for a versatile control strategy based on (3.2) and (3.7) can be expressed as

$$i_s^* = I_s^* \sin(\omega t + \phi) - i_{hn} \tag{3.8}$$

In addtion, it is worthwhile to mention that functionalities of HCC and RPC in unidirectional ac-dc boost converters are available only when these converters supply active power to its dc load. Thus, the current reference able to be used for HCC and RPC is highly dependent on its power rating and its existing loads, signifying that the amount of RPC should be limited due to current distortions caused as a result of the feature. Since multiple unidirectional converters may be connected to the power system in residential applications, their RPC capabilities can be maxmized by incorporating these aggregated converters as shown in Figure 3.10.

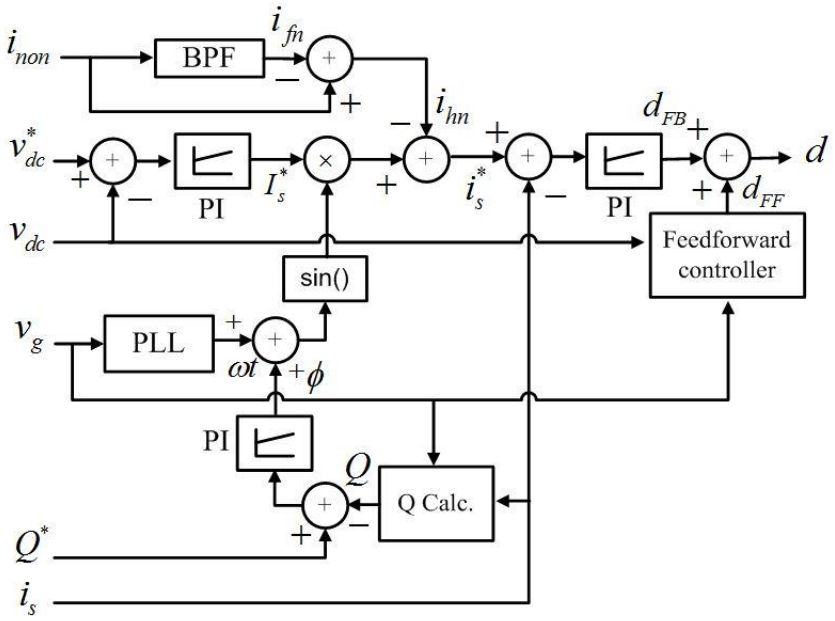

Figure 3.9 Proposed HCC and RPC control block diagram.

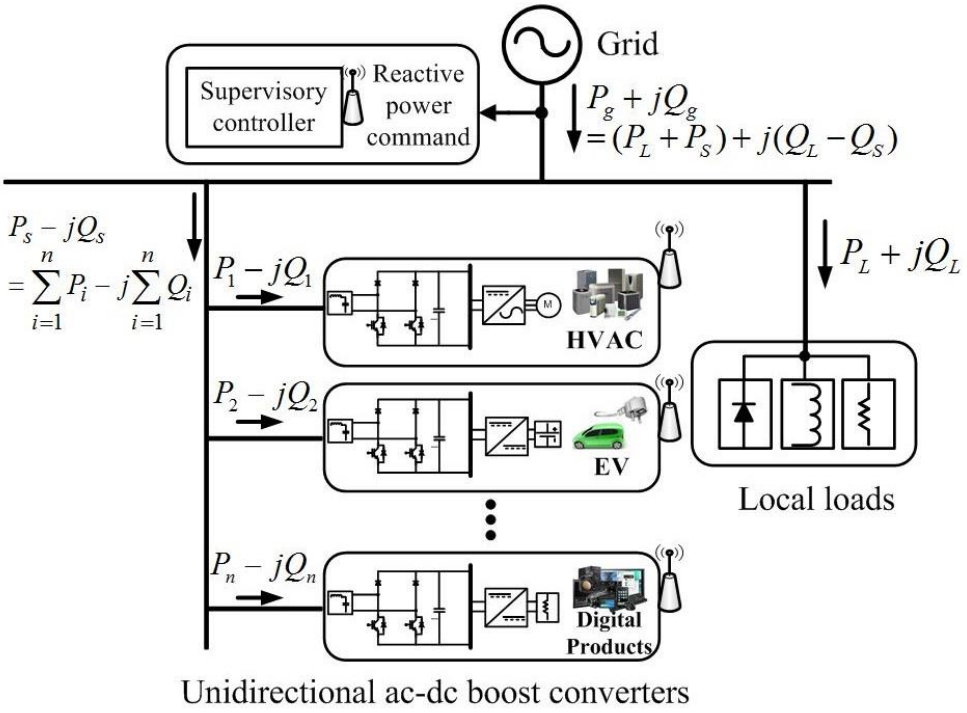

Figure 3.10 Reactive power compensation using aggregated unidirectional converters.

The possible supervisory control strategy for future smart grid applications [58] in aggregated unidirectional converters with proposed control method can be suggested as follows

(1) Analyze grid power quality factors, such as THD and PF.

(2) Calculate the amount of compensation for harmonic-producing components and reactive power.

(3) Obtain the available capacities used for HCC and RPC in an individual converter.

(4) Determine and distribute HCC and RPC references to an individual converter.

(5) Analyze the grid power quality. If the THD of the grid current is above 5%, the level of RPC needs to be reduced. Otherwise, the amount of RPC can be increased up to each converter's maximum capacity to achieve unity power factor.

(6) Repeat (1) through (5).

Using these steps, the grid power quality can be enhanced, as long as the available converter capacities for HCC and RPC remain.

3.3 Current harmonic analysis

In the conventional control method of unidirectional ac-dc boost converters, the magnitude and phase of the current reference can be obtained in the dc-voltage controller and the phase-locked-loop (PLL), respectively. By adjusting the phase angle, ϕ in (3.6), the current either leads or lags in reference to the voltage. This allows the generation or consumption of reactive power in unidirectional ac-dc boost converters. Due to the intrinsic operation of diodes, however, uncontrolled regions exist where the signs of the input voltage and current reference are opposite [59] and the actual current in unidirectional converters is not capable of following the current reference exactly. Therefore, an analytical approach is required to estimate current distortions and actual generated power. To simplify and generalize the current waveform in this paper, it is assumed that the duty output from the controller is zero in these regions.

3.3.1 Extended cusp distortion in the capacitive current

Figure 3.11(a) depicts the comparison of the current waveforms during capacitive power compensation. It can be observed in Figure 3.11(b) that there are two distortion periods, called the zero-current distortion and the cusp distortion regions. Due to the unidirectional power flow capabilities of the converter, the current is periodically uncontrollable when signs of the input voltage and current reference are opposite, which creates the zero-current distortion region, ϕ. In addition, the current drastically increases after the grid voltage crosses zero, which leads to the cusp distortion common to all boost converter topologies [60]. This occurs because the inductor voltage is limited in its ability to drive its current up, even with the switch closed during this time [59].

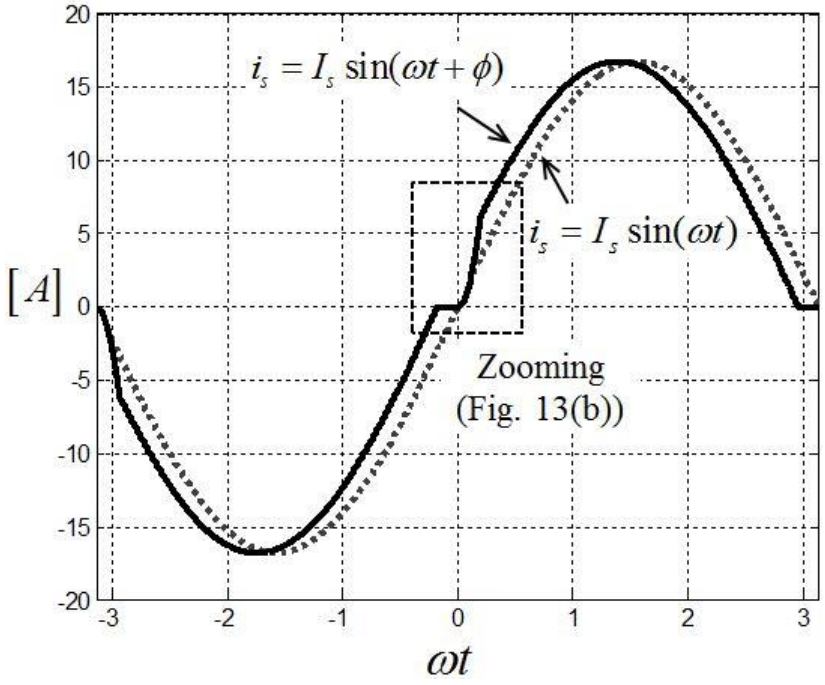

(a) comparison of current wavefoms

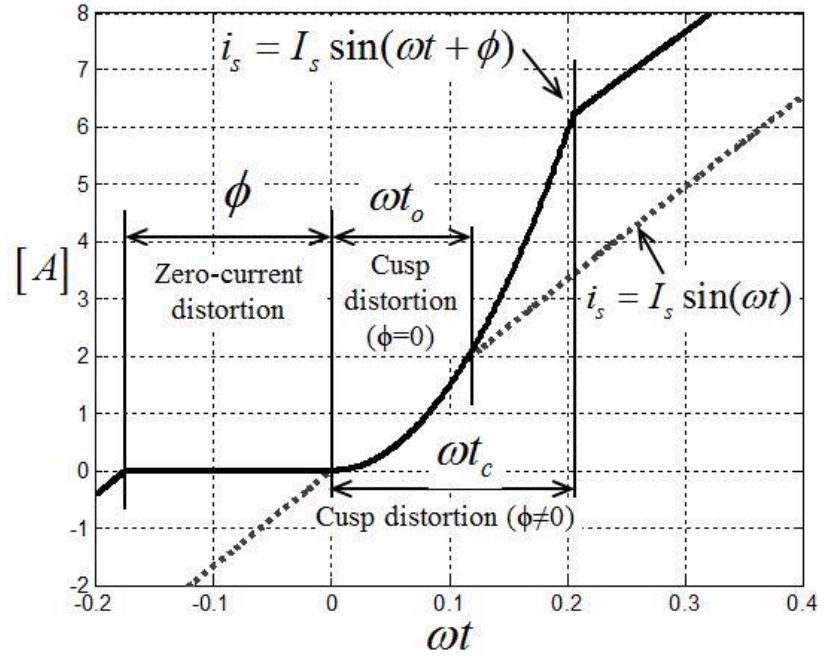

(b) the zero-current and cusp distortion in zoomed regions

Figure 3.11 Current waveform in capacitive power compensation.

It should be noted in Figure 3.11(b) that the duration of the cusp distortion is extended up to t_c in capacitive power compensation, compared to the original t_o in unity power factor mode. Since the switch is always on during the cusp distortion (d=1 in this condition), only the source voltage and inductor voltage remain in Figure 2.3, i.e. the averaged source voltage is zero. Therefore, the input current is described by

$$i_s(t) = \frac{V_g}{L}\int_0^{t_c} \sin(\omega t)dt = \frac{V_g}{X}\left(1-\cos(\omega t_c)\right) \qquad \text{where, } X = \omega L \tag{3.9}$$

where, V_g is the peak input voltage. The cusp distortion continues until the actual current meets the capacitive current reference

$$\frac{V_g}{X}\left(1-\cos(\omega t_c)\right) = I_s \sin(\omega t_c + \phi) \tag{3.10}$$

By solving (3.10) in terms of ωt_c, the extended duration of the cusp distortion, ωt_c can be calculated as

$$\omega t_c = \tan^{-1}\left(\frac{\sqrt{X^2 I_s^2 + 2V_s I_s X \sin\phi}}{V_g}\right) + \tan^{-1}\left(\frac{I_s \cos\phi}{I_s \sin\phi + \frac{V_g}{X}}\right) \tag{3.11}$$

ωt_o can be obtained as $2\tan^{-1}(XI_s/V_g)$ when ϕ is zero in (3.11), which corresponds with [60]. Figure 3.12(a) shows ωt_c values calculated by (3.11) with various inductances L under v_g is 110 V_{rms}. It increases in magnitude as the inductance value and peak current increase. Additionally, ωt_c is prolonged, as shown in Figure 3.12(b), when more capacitive current is

required because the current error between the actual current and reference current after the zero crossing of the input voltage grows.

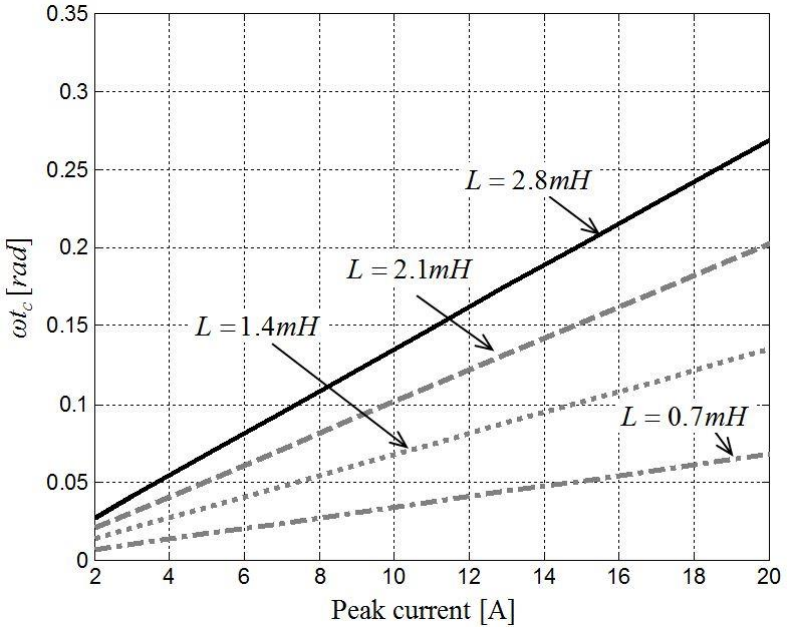

(a) ωt_c versus peak current for different L values when ϕ=0

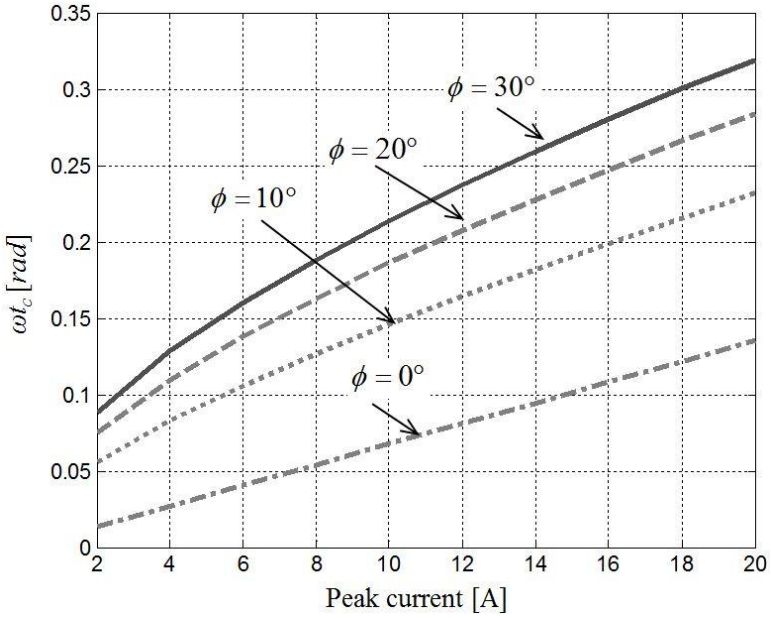

(b) ωt_c versus peak current for different ϕ when L=1.4 mH

Figure 3.12 Duration of the cusp distortion in various L values and capacitive currents.

3.3.2 Analysis of the current waveform in capacitive power compensation

Based on periods of zero-current and cusp distortions, the resulting current waveform in capacitive power compensation can be defined by

$$i_s(t) = \begin{cases} \frac{V_s}{X}\left(1-\cos(\omega t)\right) & ,0 \le \omega t < \omega t_c \\ I_s \sin(\omega t + \phi) & ,\omega t_c \le \omega t < \pi - \phi \\ 0 & ,\pi - \phi \le \omega t < \pi \\ \frac{V_s}{X}\left(-1-\cos(\omega t)\right) & ,\pi \le \omega t < \pi + \omega t_c \\ I_s \sin(\omega t + \phi) & ,\pi + \omega t_c \le \omega t < 2\pi - \phi \\ 0 & ,2\pi - \phi \le \omega t < 2\pi \end{cases} \tag{3.12}$$

Even though the current reference in (3.7) is used to generate or consume reactive power, the real current is not capable of tracking the current reference in an exact manner due to the zero current and extended cusp distortions. Since the real currents are distorted, the fundamental current needs to be extracted to calculate the actual active and reactive power. According to the Fourier series, the current waveform in (3.12) can be expressed as the sum of multiple sinusoids of different frequencies [25]

$$i_s(t) = a_0 + \sum_{n=1}^{\infty}\left[a_n \cos n\omega t + b_n \sin n\omega t\right] \tag{3.13}$$

where a_o is the dc value (zero under a perfect ac waveform, i.e. $a_o = 0$), a_n and b_n are the amplitudes of the n-th cosine-term and sine-term harmonics, respectively. Regarding the fundamental content of the capacitive current in (3.12), the Fourier series coefficient at the fundamental frequency can be solved as

$$a_1 = \frac{1}{2\pi}\begin{pmatrix} I_s\left(\cos\left(\phi+2\omega t_c\right)-\cos\phi+2\left(\pi-\phi-\omega t_c\right)\sin\phi\right) \\ -\frac{V_s}{X}\left(\sin\left(2\omega t_c\right)-4\sin\left(\omega t_c\right)+2\omega t_c\right) \end{pmatrix} \tag{3.14}$$

$$b_1 = \frac{1}{2\pi}\begin{pmatrix} I_s\left(\sin\left(\phi+2\omega t_c\right)+\sin\phi+2\left(\pi-\phi-\omega t_c\right)\cos\phi\right) \\ +\frac{2V_s}{X}\left(\cos\left(\omega t_c\right)-1\right)^2 \end{pmatrix} \tag{3.15}$$

Using (3.14) and (3.15), the current with the fundamental radian frequency, ω can be obtained as

$$i_{s1} = I_{s1}\sin(\omega t+\delta) \tag{3.16}$$

where, $I_{s1} = \sqrt{a_1^2+b_1^2}$, $\delta = \tan^{-1}\left(a_1/b_1\right)$

It should be noted that δ is a displacement angle in the current in reference to the fundamental frequency, which contributes to the production of actual active and reactive power, rather than just at the phase angle reference (ϕ). The *rms* value of the current waveform in (3.12) can be defined and calculated as

$$\begin{aligned} I_{srms} &= \sqrt{\frac{1}{2\pi}\int_0^{2\pi} i_s^2(t)dt} \\ &= \sqrt{\frac{1}{4\pi}\left(I_s^2\left(2\left(\pi-\phi-\omega t_c\right)+\sin\left(2\phi+2\omega t_c\right)\right)+\frac{V_s^2}{X^2}\left(6\omega t_c+\sin\left(2\omega t_c\right)-8\sin\left(\omega t_c\right)\right)\right)} \end{aligned} \tag{3.17}$$

Using *rms* values of the fundamental and total current from (3.16) and (3.17), the theoretical THD values of the input current under RPC can be obtained as

$$THD_{th} = \frac{\sqrt{I_{srms}^2 - I_{s1rms}^2}}{I_{s1rms}} \qquad where,\ I_{s1rms} = \frac{\sqrt{a_1^2 + b_1^2}}{\sqrt{2}} \tag{3.18}$$

In addition, the active and reactive power under RPC can be calculated as

$$P = \frac{1}{2} V_s I_{s1} \cos\delta \tag{3.19}$$

$$Q = -\frac{1}{2} V_s I_{s1} \sin\delta \tag{3.20}$$

Finally, using (3.18)-(3.20), the theoretical THD values and the expected active and reactive power in capacitive power compensation mode can be calculated as shown in Figure 3.13. It can be noted that not only the zero-current distortion, but also the cusp distortion causes the current distortion level to increase at higher capacitive power.

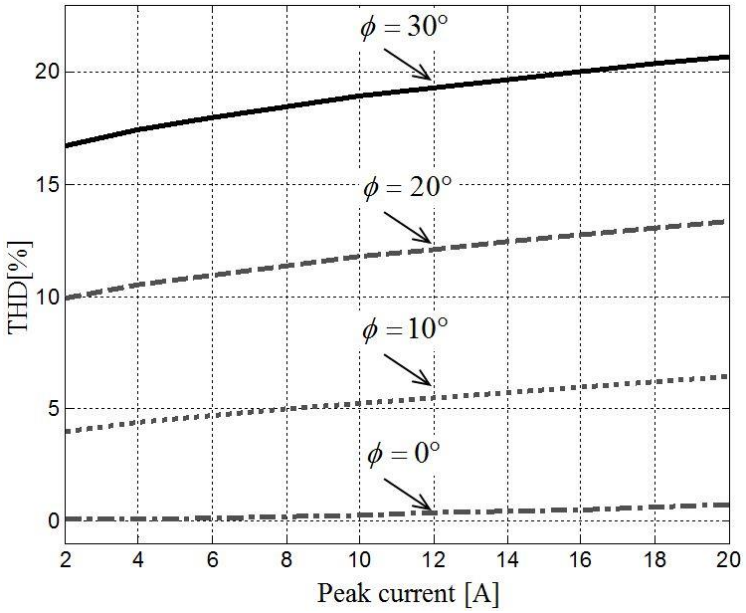

(a) THD versus peak current for different ϕ

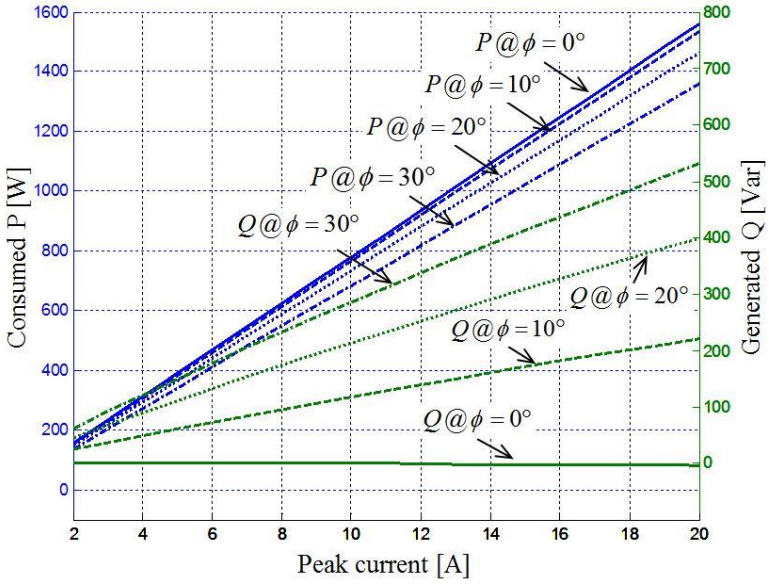

(b) active power and reactive power versus peak current for different ϕ

Figure 3.13 Analytical results in capacitive power compensation mode.

3.3.3 Analysis of the current waveform in inductive power compensation

Similarly, Figure 3.14 depicts the comparison of the current waveforms with varying inductive power. Compared to the capacitive current, the cusp distortion is not as pronounced because the voltage across the boost inductor is already high enough to drive the required current. However, in this scenario, the zero-current distortion still appears due to the uncontrollable regions caused by the diodes. The resulting current waveform for inductive power compensation is simpler than the capacitive current and can be defined as

$$i_s(t) = \begin{cases} 0 & ,0 \le \omega t < \phi \\ I_s \sin(\omega t - \phi) & ,\phi \le \omega t < \pi \\ 0 & ,\pi \le \omega t < \pi + \phi \\ I_s \sin(\omega t - \phi) & ,\pi + \phi \le \omega t < 2\pi \end{cases} \tag{3.21}$$

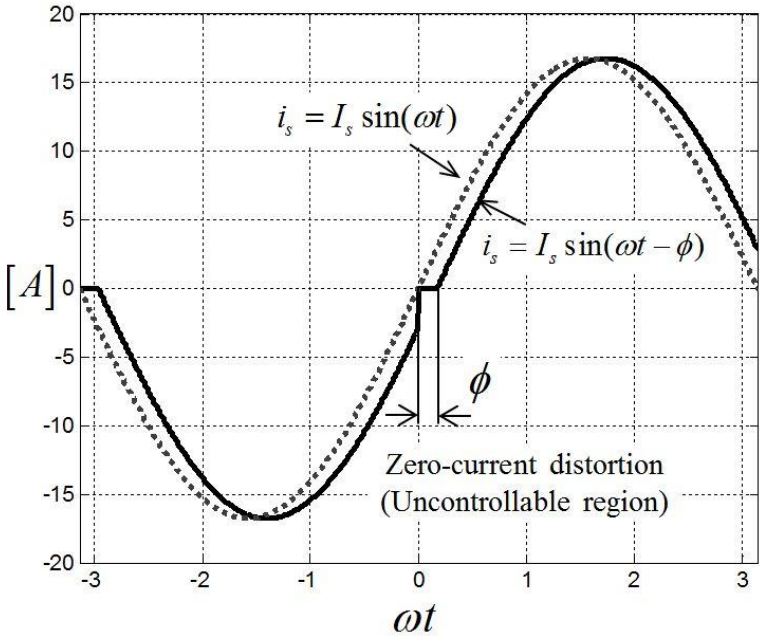

Figure 3.14 Current waveform in inductive power compensation.

Deriving the Fourier series coefficients in the same way, and expressing the rms values of the current with respect to the fundamental frequency

$$a_1 = \frac{-I_s\left(\pi-\phi\right)\sin\phi}{\pi} \tag{3.22}$$

$$b_1 = \frac{I_s}{\pi}\left(\sin\phi+\left(\pi-\phi\right)\cos\phi\right) \tag{3.23}$$

$$I_{srms} = \sqrt{\frac{1}{2\pi}\int_0^{2\pi} i_s^2(t)dt} = \sqrt{\frac{I_s^2}{4\pi}\left(2\left(\pi-\phi\right)+\sin\left(2\phi\right)\right)} \tag{3.24}$$

(3.22) and (3.23) are used to obtain the fundamental current in (3.16); substituting its outcome and (3.24) into (3.18)-(3.20) yields the expected values of the THD, active power, and reactive power in inductive power compensation, as shown in Figure 3.15. It is notable that the distortion level remains unchanged regardless of the magnitudes of the current, but deteriorates as ϕ increases. The currents in inductive power compensation, when compared to the currents in capacitive power compensation, exhibit approximately a 30% reduction of THD. For example, when ϕ is 20°, the THD values of the capacitive and inductive currents at 17-A are 12.9% and 8.7%, respectively, because the inductive current does not have cusp distortions. As a result, inductive power compensation yields a higher amount of reactive power (when only absolute values of reactive power are compared) at the same phase angle when Figure 3.13(b) and Figure 3.15(b) are compared.

The grid current THD highly depends on load currents and converter currents. If the load power is much greater and more sinusoidal than that of the converter, the grid current

THD is less affected by the converter current distortion when RPC is enabled, and vice versa. If there is no load current, the grid current is identical to the converter current. Since the converter current THD is dependent on many electrical parameters such as the grid voltage, converter power rating, and maximum shifted phase angle, each converter has different RPC capabilities even if the power rating of the converter is similar with others. From Figure 3.13(a) and 15(a) with regard to our test environment, the maximum shifted phase angle, which should not cause current THD higher than 5%, can be estimated. Then, using its maximum shifted phase angle and converter power ratings, the maximum reactive power can be estimated theoretically in Figure 3.13(b) and 3.15(b). In conclusion, approximately up to 15% and 30% of available power from a 1.2kVA unidirectional converter can be supplied for capacitive and inductive power, respectively. From a single converter, this capability is relatively small, but RPC capabilities can be multiplied by utilizing aggregated unidirectional converters as shown in Figure 3.10.

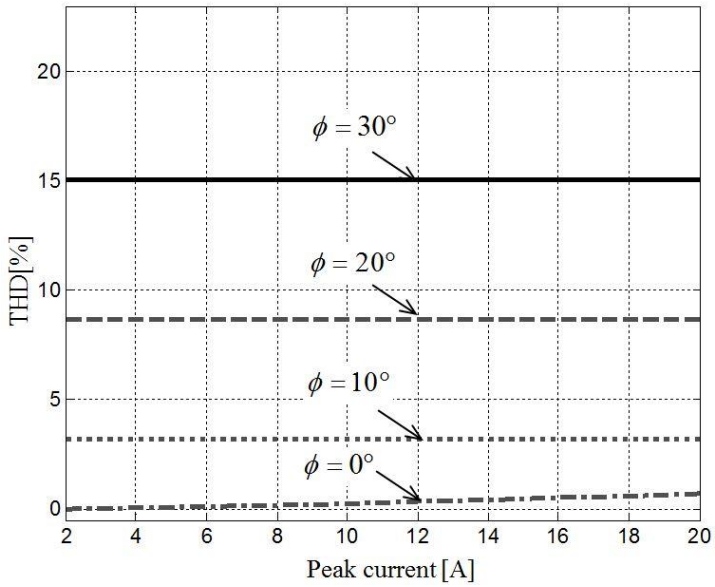

(a) THD versus peak current for different ϕ

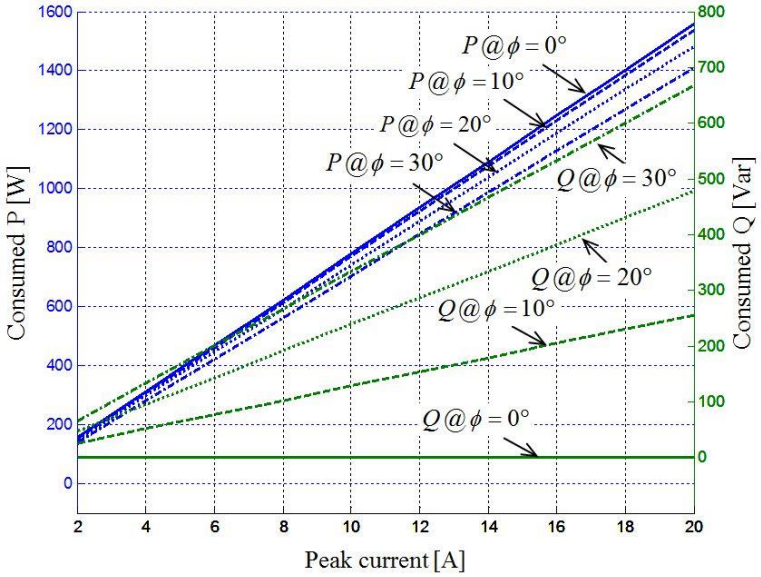

(b) active power and reactive power versus peak current for different ϕ

Figure 3.15 Analytical results in inductive power compensation mode.

3.3.4 Estimation of current THD

Although the current distortion levels based on the emulated current models in (3.12) and (3.21) are mathematically predicted in previous sections, actual distortion levels under practical implementations might deviate from these theoretical results because the quality of current waveforms correlate closely with many hardware and software components, such as the performances of the current compensator, filters and PLL, as well as the noise immunity of the sensors and the linearity of the inductor [61]. Due to these inherent imperfections, commercial ac-dc PFC converters in unity power factor mode ordinarily have THD values in the range of 2% to 5%. Demonstrating this, Figure 3.16 shows the THD values acquired experimentally from our proto-type PFC board. Since this

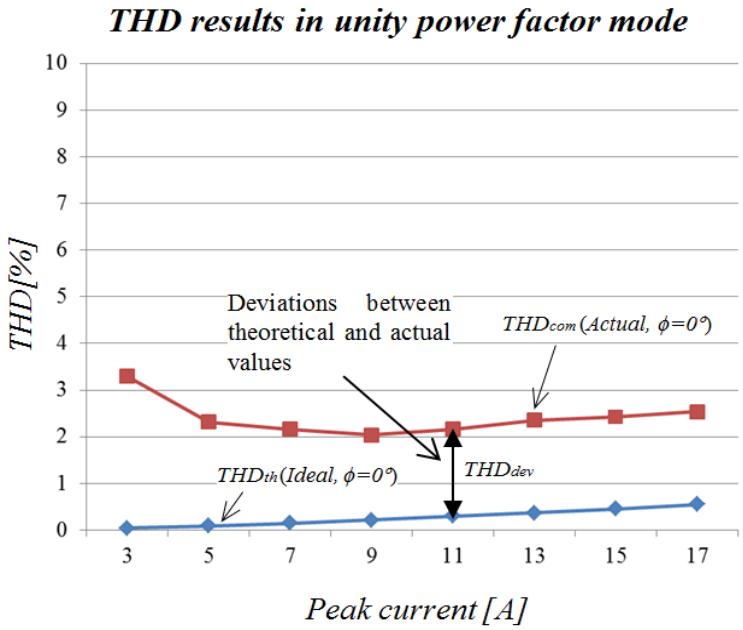

Figure 3.16 Actual harmonic distortion levels in a unity power factor mode.

imperfection from real circuits relates to the real current waveforms of the converter, it also affects THD values of reactive power current and causes the deviation between the theoretical and actual THD values. Therefore, the actual THD value considering this deviation can be represented approximately as

$$THD_{com} \approx THD_{th} + THD_{dev} \tag{3.25}$$

where THD_{th} is the theoretical THD value from (3.18) and THD_{dev} is an averaged deviation based on experimental results in unity power factor mode. In Figure 3.16, THD_{dev} is 2.14% which will be used for calculating the estimated THD in (3.25).

3.4 Simulation results

In order to validate the effectiveness and performance of the proposed control method for a unidirectional ac-dc boost converter, a 2-kW bridgeless PFC converter model, a nonlinear load and a linear load are implemented in MATLAB/Simulink. For a comparative evaluation of performances, the three converter operation modes are simulated: 1) HCC mode, 2) RPC mode, and 3) combined operations of HCC and RPC.

Figure 3.17 shows the simulation results in HCC mode when a single-phase rectifier with 80% current THD as a nonlinear load is connected to the unidirectional ac-dc boost converter at the PCC. The PFC operation begins with a 200 V dc-bus voltage reference while the current THD is 3% and the PF is 0.993. However, the grid THD increases as it becomes polluted with the harmonic current from the nonlinear load, resulting in 17% THD and 0.975 PF. At 0.2s, the operation mode of the converter is changed from PFC to HCC. It

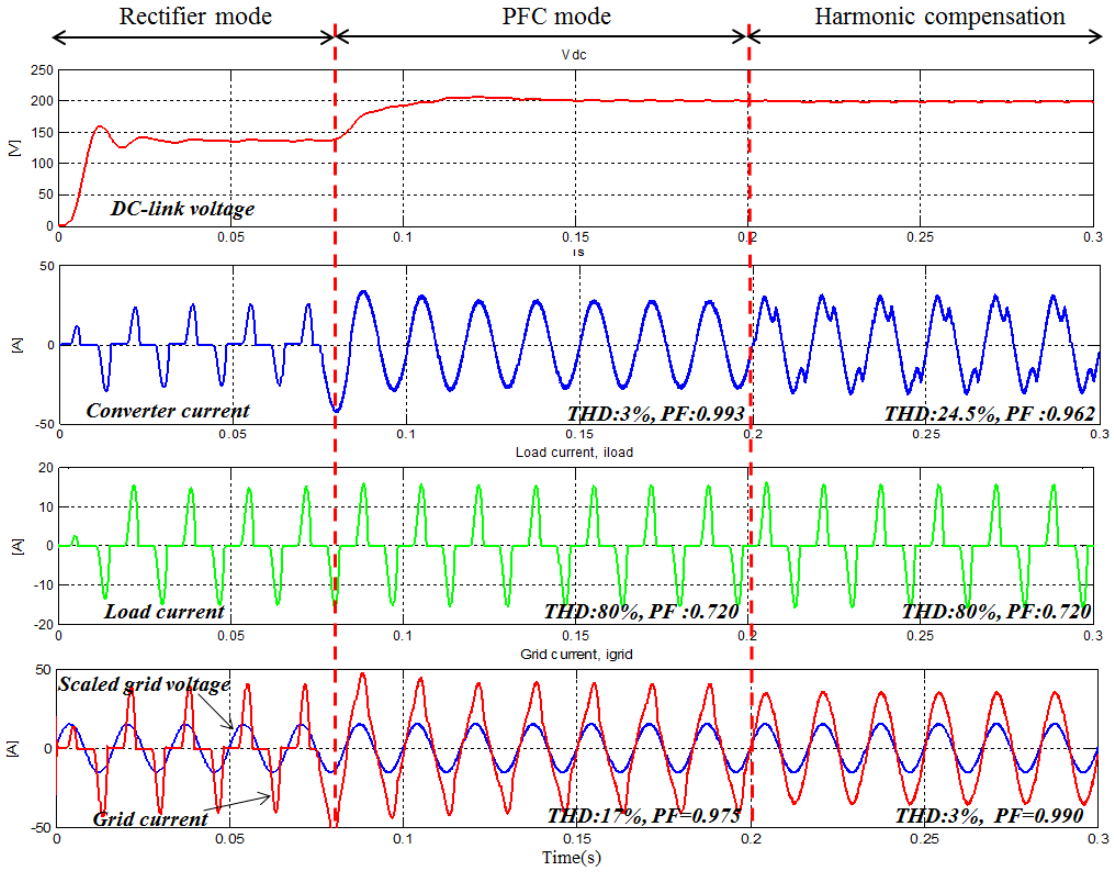

Figure 3.17 Simulation results in HCC mode.

can be observed that the grid current is a nearly sinusoidal waveform with 3% THD and 0.990 PF as a result of canceling the harmonic current at the load side.

Figure 3.18 shows the simulation results in RPC mode when a single-phase induction motor connected to the unidirectional ac-dc boost converter at the PCC is used as linear load with a poor PF of 0.8. It can be observed that the power factor of the grid is improved from 0.948 to 0.976 when the converter generates 500-Var in RPC mode. However, the THD of the grid current increases from 1.3% to 8% due to inherent distortions of reactive power current in unidirectional ac-dc boost converters. Thus, as

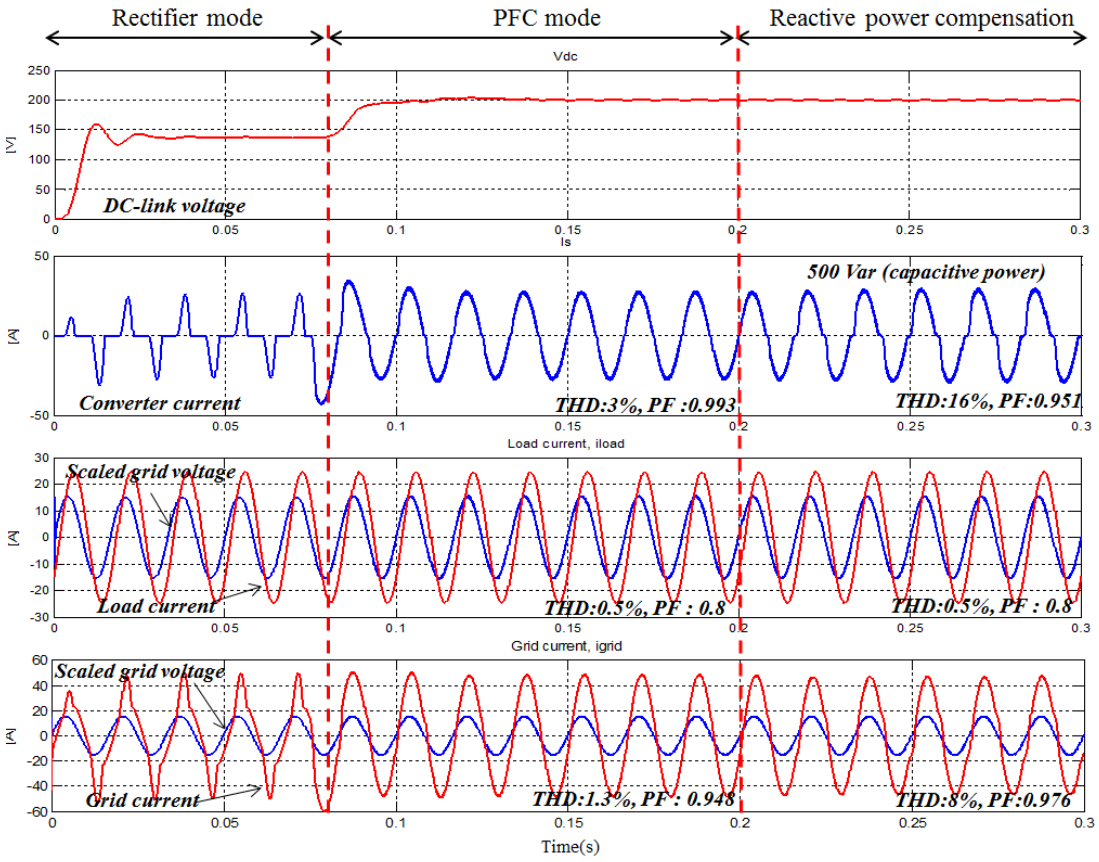

Figure 3.18 Simulation results in RPC mode.

explained in previous sections, the amount of reactive power used for compensation should be limited to maintain low THD of the grid current.

Figure 3.19 shows the simulation results for combined operations of HCC and RPC when the two emulated loads used in previous simulations are connected at the PCC. When the converter is operating in PFC mode, the PF and THD of the grid current are 0.941 and 10%, respectively. When HCC and RPC begin simultaneously, the resulting grid power

quality improves to a PF of 0.974 and 5% THD. This means that the grid power quality is enhanced as a result of the proposed control method. If more converters are available at the PCC and the total amount of RPC can be larger with smaller assignments of RPC of individual converters, the grid current will be more sinusoidal and in phase with the grid voltage. Simulation results are summarized in Table 3.1.

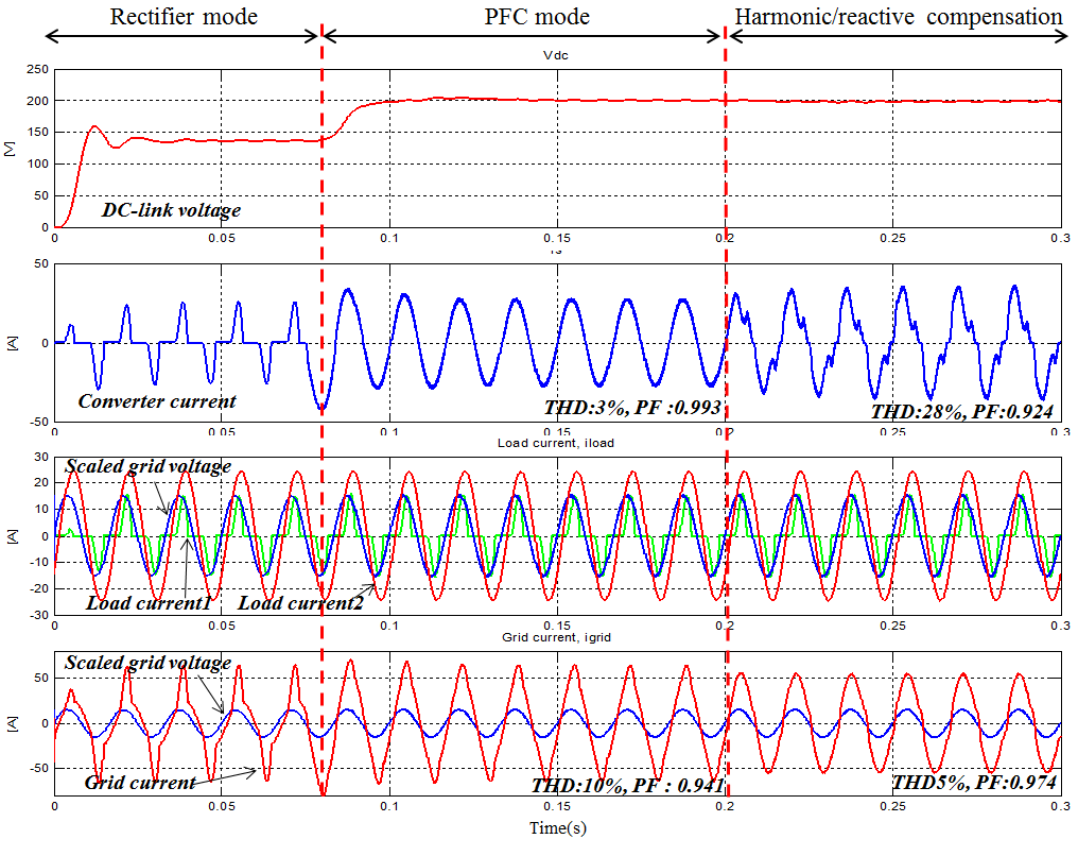

Figure 3.19 Simulation results in combined HCC and RPC mode.

Table 3.1 Summary of simulation results

Mode	Items	Unidirectional PFC converter		Load1 (nonlinear)	Load2 (linear)	Grid	
		Conv.	Proposed			Conv.	Proposed
HCC	*P* (W)	2000	2000	550	N/A	2550	2550
	Q (Var)	0	0	200	N/A	200	200
	THD (%)	3%	24.5%	80%	N/A	17%	3%
	P.F	0.993	0.962	0.720	N/A	0.975	0.990
RPC	*P* (W)	2000	2000	N/A	1500	3500	3500
	Q (Var)	0	-500	N/A	1100	1100	600
	THD (%)	3%	16%	N/A	0.5%	1.3%	8%
	P.F	0.993	0.951	N/A	0.800	0.948	0.976
HCC + *RPC*	*P* (W)	2000	2000	550	1500	4050	4050
	Q (Var)	0	-500	200	1100	1300	800
	THD (%)	3%	28%	80%	0.5%	10%	5%
	P.F	0.993	0.924	0.720	0.800	0.941	0.974

3.5 Experimental results

A 1.2-kW dual boost PFC converter was implemented in order to validate the proposed system. The passive and electronic loads used as linear and non-linear loads are connected with the grid and converter at the PCC. Figure 3.20 shows the experimental test bench and Table 3.2 lists some important experimental values.

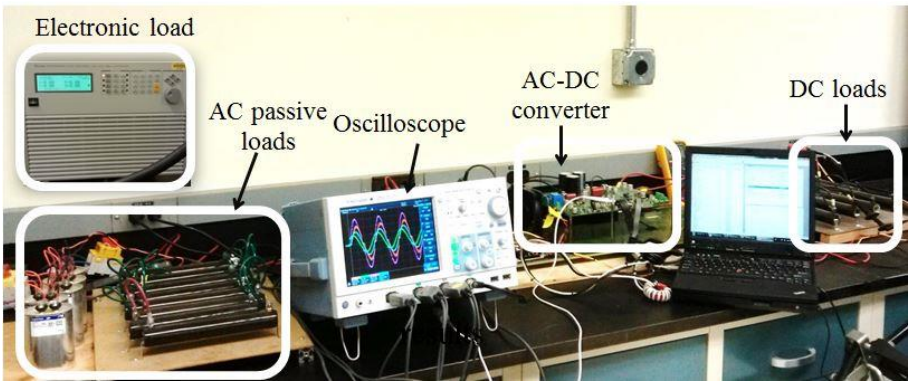

Figure 3.20 Test bench set-up.

Table 3.2 Experimental setup parameters

System parameter	***Values***
AC Source Voltage	110 Vrms / 60Hz
Rated Power	700 W
Switching Frequency	20 kHz
Boost Inductor	1.4 mH (split into two in series)
DC capacitor	2040 μF
DSP	TMS320F28035 (TI)
Power device	FPDB60PH60B (FAIRCHILD)
Grid emulator	3120-AMX (PACIFIC)
Load emulator	63803 (CHROMA) and ***RLC*** loads

3.5.1 Estimating current distortion levels

The estimated, simulated and measured output current and grid voltage waveforms in different operation modes are presented in Figure 21 and Figure 22 as an example to show the effectiveness of the proposed approach for estimating current distortion levels in RPC mode, where the peak current and phase references are 17-A and 20º, respectively. The waveforms of measured currents are nearly identical to the waveforms of the estimated

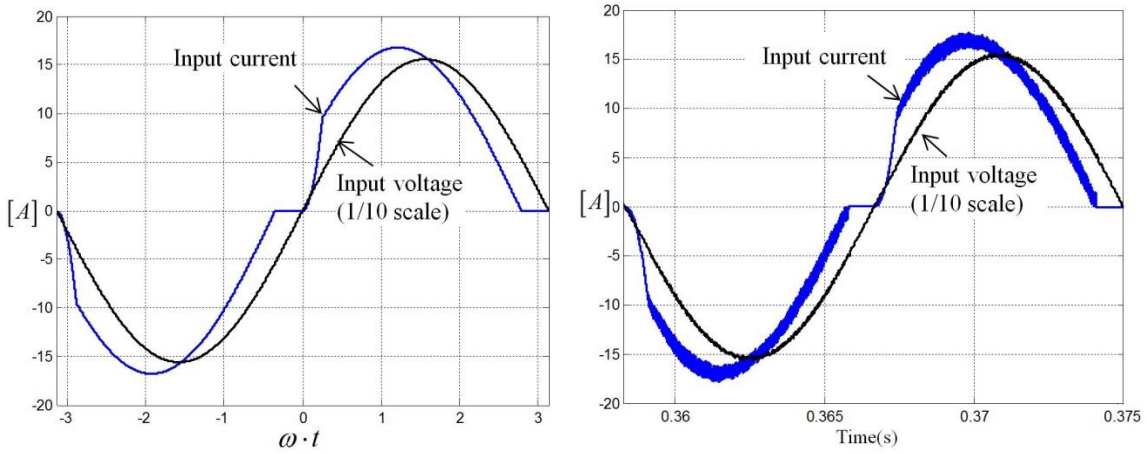

(a) estimated result (THD_{com}: 15. 1%) (b) simulation result (THD: 15.1%)

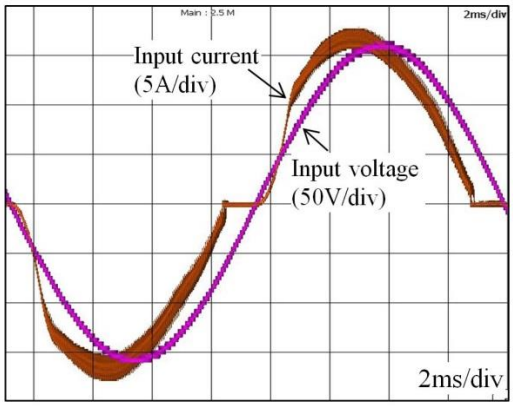

(c) experimental result (THD: 15.5%)

Figure 3.21 Comparison of waveforms in capacitive power compensation (I_s^*=17A, ϕ=20º).

and simulated results. In agreement with the analytical results, the capacitive current suffers from the zero-current and cusp distortions as shown in Figure 3.21, whereas the inductive current, as shown in Figure 3.22, is distorted only by the zero-current distortion.

Figure 3.23 shows test results comparing the measured THD values with the estimated values. The THD differences between the estimated THD from (3.25) and measured THD values from experimental tests are below 1% and the total averaged THD

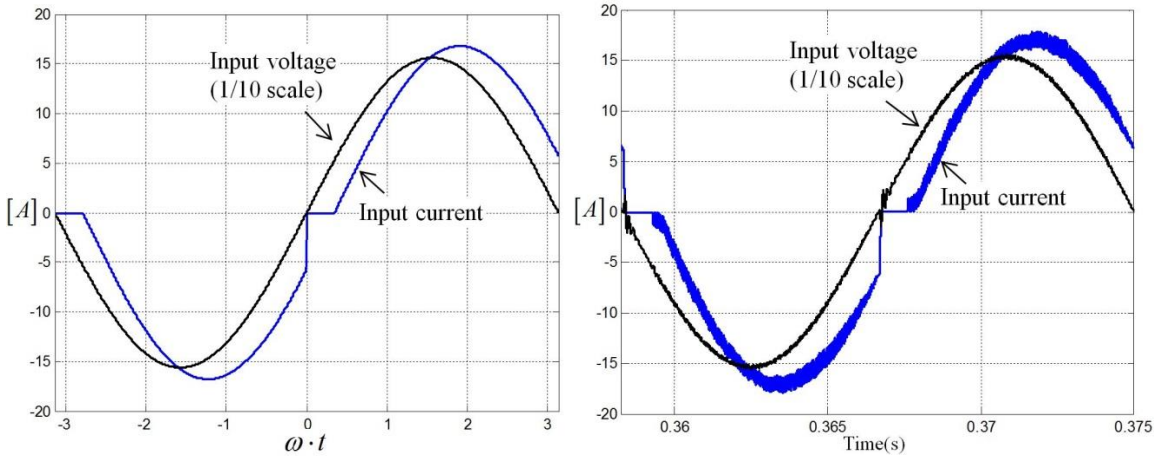

(a) estimated result (THD_{com}: 10.9%) (b) simulation result (THD: 10.7%)

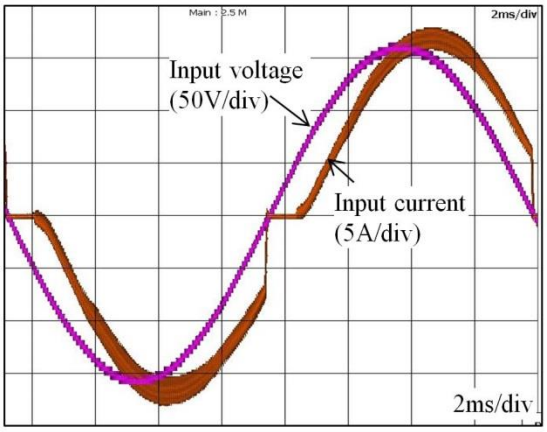

(c) experimental result (THD: 10.3%)

Figure 3.22 Comparison of waveforms in inductive power compensation (I_S^*=17A, ϕ=20°).

difference is approximately 0.3%. In addition, it can be observed clearly that the measured THD values in capacitive power compensation mode tend to increase as the peak current and shifted-phase-angle increase, whereas the measured THD values in inductive power compensation are inclined to be constant regardless of the magnitude of the current at a fixed phase angle. These features match the previous analytical results. Hence, the experimental results demonstrate that the proposed analytical approach is an effective solution for estimating current distortion levels in unidirectional ac-dc boost converters with RPC modes.

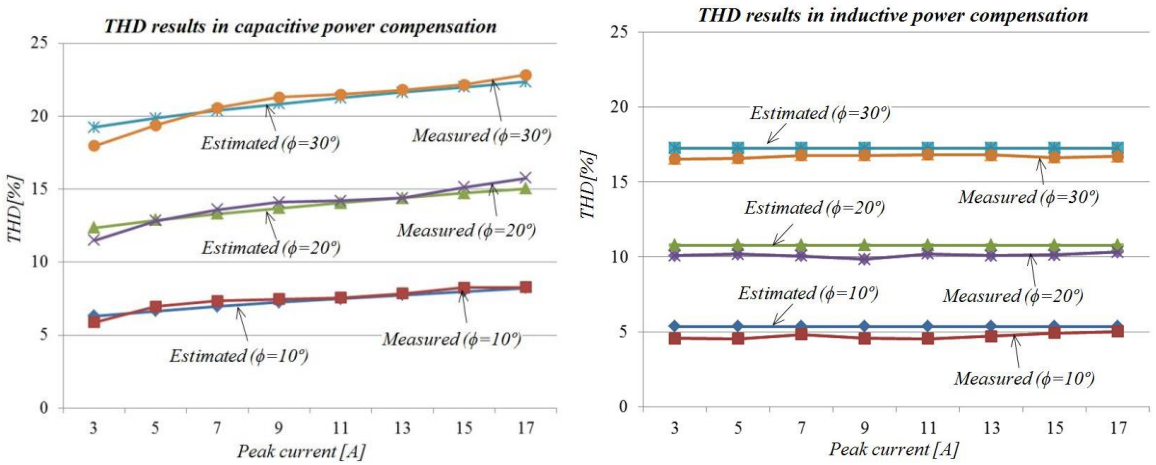

(a) capacitive power compensation (b) inductive power compensation

Figure 3.23 Experimental results for THD of input currents.

3.5.2 Harmonic current compensation

Figure 3.24 shows the experimental results in HCC mode when an emulated nonlinear load with 82% THD current is connected to the unidirectional ac-dc boost converter operating at about 700-W at the PCC. Before HCC mode is enabled, the converter current THD is 2.7% and the PF is 0.994 while the grid THD is polluted with the harmonic current from the nonlinear load, resulting in 15.5% THD with a peak-shape waveform as shown in Figure 3.24(a). However, after HCC mode is enabled and the converter current is intentionally distorted, it can be observed that the grid current can be a sinusoidal waveform with 4.5% THD, along with improved power factor as a result of canceling the load harmonic current as shown in Figure 3.24(b) and 3.24(c).

3.5.3 Reactive power compensation

Figure 3.25 shows the experimental results in RPC mode when a passive load consisting of several resistors and capacitors connected to the unidirectional ac-dc boost converter at the PCC is used as a linear load with a poor PF of 0.779, and generating 262-Var. Before RPC mode is enabled, the grid power factor decreases to 0.963 due to this capacitive load, even under the unity power factor of the converter as shown in Figure 3.25(a). After RPC mode is enabled, the converter consumes 300-Var. It can be observed that the power factor of the grid is improved from 0.963 to 0.992 as shown in Figure 3.25(b). However, the THD of the grid current increases from 1.89% to 3.93% as shown in Figure 3.25(c) due to inherent distortions of reactive power current in unidirectional ac-dc

boost converters as explained in previous sections. Thus, the amount of reactive power used for compensation should be limited to maintain low THD of the grid current.

3.5.4 Combined compensation mode

Figure 3.26 shows the experimental results for combined operations of HCC and RPC when the two loads used in previous experimental tests are connected at the PCC. When the converter is operating in PFC mode, the grid PF and the THD of the grid current are 0.960 and 11.2%, respectively. HCC and RPC begin simultaneously, and the resulting grid power quality improves to 0.992 P.F and 4% THD at the same time. From experimental results, the grid power quality can be partially enhanced through the proposed versatile control strategy, even though a unidirectional ac-dc boost converter is implemented instead of a bidirectional converter. Experimental results under all test conditions are summarized in Table 3.3.

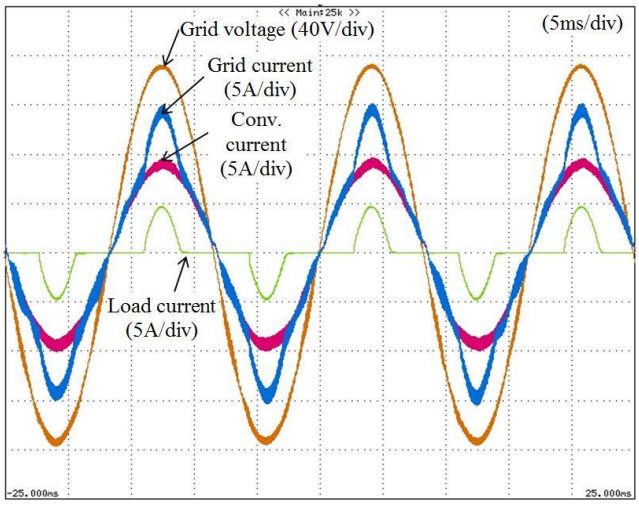

(a) before HCC

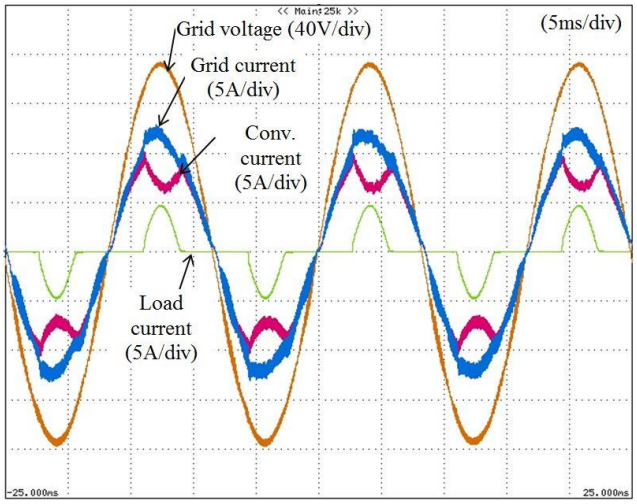

(b) after HCC

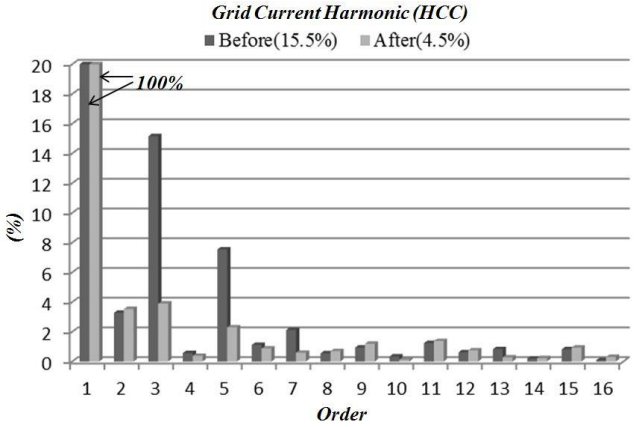

(c) harmonic analysis of the grid current

Figure 3.24 Experimental results in harmonic compensation mode.

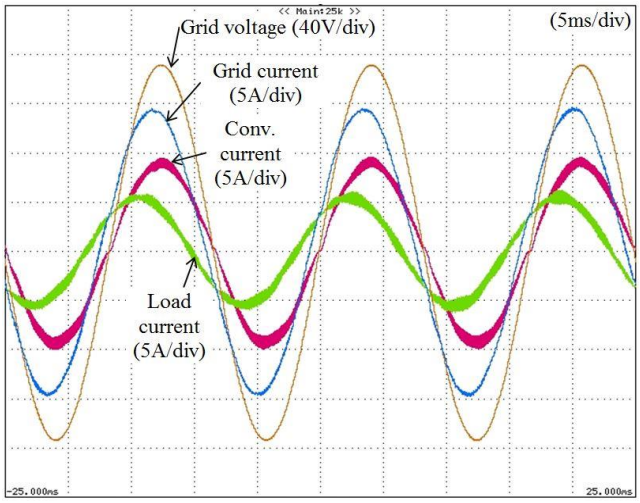

(a) before RPC

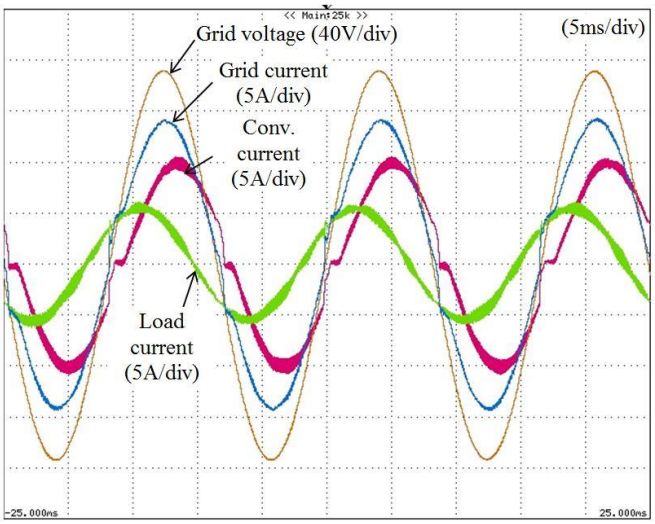

(b) after RPC

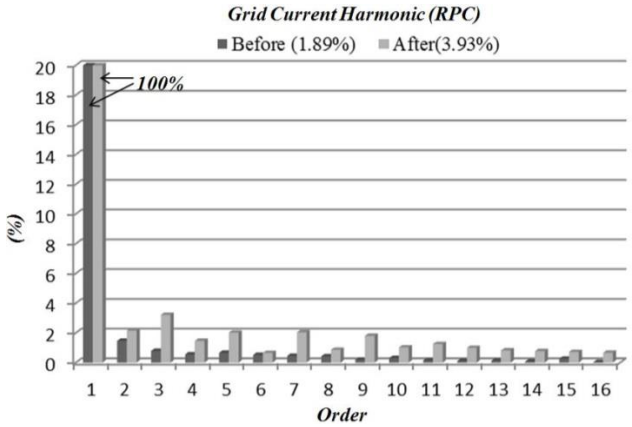

(c) harmonic analysis of the grid current

Figure 3.25 Experimental results in reactive power compensation mode.

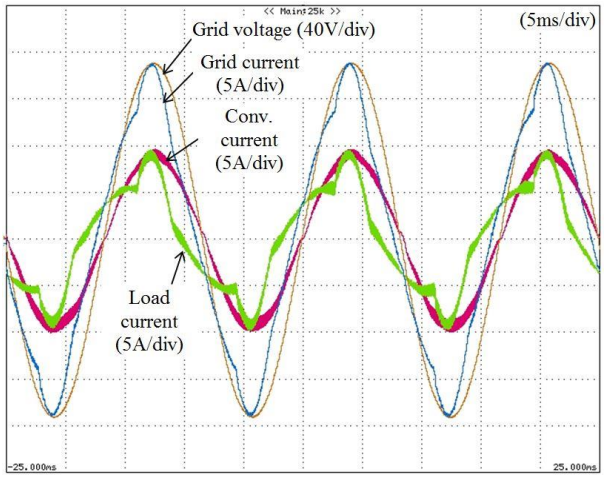

(a) before HCC and RPC

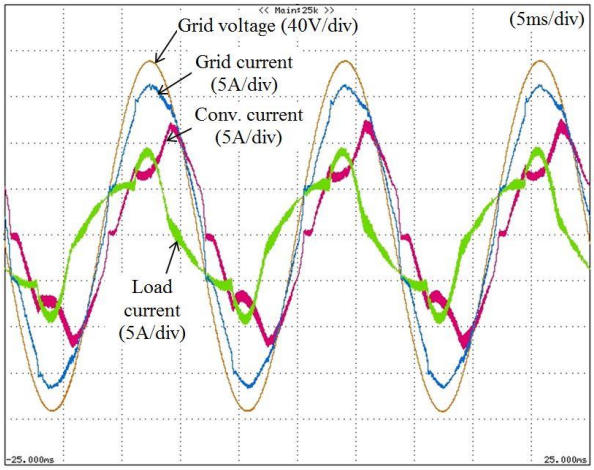

(b) after HCC and RPC

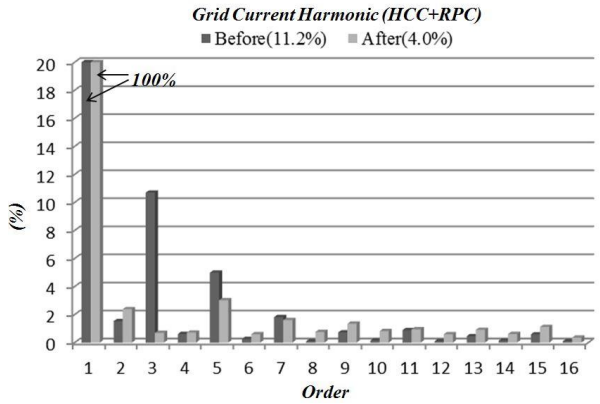

(c) harmonic analysis of the grid current

Figure 3.26 Experimental results in combined HCC and RPC mode.

TABLE 3.3 Summary of experimental results

Mode	Items	Unidirectional PFC converter		Load1 (nonlinear)	Load2 (linear)	Grid	
		Conv.	Proposed			Conv.	Proposed
HCC	*P* (W)	695	695	165	N/A	905	905
	Q (Var)	-20	-125	145	N/A	160	50
	THD (%)	2.7%	17.1%	82.0%	N/A	15.5%	4.5%
	P.F	0.994	0.961	0.559	N/A	0.964	0.989
RPC	*P* (W)	695	695	N/A	330	1067	1067
	Q (Var)	-20	300	N/A	-262	-262	75
	THD (%)	2.7%	5.1%	N/A	0.86%	1.89%	3.93%
	P.F	0.994	0.908	N/A	0.779	0.963	0.992
HCC + *RPC*	*P* (W)	695	695	490		1225	1225
	Q (Var)	-20	360	-295		-290	90
	THD (%)	2.7%	16.2%	24.3%		11.2%	4.0%
	P.F	0.994	0.870	0.824		0.960	0.992

3.6 Summary

Since unidirectional ac-dc boost converters are already ubiquitously connected with ac power systems, existing unidirectional ac-dc boost converters possess the ability to improve substantially the stability of ac power systems by maximizing functionalities of aggregated unidirectional ac-dc boost converters. In this chapter, versatile control methods for the unidirectional ac-dc boost converter have been presented to enhance grid power quality through the combination of HCC and RPC, which can be a more economical solution for future smart grid applications. In addition, the framework for evaluation of the current distortion levels in unidirectional ac-dc boost converters when they are employed for RPC has been presented. The effectiveness of the proposed control method was

validated through simulation and experimental results showing improved power factor and total harmonic distortion of the grid. At the same time, it should be noted that due to the inherent limitations of the unidirectional ac-dc boost converter, the grid current will be distorted unintentionally when operating in RPC mode where the THD of capacitive current is worse than that of the inductive current due to extended cusp distortions. Hence, the amount of reactive power injected from an individual converter to the grid should be restricted. Although, combined operation of these aggregated converters, each restricted in RPC, can meet the reactive power demand while still effectively compensating for generated harmonics.

Chapter 4. Bidirectional converters

4.1 Introduction

Global concerns regarding environmental regulations and gradual depletion of fossil fuel resources have led to a new trend of generating power locally at the distribution level by using non-conventional or renewable energy sources such as wind turbines, photovoltaic panels, fuel cells and microturbines, generally referred to as distributed power system (DPS) or distributed generation (DG) [C5], [C6], [C8]. It exptects that these DPSs play a key role to realize micro-grid system, furthermore smart-grid system for better utilizations of power systems. For more efficient energy usage within limited available resources, energy storage systems and independent battery systems can also be considered as local DPSs [14]-[16].

It is common for converters of DPSs to have multiple-stage configurations consisting of dc-dc and dc-ac stages as shown in Figure 4.1. The dc-dc converter based on

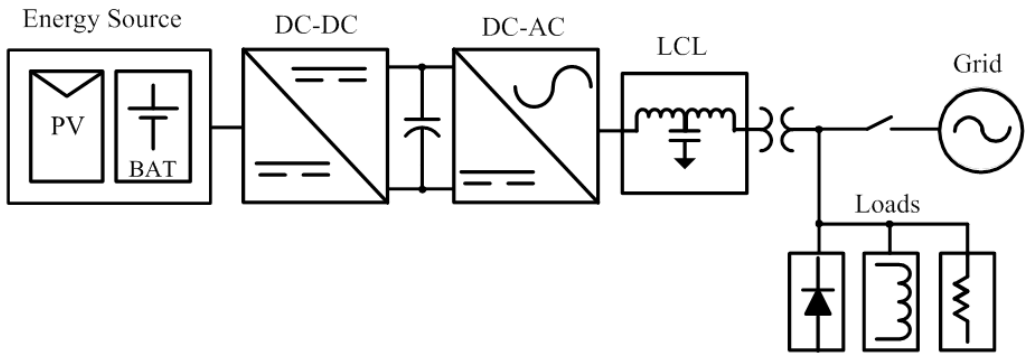

Figure 4.1 Typical distributed power system integrated bidirectional converters.

buck, boost, and buck-boost principles accomplishes certain objectives by using maximum power point tracking (MPPT) control of PV systems or state of charge (SOC) control of V2G systems. The bidirectional dc-ac converter referred to as the grid-tied converter delivers the regulated dc energy to the grid or local ac loads along with the satisfaction of stringent requirements of grid power quality [62].

In this chapter, modeling approach and control method of general bidirectional converters in PV and V2G applications are investigated and proposed for residential DPSs.

4.2 PV applications

PV systems can be classified according to their connection method between the PV modules and the power conditioning system (PCS) [63], [64]. In a conventional string configuration, shown in Figure 4.2(a), which can also be connected with several parallel strings, several series PV modules deliver electrical power to the grid and local ac loads through a central PCS. However, the central PCS configuration may cause mismatch losses of arrays due to differences in manufacturing, temperature, shading, and degradation conditions among the PV modules, resulting in a less efficient PV system. Also, failure of the PCS affects the reliability of the whole system. On the other hand, the microinverter configuration shown in Figure 4.2(b), also referred to as the module-integrated converter (MIC), uses individual small PCSs mounted on each PV module, allowing a simple “plug and play” installation and more localized control such as independent maximum power point tracking (MPPT) at the individual PV module scale [65]-[67]. Compared to the centralized PCS configuration, this system is expected to be more reliable with higher

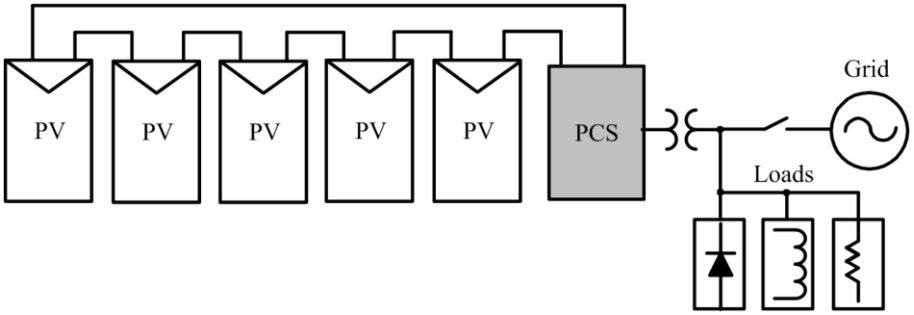

(a) conventional string type

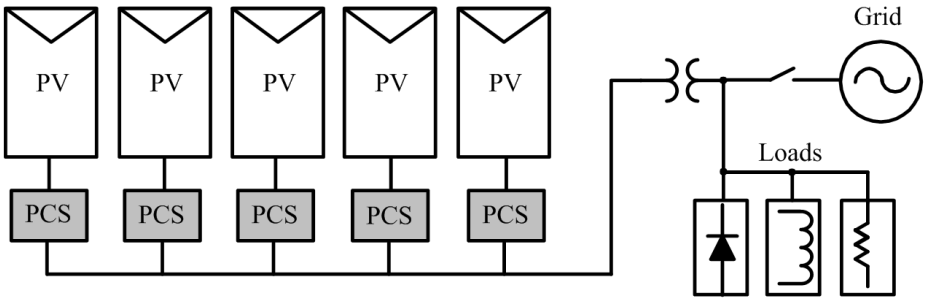

(b) multiple microinverters type

Figure 4.2 PV system configurations.

energy yield, which justifies its minor cost increase.

4.2.1 Modeling PV converters

As PV systems become more popular, higher efficiency and reliability are of increasing importance and system-level simulations are critical when addressing these needs. Modeling and simulation has thus become essential especially in order to choose the proper topology, select appropriate circuit component types and values, evaluate circuit performance, and complete a system design [68]-[70].

There are several methods to build power electronics models. Typically switching power devices and passive power elements such as inductors, capacitors, and resistors involved in the models. Dynamic models including switching actions may not be suitable for multiple microinverter aggregated system simulation in spite of their simple implementation and accurate transient responses. The increase in the number of microinverters in a system simulation yields significant computational burdens and long simulation times [71], [72]. Another approach is to use the average PWM switch model [73], [74] replacing the switches in the dynamic models with time-averaged models represented by voltage and current sources. With the average modeling method, some simulation accuracy is lost but the resulting simulation run time and setup time can be significantly reduced. The state-space average model is employed to ascertain a set of equations describing the system behavior over one switching period, which aids designers in understanding the physical relationship between control parameters and converter states [68], [70], [75]. Using an average model, the transfer function of the system can also be obtained, and larger simulation step sizes can be utilized with minimal loss of accuracy which leads to a faster simulation time. Consequently the state-space average model will be the most competitive modeling method in simulation studies for aggregated mulitple microinverters.

A number of papers have researched the state-space averaging model for various power converter topologies in different operating modes [71], [72], [76]-[82]. The proper analytical averaging model for discontinuous conduction mode (DCM) operation in the dc-dc converter has been studied in [71], which contains implicitly elements to generate a base

model applicable to both fixed and variable frequency operations. Many efforts have also been made to develop adequate seamless mode transitions from DCM to CCM and vice versa in simulation studies of dc-dc converters [77], [78]. Furthermore, the issue of parasitic components on these modeling methods is investigated in [72]. Recently the conventional converter configurations such as the boost, buck and fly-back converter tend to be combined and integrated with other power electronics circuits for high efficiency converters and thus their proper averaging model have been required. The boost converter with a voltage multiplier cell has been analyzed in [80] to derive its average model which is complex and requires the use of advanced techniques due to the resonant circuit. Not only small-signal model approaches, but also large-signal model approaches have been conducted to investigate large signal behaviors and capabilities in multiple dc-dc [76] or dc-ac [82] converters where a generalized state-space averaging method employing the Fourier series with time-dependent coefficients. However, these models cannot predict the complete dynamic behavior of these systems. While most papers focus on dc-dc converter modeling, a small number of papers have been presented on average modeling of dc-ac converters to approximate their behavior in grid-connected power electronics such as STATCOM, active power filters [83] and PV applications [84]. It should be noted that [71], [72], [76]-[84] have all addressed single-stage power converters and inverters, but average modeling of multiple-stage converters such as microinverters is still open to research along with the adequate simulation strategy that is necessary to improve simulation speed and accuracy of multiple cascaded converters, such as multiple PV microinverters in a microgrid.

The primary focus of this section is to introduce the simulation strategy for aggregated multiple microinverters by employing state-space average modeling of multi-stage power converters represented by a single-matrix-form (SMF). SMF can be derived by using the intermediate source model to link to converters with established average models, and thus this approach can facilitate integration of existing average models for cascaded, parallel, and many topologies. Since the proposed simulation strategy is based on the state-space average modeling technique which allows investigating small-signal behavior of the systems, it can capture important dynamics of PV microinverters in smaller power systems such as microgrids even under aggregated multiple converters, but switching transients that slow down simulations are over-ridden. The main advantages of the proposed approach are: 1) achieving a faster simulation time in research on aggregated multiple microinverter systems compared to dynamic switching models of converters; 2) providing better flexibility with easily interchangeable converter models; 3) understanding the relationship of state variables between multi-stage converters; and 4) simple extension to other power electronics conversion systems with multiple-stage configurations. It is important to note that the main purpose of this section is to introduce this intermediate source methodology in multiple-converter systems which can be extended to various topologies and applications, especially in the area of modeling and control of microgrids to capture finer dynamics with faster simulations that mask switching transients.

It is common for PV converters to have multiple-stage configurations consisting of dc-dc and dc-ac stages [63], [64], [85]. The dc-dc converter provides MPPT at the PV panel terminals while the dc-ac converter delivers PV power to the grid or local ac loads in the

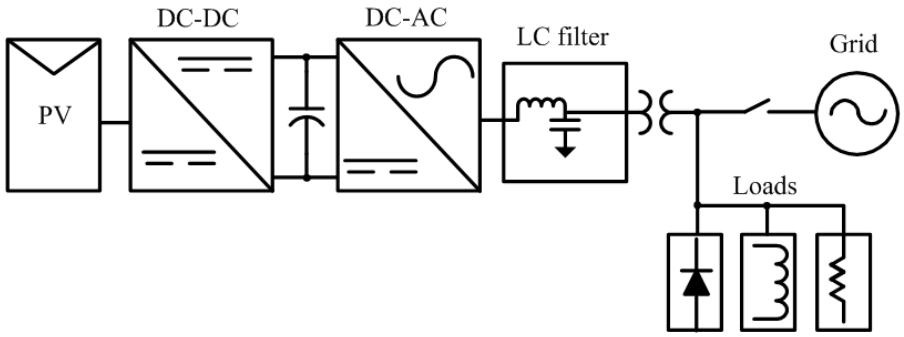

Figure 4.3 General PCS structure for converting PV power.

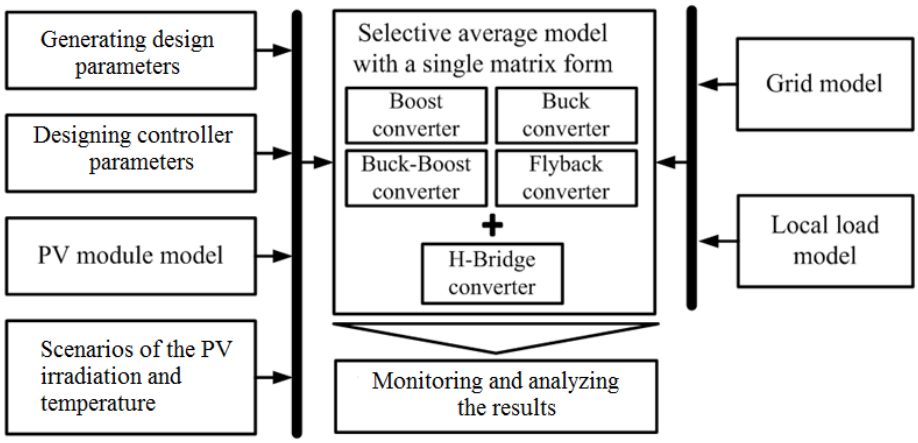

Figure 4.4 Proposed modeling approach for the multiple microinverters system.

second stage as shown in Figure 4.3. The proposed simulation approach to simulate the multiple microinverter system is shown in Figure 4.4. Several models are required for a PV system simulation—PV module model, power converter model, grid model and local load model. PV cell models are very common in the literature, especially those utilizing the current source and inverse diode configuration [86], [87]. Using this model, a 200W PV panel model is developed for use as the PV module model under different irradiance

conditions. As for the load model, a simple resistor model is used as the passive local load model since it yields simpler SMF. If reactive power needs to be consumed or generated by local loads, the resistive load model can be replaced with other inductive and capacitive loads or an RLC combination. The grid model encompasses a stiff single-phase voltage source with fixed voltage and frequency characteristics in series with the grid impedance consisting of a resistor and inductor. By using this model, it is possible to simulate all grid disturbances such as sag, swell, and interruptions, and adjust the voltage source to include voltage harmonics. Details of the converter dc-dc, dc-ac, and combined converter models are presented in this section.

While this section presents examples of specific dc-dc and dc-ac stages, adjusting the matrices in the average model of each stage to reflect other converter topologies is possible. The methodology proposed in this paper for integrating two average models of dc-dc and dc-ac stages as shown in Figure 4.5 can thus be followed.

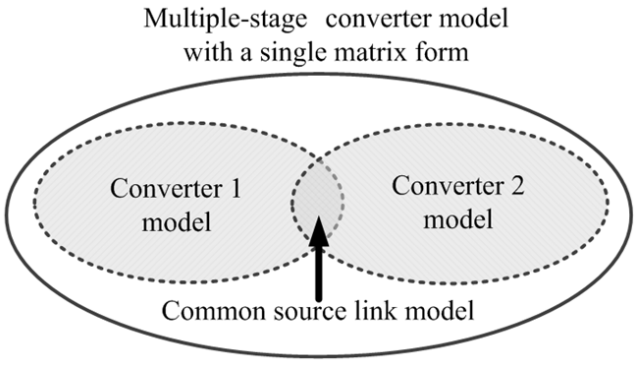

Figure 4.5 Single matrix form model for multiple-stage converter.

A SMF integrated with the dc-dc converter and dc-ac converter models is used for better flexibility when other topologies are used as it directly links the state variables between both energy conversion stages.

a) PV model

The most commonly used the equivalent circuit model to analyze the behavior of the PV cell is shown in Figure 4.6. The PV cell has a built-in series resistance, R_s, and shunt resistance, R_{sh}. In general, R_s, which is dependent on contacts and irradiances, needs to be very small to avoid any power dissipation, whereas R_{sh}, which is dependent on their materials, needs to be very large. Usually, the difference between the square of the power curve and the maximum power, known as the fill factor, is related to these resistances. The relationship between the PV output current, i_{pv}, and the PV output voltage, v_{pv}, known as the I–V characteristic of the PV cell can be defined as

$$i_{pv} = I_L - I_o\left(\exp\left(\frac{q\left(v_{pv}+i_{pv}R_s\right)}{nkT}\right)-1\right)-\frac{v_{pv}+i_{pv}R_s}{R_{sh}} \tag{4.1}$$

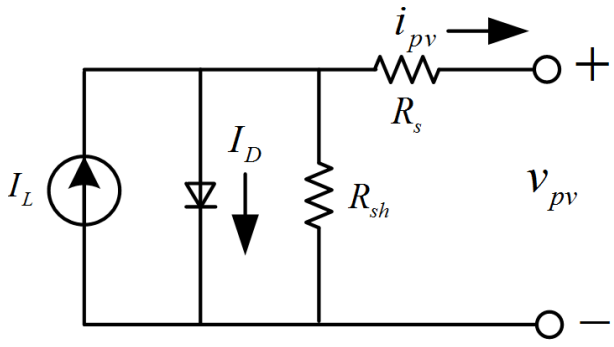

Figure 4.6 Equivalent circuit model for the PV cell.

where I_L is the light generated current that is proportional to the solar irradiation, I_o is the saturation current that mainly depends on the temperature, T, n is the ideality factor (from 1 to 2), k is the Boltzmann constant and q is the electron charge.

b) DC-DC converter average model

State-space average modeling is employed to obtain a set of differential equations to a selected converter topology [68], [70], [75]. The resulting model is expected to combine the dc-dc converter in continuous conduction mode (CCM) and dc-ac converter. Those equations are capable of describing the system behavior over one switching period. It is also desirable to include all parasitic effects in the state-space average model to predict the dynamic behavior and frequency response of the microinverter accurately [72]. The state space equation of the converter in CCM can be expressed as

$$\dot{\mathbf{x}}(t) = \left(q(t)\mathbf{A}_1 + (1-q(t))\mathbf{A}_2\right)\mathbf{x}(t) + \left(q(t)\mathbf{B}_1 + (1-q(t))\mathbf{B}_2\right)\mathbf{u}(t) \tag{4.2}$$

where $q(t)$ is the switching function corresponding to the power device's on/off states, $\mathbf{A}_k$ and $\mathbf{B}_k$ are the system matrices where k=1 or 2 depending on the switch status, and u(t) is an input vector. The low-frequency components of state variables such as the inductor currents, capacitor voltages and the output duty can be modeled by averaging over the switching period, T_s, and can be defined as,

$$\bar{\mathbf{x}}(t) = \frac{1}{T_s}\int_t^{t+T_s} \mathbf{x}(\tau)d\tau \tag{4.3}$$

where the bar symbol denotes the so-called fast average or true average of a state variable **x**(t). Using (4.3), the state average equation can be expressed as

$$\dot{\bar{\mathbf{x}}}(t) = \left(d(t)\mathbf{A}_1 + (1-d(t))\mathbf{A}_2\right)\bar{\mathbf{x}}(t) + \left(d(t)\mathbf{B}_1 + (1-d(t))\mathbf{B}_2\right)\bar{\mathbf{u}}(t) \tag{4.4}$$

where $d(t)$ is the duty cycle function.

Figure 4.7 depicts the grid-connected microinverter, consisting of a non-ideal boost converter and H-bridge inverter as an example. In order to obtain the state-space average model with a SMF, first of all, these converters can be separately considered as shown in Figure 4.8 and Figure 4.9.

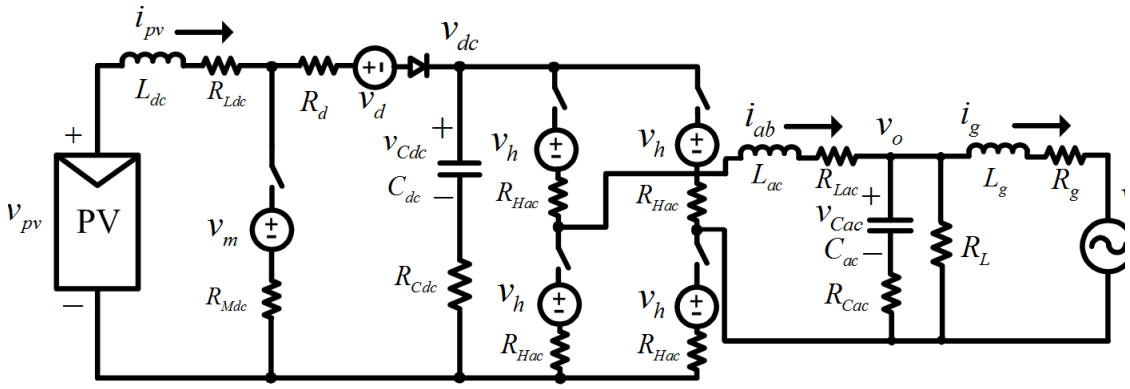

Figure 4.7 Circuit model for deriving the average model.

The circuit equations of these converters for turn-on and turn-off periods can be derived by applying Kirchhoff's voltage and current laws, and then the system matrices according to the switching status can be obtained. From the dc-dc boost converter as shown in Figure 4.8, the state-space average model can be defined as

$$\begin{aligned}\dot{\bar{\mathbf{x}}}_d(t) &= \mathbf{A}_d\bar{\mathbf{x}}_d(t)+\mathbf{B}_d\bar{\mathbf{u}}_d(t)\\ &=\left(D_{dc}(t)\mathbf{A}_{d1}+(1-D_{dc}(t))\mathbf{A}_{d2}\right)\bar{\mathbf{x}}_d(t)\\ &\quad+\left(D_{dc}(t)\mathbf{B}_{d1}+(1-D_{dc}(t))\mathbf{B}_{d2}\right)\bar{\mathbf{u}}_d(t)\end{aligned} \tag{4.5}$$

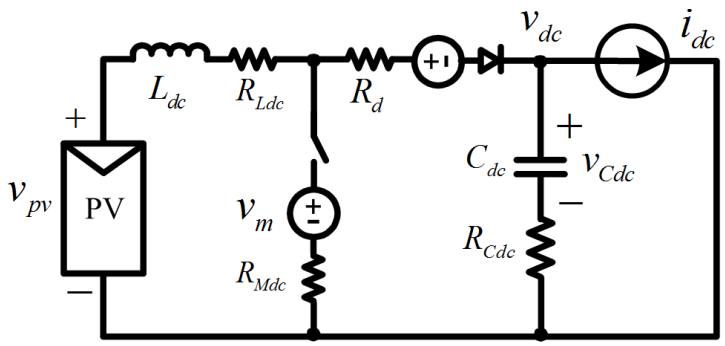

Figure 4.8 Circuit model for the dc-dc converter.

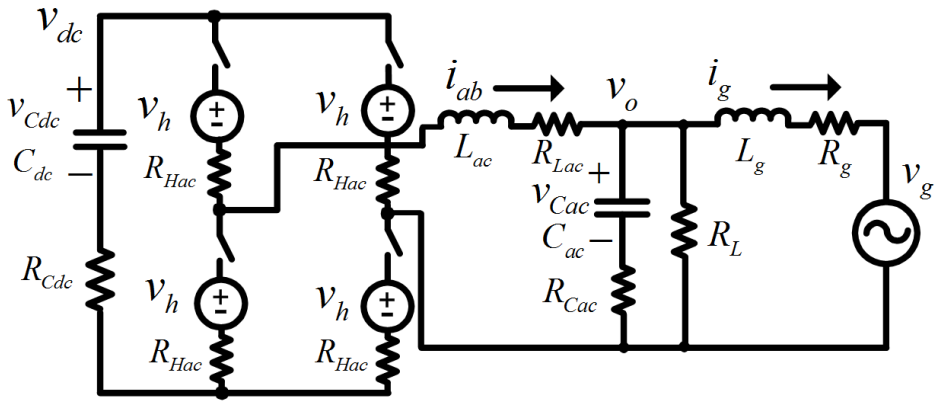

Figure 4.9 Circuit model for the dc-ac converter.

where $\mathbf{x}_d = [i_{pv}\ \ v_{Cdc}]^T$, $\mathbf{u}_d = [v_{pv}\ \ v_m\ \ v_d\ \ i_{dc}]^T$ and i_{pv} is the dc inductor current, v_{Cdc} is the link capacitor voltage, v_{pv} is the output voltage of the PV module, v_m is the drain-to-source voltage of the boost switch, v_d is the forward voltage of the diode, i_{dc} is the current in the dc-bus and D_{dc} is the duty ratio of the boost converter. Matrices $\mathbf{A}_{d1}$, $\mathbf{A}_{d2}$, $\mathbf{B}_{d1}$ and $\mathbf{B}_{d2}$ when

the switch is on and off are presented. The matrix $\mathbf{A}_{d1}$, $\mathbf{A}_{d2}$, $\mathbf{B}_{d1}$ and $\mathbf{B}_{d2}$ for the dc-dc converter is given by

$$\mathbf{A}_{d1} = \begin{bmatrix} -\dfrac{(R_{Ldc} + R_{Mdc})}{L_{dc}} & 0 \\ 0 & 0 \end{bmatrix} \tag{4.6}$$

$$\mathbf{B}_{d1} = \begin{bmatrix} \dfrac{1}{L_{dc}} & -\dfrac{1}{L_{dc}} & 0 & 0 \\ 0 & 0 & 0 & -\dfrac{1}{C_{dc}} \end{bmatrix} \tag{4.7}$$

$$\mathbf{A}_{d2} = \begin{bmatrix} -\dfrac{(R_{Ldc} + R_{Cdc} + R_d)}{L_{dc}} & -\dfrac{1}{L_{dc}} \\ \dfrac{1}{C_{dc}} & 0 \end{bmatrix} \tag{4.8}$$

$$\mathbf{B}_{d2} = \begin{bmatrix} \dfrac{1}{L_{dc}} & 0 & -\dfrac{1}{L_{dc}} & \dfrac{R_{Cdc}}{L_{dc}} \\ 0 & 0 & 0 & -\dfrac{1}{C_{dc}} \end{bmatrix} \tag{4.9}$$

Using these matrices and (4.5)-(4.9), matrices $\mathbf{A}_d$ and $\mathbf{B}_d$ presented with averaged values during one-sample time are

$$\mathbf{A}_d = \begin{bmatrix} -\dfrac{R_{Ldc} + D_{dc}R_{Mdc} + (R_{Cdc} + R_d)(1 - D_{dc})}{L_{dc}} & -\dfrac{1 - D_{dc}}{L_{dc}} \\ \dfrac{1 - D_{dc}}{C_{dc}} & 0 \end{bmatrix} \tag{4.10}$$

$$\mathbf{B}_{\mathrm{d}} = \begin{bmatrix} \dfrac{1}{L_{dc}} & -\dfrac{D_{dc}}{L_{dc}} & -\dfrac{1-D_{dc}}{L_{dc}} & \dfrac{(1-D_{dc})R_{Cdc}}{L_{dc}} \\ 0 & 0 & 0 & -\dfrac{1}{C_{dc}} \end{bmatrix} \tag{4.11}$$

where L_{dc} is the boost inductor value, C_{dc} is the dc link capacitor value, R_{Ldc} and R_{Cdc} are parasitic resistors of the passive components, R_{Mdc} and R_d are the switch on-resistance, respectively.

b) DC-AC Converter Average model

In a procedure similar to that discussed in the previous section, the average model of the H-bridge converter shown in Figure 4.9 is defined as,

$$\begin{aligned} \dot{\bar{\mathbf{x}}}_a(t) &= \mathbf{A}_a \bar{\mathbf{x}}_a(t) + \mathbf{B}_a \bar{\mathbf{u}}_a(t) \\ &= \left(D_{ac}(t)\mathbf{A}_{a1} + (1-D_{ac}(t))\mathbf{A}_{a2}\right)\bar{\mathbf{x}}_a(t) \\ &\quad + \left(D_{ac}(t)\mathbf{B}_{a1} + (1-D_{ac}(t))\mathbf{B}_{a2}\right)\bar{\mathbf{u}}_a(t) \end{aligned} \tag{4.12}$$

where $\mathbf{x}_a = [i_{ab} \quad v_{Cac} \quad i_g]^T$, $\mathbf{u}_a = [v_{Cdc} \quad v_h \quad v_g]^T$, i_{ab} is the ac inductor current, v_{Cac} is the capacitor voltage in the LC filter, i_g is the grid current, v_h is the drain-to-source voltage of the H-bridge switch, v_g is the grid voltage and D_{ac} is the duty ratio of the H-bridge converter. It is worthwhile to mention that the relationship between the average duty and modulation index (M) of the H-bridge converter can be expressed as $D_{ac}(t)=0.5+M\cdot\sin(\omega t)$ where ω is the grid frequency since the average duty is between 0 and 1. The matrix $\mathbf{A}_{a1}$, $\mathbf{A}_{a2}$, $\mathbf{B}_{a1}$ and $\mathbf{B}_{a2}$ for the dc-ac converter is given by

$$\mathbf{A}_{a1}=\begin{bmatrix} \dfrac{-\begin{pmatrix}2R_{Hac}+R_{Lac}\\ +R_{Cac}\Psi+R_{Cdc}\end{pmatrix}}{L_{ac}} & -\dfrac{\Psi}{L_{ac}} & \dfrac{R_{Cac}\Psi}{L_{ac}} \\ \dfrac{\Psi}{C_{ac}} & -\dfrac{\Psi}{C_{ac}R_L} & -\dfrac{\Psi}{C_{ac}} \\ \dfrac{R_{Cac}\Psi}{L_g} & \dfrac{\Psi}{L_g} & -\dfrac{\Psi}{L_g}\begin{pmatrix}R_{Cac}+R_g\\ +\dfrac{R_{Cac}R_g}{R_L}\end{pmatrix} \end{bmatrix} \tag{4.13}$$

$$\mathbf{B}_{a1}=\begin{bmatrix} \dfrac{1}{L_{ac}} & -\dfrac{2}{L_{ac}} & 0 \\ 0 & 0 & 0 \\ 0 & 0 & -\dfrac{1}{L_g} \end{bmatrix} \tag{4.14}$$

$$\mathbf{A}_{a2}=\begin{bmatrix} \dfrac{-\begin{pmatrix}2R_{Hac}+R_{Lac}\\ +R_{Cac}\Psi+R_{Cdc}\end{pmatrix}}{L_{ac}} & -\dfrac{\Psi}{L_{ac}} & \dfrac{R_{Cac}\Psi}{L_{ac}} \\ \dfrac{\Psi}{C_{ac}} & -\dfrac{\Psi}{C_{ac}R_L} & -\dfrac{\Psi}{C_{ac}} \\ \dfrac{R_{Cac}\Psi}{L_g} & \dfrac{\Psi}{L_g} & -\dfrac{\Psi}{L_g}\begin{pmatrix}R_{Cac}+R_g\\ +\dfrac{R_{Cac}R_g}{R_L}\end{pmatrix} \end{bmatrix} \tag{4.15}$$

$$\mathbf{B}_{a2}=\begin{bmatrix} -\dfrac{1}{L_{ac}} & -\dfrac{2}{L_{ac}} & 0 \\ 0 & 0 & 0 \\ 0 & 0 & -\dfrac{1}{L_g} \end{bmatrix} \tag{4.16}$$

Using these matrices (4.12)-(4.16), matrices $\mathbf{A}_a$ and $\mathbf{B}_a$ for averaged values during one-sample time are given by

$$\mathbf{A}_a = \begin{bmatrix} -\dfrac{\left(\begin{matrix}2R_{Hac}+R_{Lac}\\ +R_{Cac}\Psi+R_{Cdc}\end{matrix}\right)}{L_{ac}} & -\dfrac{\Psi}{L_{ac}} & \dfrac{R_{Cac}\Psi}{L_{ac}} \\ \dfrac{\Psi}{C_{ac}} & -\dfrac{\Psi}{C_{ac}R_L} & -\dfrac{\Psi}{C_{ac}} \\ \dfrac{R_{Cac}\Psi}{L_g} & \dfrac{\Psi}{L_g} & -\dfrac{\Psi}{L_g}\left(\begin{matrix}R_{Cac}+R_g\\ +\dfrac{R_{Cac}R_g}{R_L}\end{matrix}\right) \end{bmatrix} \tag{4.17}$$

where $\Psi = \dfrac{R_L}{R_L + R_{Cac}}$, and,

$$\mathbf{B}_a = \begin{bmatrix} \dfrac{(2D_{ac}-1)}{L_{ac}} & -\dfrac{2}{L_{ac}} & 0 \\ 0 & 0 & 0 \\ 0 & 0 & -\dfrac{1}{L_g} \end{bmatrix} \tag{4.18}$$

where, L_{ac} is the ac inductor value, C_{ac} is the capacitor value in the LC filter, R_{Lac} and R_{Cac}, are parasitic resistors of the passive components, R_L is the local load resistance, and L_g and R_g reflect the grid impedance.

c) Combing two convertet models

As the next step, using the relationship between the dc-bus current and output current, two state-space average models obtained in (4.5) and (4.12) can be combined into SMF since the common source in the previously derived two state-space average model is the dc-bus current. Thus, the dc-bus current can be represented by ac current and ac duty in the H-bridge converter as,

$$\overline{i}_{dc} = (2D_{ac} - 1)\overline{i}_{ab} \tag{4.19}$$

It is notable in (4.19) that the common source model causes the dc-bus current to include ac ripples that are twice the ac output frequency, which is also reflected to dc-bus voltage. Moreover, the dc voltage v_{dc} and the output ac voltage v_o can be expressed as

$$\overline{v}_{dc} = R_{Cdc}\overline{i}_{pv} + \overline{v}_{Cdc} - R_{Cdc}\overline{i}_{ab} \tag{4.20}$$

$$\overline{v}_o = \left(\frac{R_L R_{Cac}}{R_L + R_{Cac}}\right)\overline{i}_{ab} + \left(\frac{R_L}{R_L + R_{Cac}}\right)\overline{v}_{Cac} - \left(\frac{R_L R_{Cac}}{R_L + R_{Cac}}\right)\overline{i}_g \tag{4.21}$$

The SMF state-space representation of the dc-dc and dc-ac converters is

$$\frac{d\overline{\mathbf{x}}(t)}{dt} = \mathbf{A}\overline{\mathbf{x}}(t) + \mathbf{B}\overline{\mathbf{u}}(t) \tag{4.22}$$

$$\overline{\mathbf{y}}(t) = \mathbf{C}\overline{\mathbf{x}}(t) \tag{4.23}$$

The state variables **x**, **u** and **y** in Figure 4.7, for grid connected mode are defined as

$$\overline{\mathbf{x}} = \begin{bmatrix} \overline{i}_{pv} & \overline{v}_{Cdc} & \overline{i}_{ab} & \overline{v}_{Cac} & \overline{i}_g \end{bmatrix}^T \tag{4.24}$$

$$\bar{\mathbf{u}} = \begin{bmatrix} \bar{v}_{pv} & \bar{v}_m & \bar{v}_d & \bar{v}_h & \bar{v}_g \end{bmatrix}^T \tag{4.25}$$

$$\bar{\mathbf{y}} = \begin{bmatrix} \bar{i}_{pv} & \bar{v}_{dc} & \bar{i}_{ab} & \bar{v}_o & \bar{i}_g \end{bmatrix}^T \tag{4.26}$$

Finally, matrices for the state, input, and output variables including the boost converter and H-bridge converter can be derived as

$$\mathbf{A} = \begin{bmatrix} & \mathbf{A}_d & & (1-D_{dc})(2D_{ac}-1)R_{Cdc}/L_{dc} & 0 & 0 \\ & & & -(2D_{ac}-1)/C_{dc} & 0 & 0 \\ 0 & (2D_{ac}-1)/L_{ac} & & & & \\ 0 & 0 & & \mathbf{A}_a & & \\ 0 & 0 & & & & \end{bmatrix} \tag{4.27}$$

$$\mathbf{B} = \begin{bmatrix} 1/L_{dc} & -D_{dc}/L_{dc} & -(1-D_{dc})/L_{dc} & 0 & 0 \\ 0 & 0 & 0 & 0 & 0 \\ 0 & 0 & 0 & -2/L_{ac} & 0 \\ 0 & 0 & 0 & 0 & 0 \\ 0 & 0 & 0 & 0 & -1/L_g \end{bmatrix} \tag{4.28}$$

$$\mathbf{C} = \begin{bmatrix} 1 & 0 & 0 & 0 & 0 \\ R_{Cdc} & 1 & -R_{Cdc} & 0 & 0 \\ 0 & 0 & 1 & 0 & 0 \\ 0 & 0 & R_{Cac}\Psi & \Psi & -R_{Cac}\Psi \\ 0 & 0 & 0 & 0 & 1 \end{bmatrix} \tag{4.29}$$

Moreover, the state-space average model for stand-alone mode can be obtained in (4.27)-(4.29) by setting the grid impedance (L_g and R_g) as infinity and the grid voltage (v_g) as zero.

d) Model validation

The state-space average model of the microinverter in SMF obtained in the previous section can be validated by simulating the model and comparing waveforms with a dynamic switching based model, as well as experimental testing. A 200W proto-type microinverter board is used for experimental tests. Since long input wires are used for the experimental test in the dc-dc converter side, extra input resistance R_{in} to be added to R_{Ldc} in each simulation. This validation procedure is intended to validate the plant dynamics in the average model, dynamic switching model, and experiments without control effects where the plant is the microinverter power stage. This is done using a resistive load with the main system parameters for simulation and experimental test are summarized in Table 4.1 and the input voltage is 30V to mimic that of a solar PV panel.

Table 4.1 Simulation and Experimental parameters for open-loop control model.

Parameters	Value	Parameters	Value
v_{pv}	25 ~ 40V	L_{dc}	2.63mH
v_g	110 Vrms	R_{Ldc}	0.15Ω
V_d	0.975V	L_{ac}	1.3mH
V_m	0.2V	R_{Lac}	0.075Ω
V_h	0.2V	C_{dc}	680μF
R_{In}	0.2Ω	R_{Cdc}	0.03Ω
R_{Mdc}	0.029Ω	C_{ac}	1μF
R_d	0.02Ω	R_{Cac}	0.01Ω
R_{Hac}	0.029Ω	L_g	3mH
R_L	62.5Ω	R_g	0.01Ω

Figure 4.10 shows the dynamic behavior of the dc inductor current, dc voltage and ac output current waveforms under open-loop duty disturbances of the dc-dc converter while the modulation index of the H-bridge converter remains constant at 0.935 in both MATLAB simulation models. At 0.35ms, a 1% step change from 0.800 to 0.792 in duties is applied. Simulation results show excellent correspondence between the proposed average model based on (4.27)-(4.29) and the dynamic switching model where the current and voltage values from established average model are in the middle of the dynamic model switching ripple. An experiment was carried out to ensure that the simulated models (average and dynamic) match a real setup under the same test conditions where IRFP4332PbF and MUR840G are used for power devices. As shown in Figure 4.11 and Table 4.2, experimental results are in agreement with simulation results in Figure 4.10, with the exception of the settling time which is sensitive to various experimental set-up characteristics such as PCB and line parasitic elements.

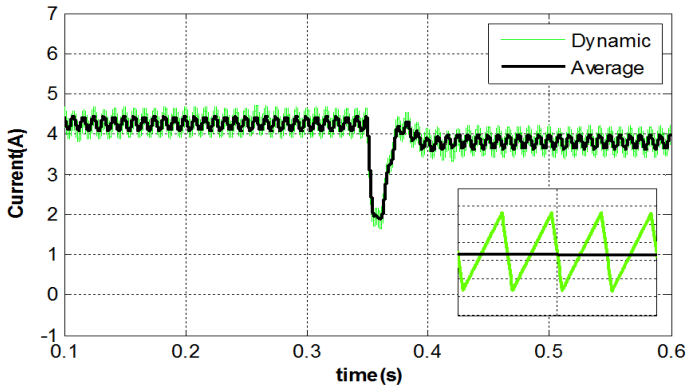

(a) PV current

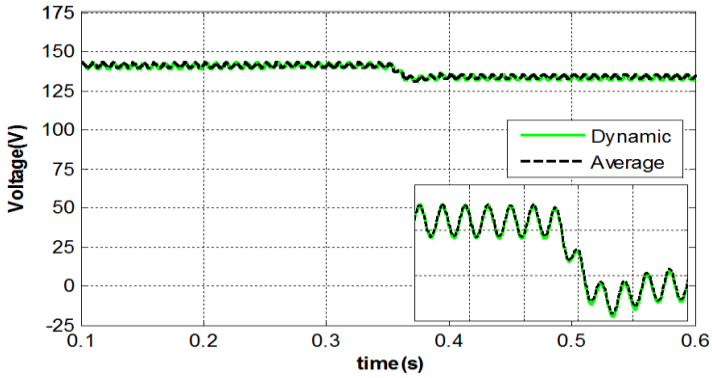

(b) Dc-bus voltage

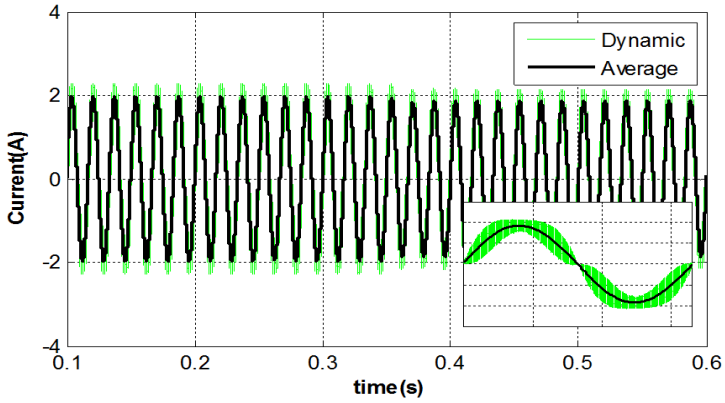

(c) Ac output current

Figure 4.10 Simulation results for a single microinverter under open-loop control with resistive load.

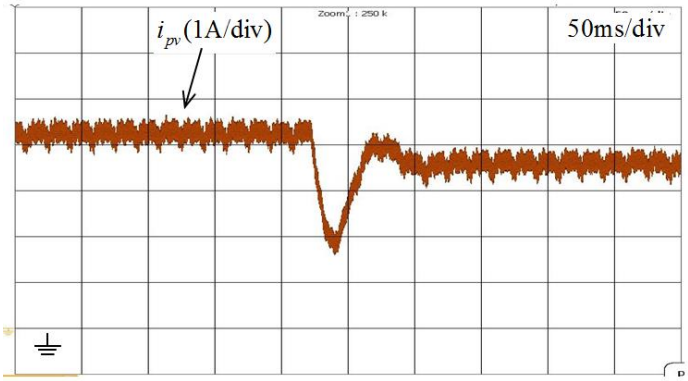

(a) PV current

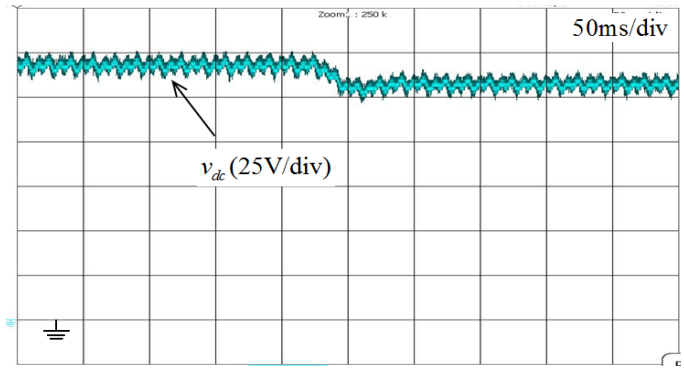

(b) Dc-bus voltage

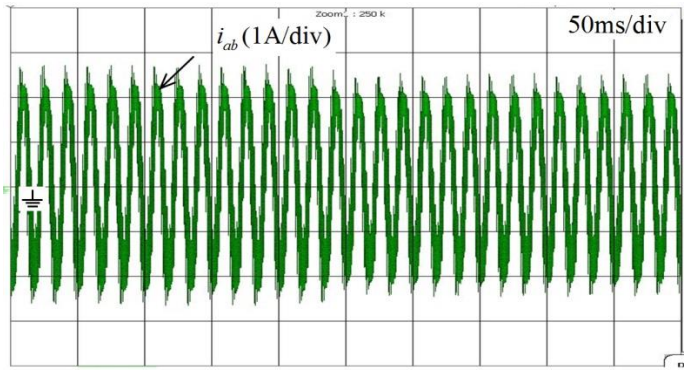

(c) Ac output current

Figure 4.11 Experimental results for a single microinverter under open-loop control with resistive load.

Table 4.2 Experimental results for open-loop control model.

	Simulation results	Experimental results	Errors (%)
$v_{dc}(D_{dc}=80.0\%)$	141 V	138 V	2.1 %
$v_{dc}(D_{dc}=79.2\%)$	134 V	132 V	1.5 %
$i_{pv}(D_{dc}=80.0\%)$	4.2 A	4.1 A	2.4 %
$i_{pv}(D_{dc}=79.2\%)$	3.8 A	3.6 A	5.3 %
$i_{ab}(D_{dc}=80.0\%)$	1.39 Arms	1.32 Arms	5.0 %
$i_{ab}(D_{dc}=79.2\%)$	1.31 Arms	1.26 Arms	3.8 %
Settling time (v_{dc})	0.07 s	0.09 s	-28.6 %
Undershoot (v_{dc})	132 V	127 V	3.8 %
Settling time (i_{pv})	0.07 s	0.09 s	-28.6 %
Undershoot (i_{pv})	1.9 A	1.8 A	5.3 %

In order to validate the fast simulation time of the proposed modeling approach in a multiple microinverter configuration, a simulation is carried out in MATLAB/Simulink with 20 parallel microinverters at 200W per PV panel for a total power output of 4kW. Figure 4.12 and Figure 4.13 show a high-level block diagram of the simulated system and the PV module model, respectively. The grid voltage is at $110V_{rms}$ and 60Hz and local loads is zero ($R_L \rightarrow \infty$) which indicates all generated power from the PV modules is sent to the grid.

Partial shading is applied to some panels in order to demonstrate the simulation flexibility. Figure 4.14(a) and 4.14(b) shows the current waveforms of the second and third microinverters among the 20 inverters where these panels have irradiance values of 900 W/m^2 and 800 W/m^2, respectively, and the irradiance of the 18 other microinverters is 1000 W/m^2. Another waveform shown in Figs. 4.14(a) and 4.14(b) is that of #1 which is at 1000 W/m^2. Figure 4.14(c) shows the total grid current from the 20 microinverters. Resulting

waveforms from using the dynamic switching model under the same conditions are shown in Figure 4.15. As expected, taking the average of waveforms generated using the dynamic model eliminates switching effects and the results match those in Figure 4.14 from the proposed average model.

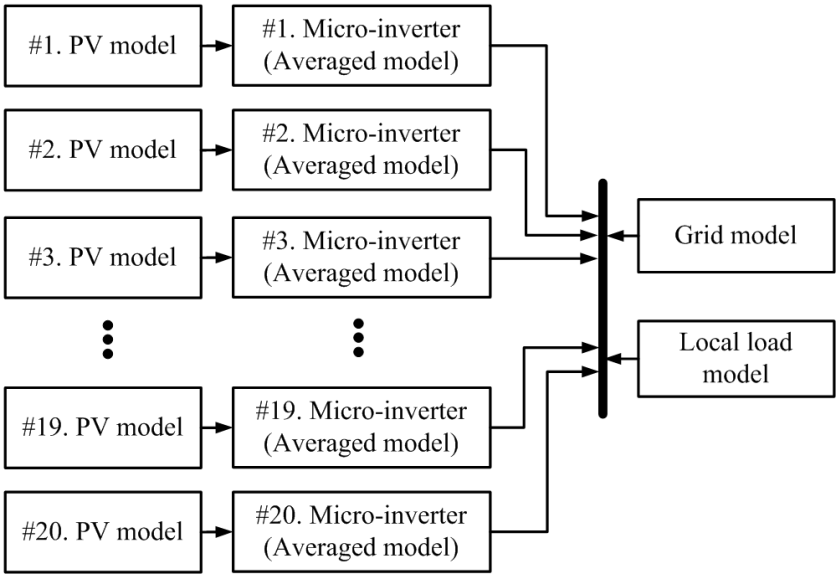

Figure 4.12 Simulation structure for aggregated microinverters.

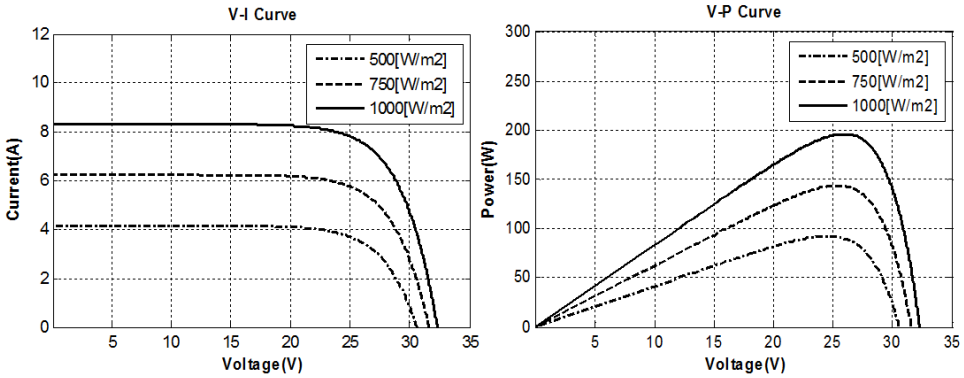

(a) V-I (b) V-P curve

Figure 4.13 Electrical characteristics of the simulated PV modules.

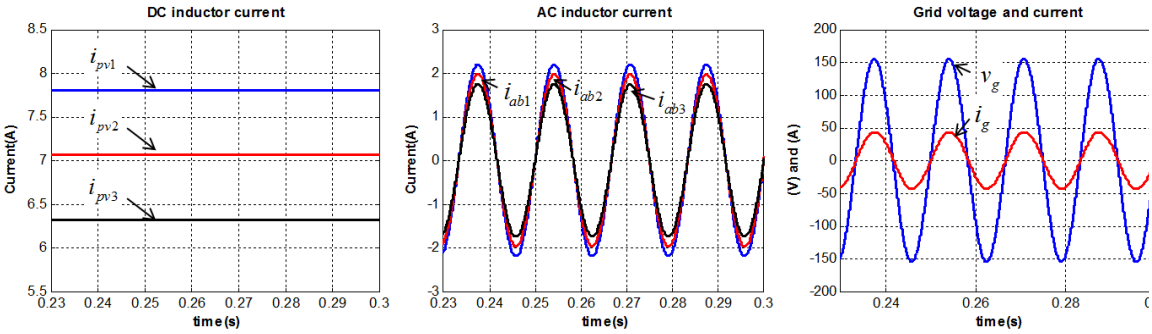

(a) (b) (c)

Figure 4.14 Simulation results using the state-space average model, (a) PV currents, (b) the output currents, and (c) grid voltage and current

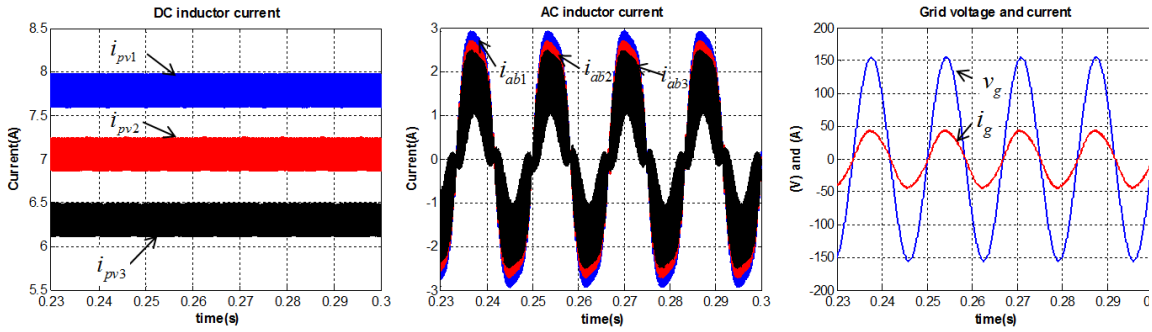

(a) (b) (c)

Figure 4.15 Simulation results using the dynamic switching model, (a) PV currents, (b) the output currents, and (c) grid voltage and current

Generally, the simulation runtime is highly dependent on the computer's performance and specifications, where the simulation tool is run, and solver options. In this paper, a computer with an Intel core i5 processor and 16 GB memory and MATLAB 2010(a) with fixed-time step and Ode4 (Runge -Kutta) are utilized as computational

medium for simulations. Simulation runtime is compared for both average and dynamic models as shown in Figure 4.16. The proposed method allows the use of a smaller step size compared to the dynamic model, thus reducing the total simulation runtime. Note that time steps $\geq$ 5.0μs resulted in erratic results in the dynamic model while the average model still performed well and all signals in the simulation model were as expected.

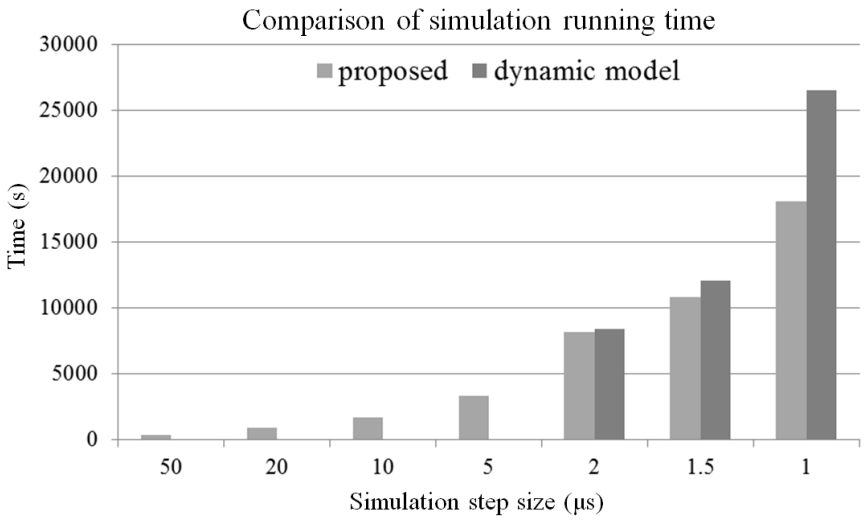

Figure 4.16 Comparison of the simulation runtime.

4.2.2 Control algorithms in PV systems

PV power is becoming more prevalent as its cost is becoming more competitive with traditional power sources and is being considered as one of the visible resources for the microgrid systems [88]. However, the utilization of dedicated energy storage systems needs to be taken into account because of the intermittent nature of the PV generation [89]. Energy storage systems can open the possibility to employ renewable energy sources able to operate in stand-alone mode, grid-connected mode, and mode transitions from stand-alone to grid, or vice versa in microgrid systems.

Figure 4.17 shows a PV system with a battery for a microgrid application, which can be connected to various distributed generation sources such as wind power, fuel cell, and diesel turbines. The PV system needs to provide secure power by delivering uninterrupted power to loads both in stand-alone operation mode and grid-connected operation mode. Using the proposed system configuration, critical loads are powered either from the grid or the PV system in grid connected mode. In addition, if critical loads cannot be supported because of accidental events and occasional failures due to grid faults, then it is necessary to change operation mode autonomously as an intentional islanding until the grid conditions return to normal [90].

There is no doubt that power converters are willing to maximize output power from renewable energy sources to increase the efficiency of conversion in both operation modes. However, there are excessive power conditions where the output power of PV modules should be adjusted with respect to the balancing power range, not relying on the MPPT algorithm. Generally, the wind turbine system has mechanical controllers such as pitch

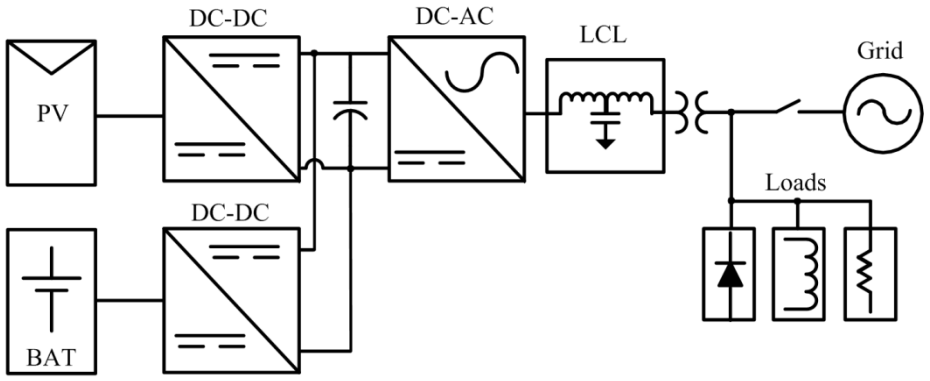

Figure 4.17 Hybrid photovoltaic-battery systems in microgrids.

controls and yaw controls as well as dynamic breakers to regulate the extra power beyond the power rating range [91], while the PV system are usually dependent on their control algorithms and protection strategies to regulate excessive power inside the system [92]. As a consequence, the control strategy preventing and limiting the surplus power from PV modules can be considered as important as MPPT algorithms, which have been published in many papers [93]-[95], in order to improve reliability of the entire PV system.

The operation modes dependent on power conditions in the stand-alone mode are shown in Table. 4.3. It should be noted that the PV converter needs non-MPPT mode at some power conditions. For instance, if generated PV power, P_{pv}(t), is much greater than critical load power, P_{loads}(t), and this surplus power cannot be consumed by battery power, P_{bat}(t), due to limited charging current or full state of charge (SOC), it results in not only, it turns out the overvoltage, but also deteriorate the entire PV system reliability. In this condition, the power flow relation shows in (4.30):

$$P_{pv}(t) > P_{load}(t) + P_{bat}(t) \tag{4.30}$$

Table 4.3 Operation modes in the stand-alone mode.

Case	***Power condition***	***Battery conv. mode***	***PV conv. mode***
I	$P_{pv} > P_{load}$	P_{bat}: Charging mode	MPPT
II	$P_{pv} > P_{load}$	Full SOC	Non-MPPT
III	$P_{pv} >> P_{load}$	P_{bat}: Max. Charging mode	Non-MPPT
IV	$P_{pv} < P_{load}$	P_{bat}: Discharging mode	MPPT

Therefore, this excessive PV power should be controllable through advanced power control algorithms, because this excessive power condition can threaten the system reliability happens frequently at drastically load change or the transition period from grid connected mode to stand-alone mode. As one of solutions for this problem, wired communication between these electrical systems has been discussed to prevent and limit excessive power [96]. Another solution is to dissipate the surplus power in the resistor banks. However, these methods may be neither practicable nor economical.

This section presents a power weakening control (PWC) to regulate photovoltaic (PV) power in excessive power conditions, when the maximum power point tracking (MPPT) algorithm is not needed. Excessive power leads to the overvoltage in the dc bus when available power from the PV arrays is greater than the sum of the load power and the battery power in the stand-alone mode. It is important to be able to control and limit this excessive PV power for protecting the PV-battery system. This section explains how to handle excessive power in the PV-battery system. The proposed PWC contains an extra dc

voltage control loop, power balance block, and hysteresis control, which decides the operation mode between MPPT and non-MPPT modes. The proposed PWC provides the load following function, thus it keeps dc voltage to be constant by controlling the surplus power. Therefore, it makes the PV-battery system more stable and robust under excessive power condition, resulting in improving the reliability of the PV-battery system. MATLAB/Simulink is used to validate effectiveness of the proposed control scheme.

a) DC-DC converters for PV-battery system

Detail power circuit diagram of DC-DC converters for the proposed PV-battery system is shown in Figure 4.18. The general boost converter is used for converting power from the PV modules and the general buck-boost converter is implemented for controlling bidirectional power of the battery. It may be desirable to be designed that the power capability of the battery is higher than one of the PV modules in order to operate the PV system at the maximum power point regardless of the maximum charging current, resulting in maximum utilization of PV power. However, it costs high for PV-battery system. Thus, in the most practical applications, the maximum charging current to the battery should be maintained within its safe limits of operation through limiting battery current along with SOC due to lower power capability of the battery.

Two control block diagrams for the dc-dc converters are shown in Figure 4.19. Cascaded voltage regulators with current regulators are used to maintain the PV bus voltage and dc link voltage within their references, while controlling maximum power point in I-V curve of PV arrays by using MPPT algorithms such as perturb & observe (P&O) method and incremental conductance method [C8], [93]-[95] and controlling the charging and

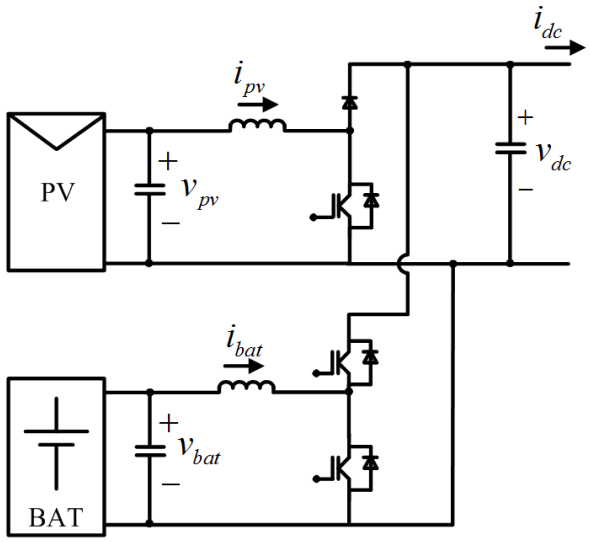

Figure 4.18 Power circuit diagram of dc-dc converters in a PV-battery system.

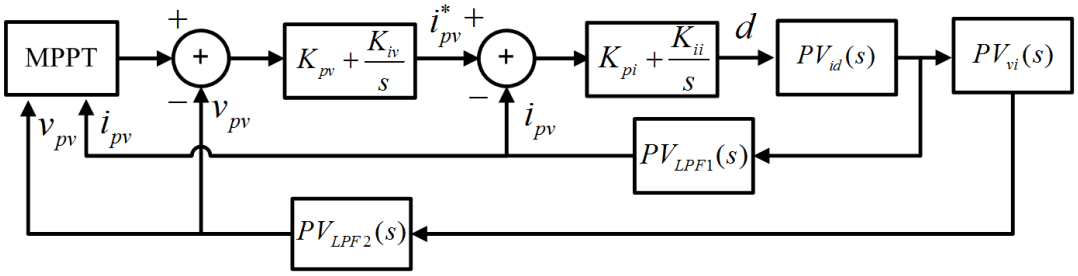

(a) Control block for PV dc-dc converter

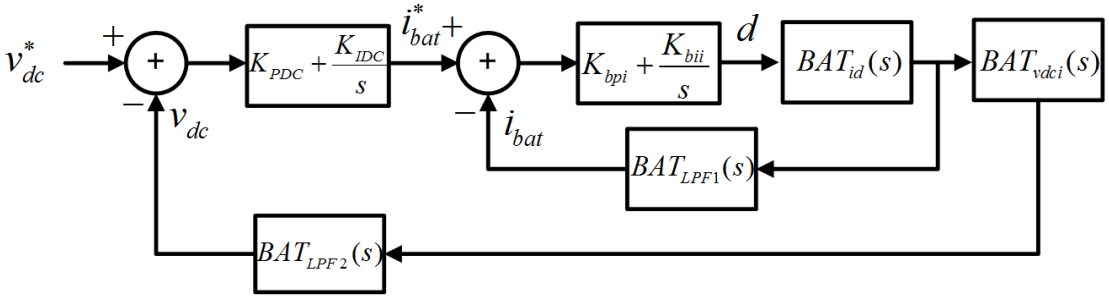

(b) Control block for battery dc-dc converter

Figure 4.19 Control block diagram of a dc-dc converter in a PV-battery system.

discharging current of the battery within the limited values. For this reason, performances of two dc-dc converters affect to the conversion efficiency and reliability of the whole PV system. Therefore, when these controllers for dc-dc converters are integrated and combined as a system, the coordination control between these converters for the PV and the battery still needs much more considerations especially for the microgrid applications, since it is a critical for the stability and safety of the system [97].

Figure 4.20 depicts the principle of the proposed PWC scheme in the I-V curve of PV modules. The PWC block does not work at the normal load condition, or the MPPT mode until surplus power occurs, because the PV current is controlled along with the trajectory of the maximum power point, $\overline{\boldsymbol{OA}}$, at different irradiance conditions through MPPT algorithms and the dc link voltage is controlled by the battery current inside the range of the maximum charging and discharging current of the battery. However, if there is

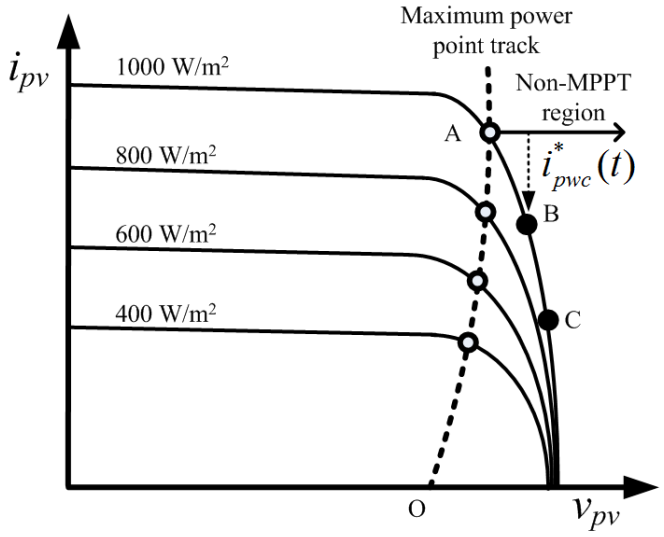

Figure 4.20 PV power weakening control.

excessive power inducing overvoltage in the dc bus, the extra dc link voltage control for PWC keeps the dc bus voltage at the higher dc voltage reference value by regulating $\boldsymbol{i_{pwc}^{*}(t)}$ autonomously, which is moving toward open circuit PV voltage at the power operation point *B* or *C*.

In the proposed PWC method, two dc voltage control loops are necessary to generate dc bus power reference, $P_{dc}^{*}(t)$, and delta PV current reference, $i_{pwc}^{*}(t)$, and also can be expressed as

$$P_{dc}^{*}(t) = K_{PDC}(v_{dc1}^{*}(t) - v_{dc}(t)) + K_{IDC}\int (v_{dc1}^{*}(t) - v_{dc}(t))dt \tag{4.31}$$

$$i_{pwc}^{*}(t) = K_{PPWC}(v_{dc2}^{*}(t) - v_{dc}(t)) + K_{IPWC}\int (v_{dc2}^{*}(t) - v_{dc}(t))dt \tag{4.32}$$

where, K_{PDC} and K_{PPWC} are proportional gains, and K_{IDC} and K_{IPWC} are integral gains for generating $P_{dc}^{*}(t)$ and $i_{pwc}^{*}(t)$, respectively. $v_{dc}(t)$ is the feedback dc voltage ,$v_{dc1}^{*}(t)$ is the dc voltage reference during the MPPT mode, and $v_{dc2}^{*}(t)$ is the upper dc voltage reference during excessive power conditions when the generated power is greater than the sum of load power and battery power.

From (4.31) and (4.32), the battery current reference, $i_{bat}^{*}(t)$, can be obtained from the power balance block in order to control dc-link voltage by balancing input power and output power, and the PV current reference, $i_{pv}^{*}(t)$, can be obtained from the output of the MPPT and PWC blocks.

$$i_{bat}^{*}(t) = \frac{P_{dc}^{*}(t) - P_{pv}^{*}(t)}{v_{bat}(t)} \tag{4.33}$$

$$\boldsymbol{i_{pv}^{*}(t) = i_{mppt}^{*}(t) - i_{pwc}^{*}(t)} \tag{4.34}$$

where, $P_{pv}^{*}(t) = i_{pv}^{*}(t) \cdot v_{pv}(t)$

In addition, the selection of controllers can be carried out by a hysteresis controller based on the feedback dc link voltage value. Thus, the selecting signal for the dc voltage controller can be obtained as

$$s_h(t) = \begin{cases} 0, & \text{if } v_{dc}(t) < v_{dc1}^{*} \\ 1, & \text{if } v_{dc}(t) > v_{dc2}^{*} \end{cases} \tag{4.35}$$

This hysteresis controller can easily switch from MPPT to non-MPPT mode or vice versa. Figure 4.21 shows the proposed overall control structure diagram of the PV-battery system including the power balance and the PWC.

The MATLAB/Simulink model was built to validate the proposed system in the stand-alone mode with the power conditions shown in Table 4.4. The PV converter controls the PV voltage in order to extract maximum power from the PV arrays through P&O MPPT algorithm. The battery, which is controlled by another dc-dc converter with the bidirectional power flow, can be used to balance the input power and output power.

Figure 4.22 shows the simulation results without the PWC at excessive power conditions. At 0.3s, the load power is changed from 2.8kW to 1.3kW and the battery charging current increases to its maximum charging current level, while the PV converter is operating at the MPPT. Still, there is excessive power need to be consumed and there is no way to absorb this excessive power, which makes an overvoltage in the dc bus, because the PV system is still producing power at the maximum power. The DC overvoltage problem happens again when the SOC of the battery is full. Therefore, an additional control algorithm needs to be considered for non-MPPT mode operation.

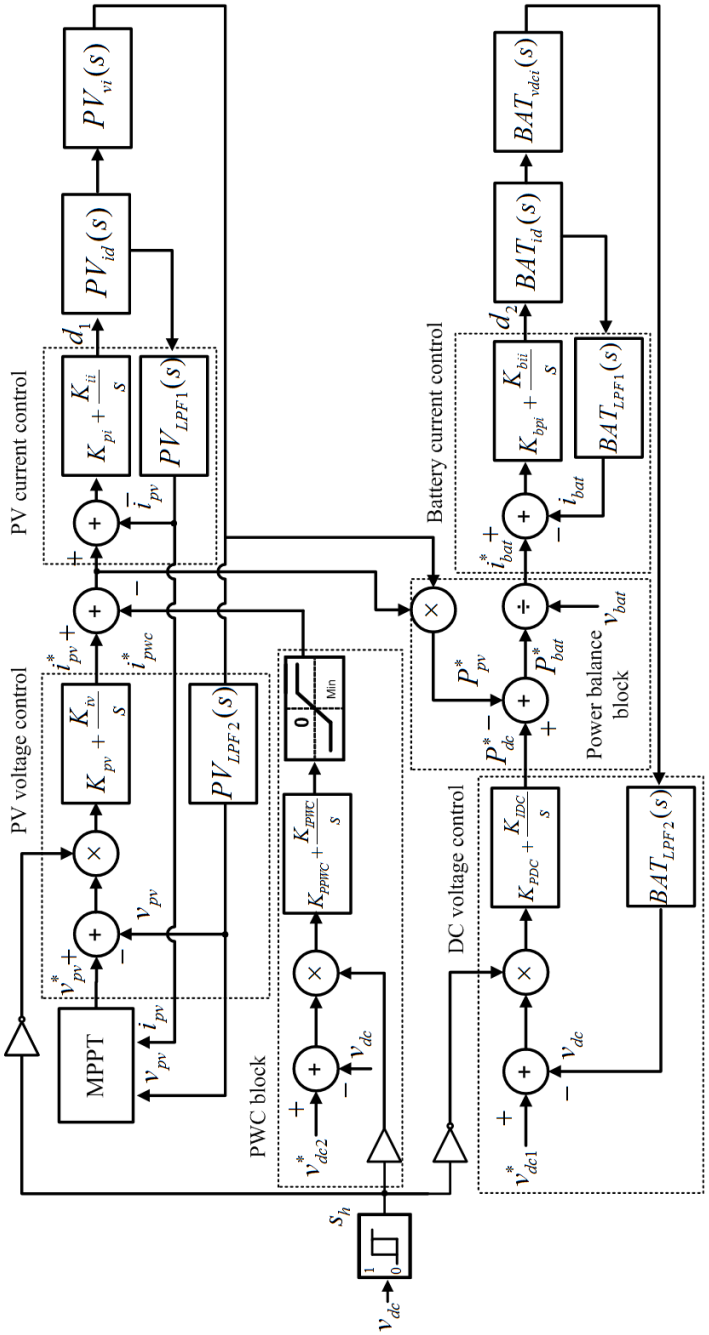

Figure 4.21 Proposed control block for the PV-battery system.

Table 4.4 Power scenarios for simulation.

Source	***Conditions***
PV	4kW @ T= 25C° and G= 1000 W/m^2 MPPT algorithm : P&O method
Battery	Max. charging and discharging power :2.1kW Initial SOC : 85% Maximum SOC: 90%
Load	2.8kW : 0s < t < 0.3s 1.3kW: 0.3s < t < 0.8s 2.8kW: 0.8s < t < 2s
DC voltage command	v_{dc1}^*: 200V @ normal condition v_{dc2}^*: 230V @ power weakening control

Figure 4.23 and Figure 4.24 show the simulation results of the proposed PWC regulating PV power autonomously based on the dc bus voltage at the previous load scenarios. At 0.3s, the dc voltage increases due to the change of load causing excessive power, and then PWC starts to maintain constant dc bus voltage operating at a higher dc voltage set point (230V) shown in Figure4.23. $i_{pwc}^*(t)$ from the PWC block increases to reduce PV power and then the PV current reference value goes to the proper value in order to remove excessive power. In the proposed control method, there is no component to calculate the amount of surplus power to be removed and it is using only the dc bus voltage information to determine non-MPPT mode, which makes simple and easy implementation with the existing controller. At 0.8s, load power increases to 2.8kW and the PV system returns to MPPT mode to generate the maximum power from the PV modules at the given

temperature and irradiation and to provide power to the loads. It can be noted that as soon as the load is changed, a mismatch between the PV power generation and the load demand is created and the battery compensates the mismatch instantaneously. As a consequence, these simulation results show that the proposed PWC method keeps the power balance very well in excessive power conditions.

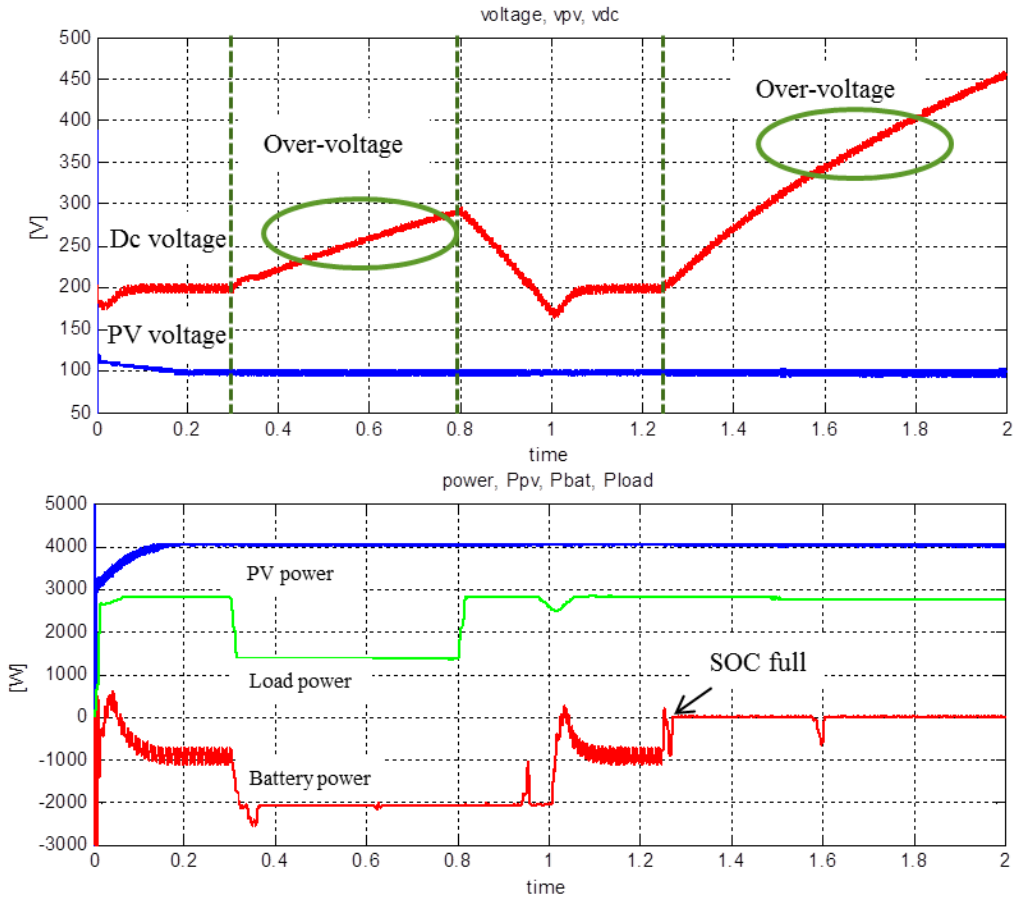

Figure 4.22 Simulation results without power weakening control.

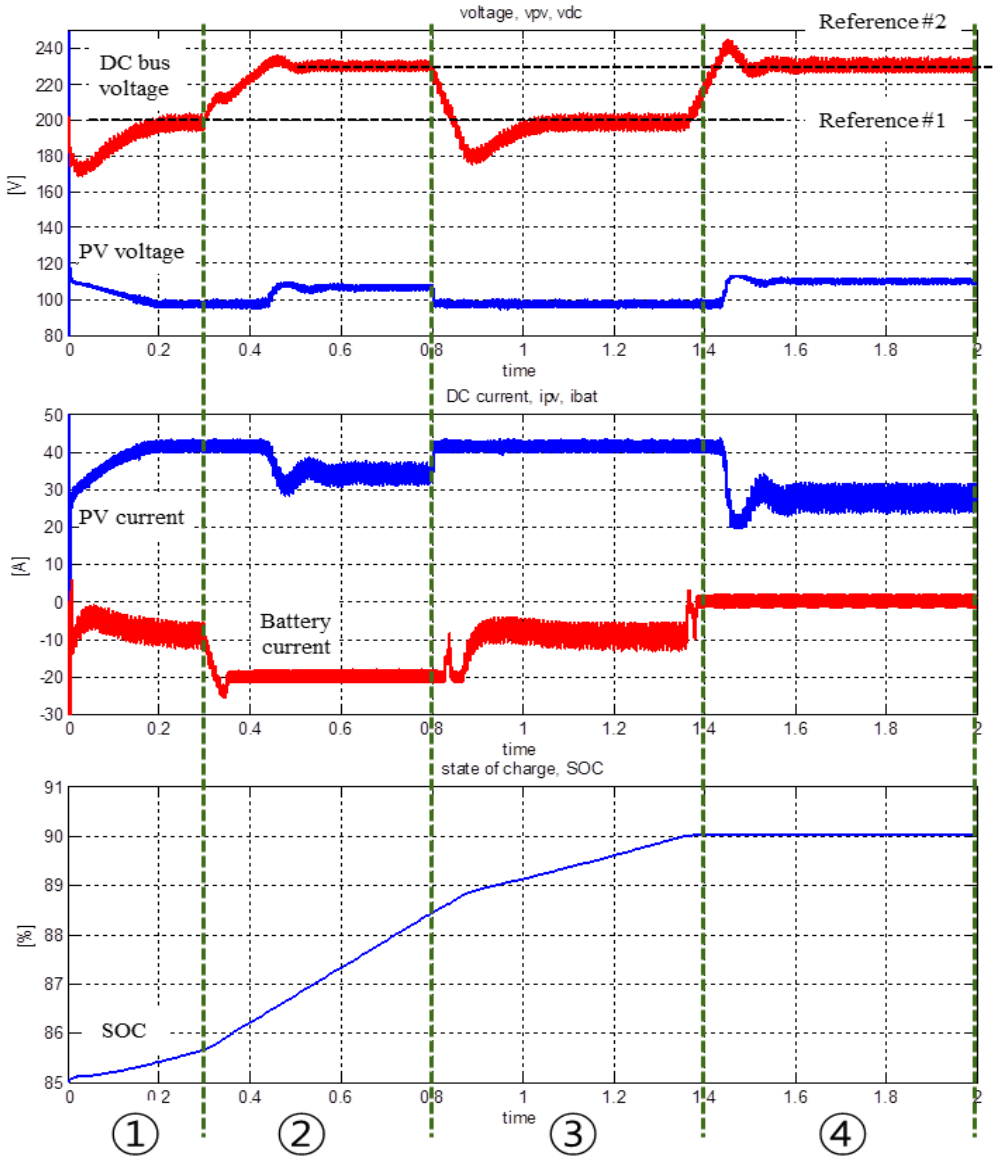

① : Starting MPPT (PV < Bat +Load)
② : Decreasing Load power →Limiting battery maximum current (PV > Bat +Load)
- Enable Power weakening control
③ : Normal condition (PV < Bat +Load)
④ : Maximum SOC (90%) (Bat=0)
- Enable Power weakening control

Figure 4.23 Simulation results with power weakening control operation-1.

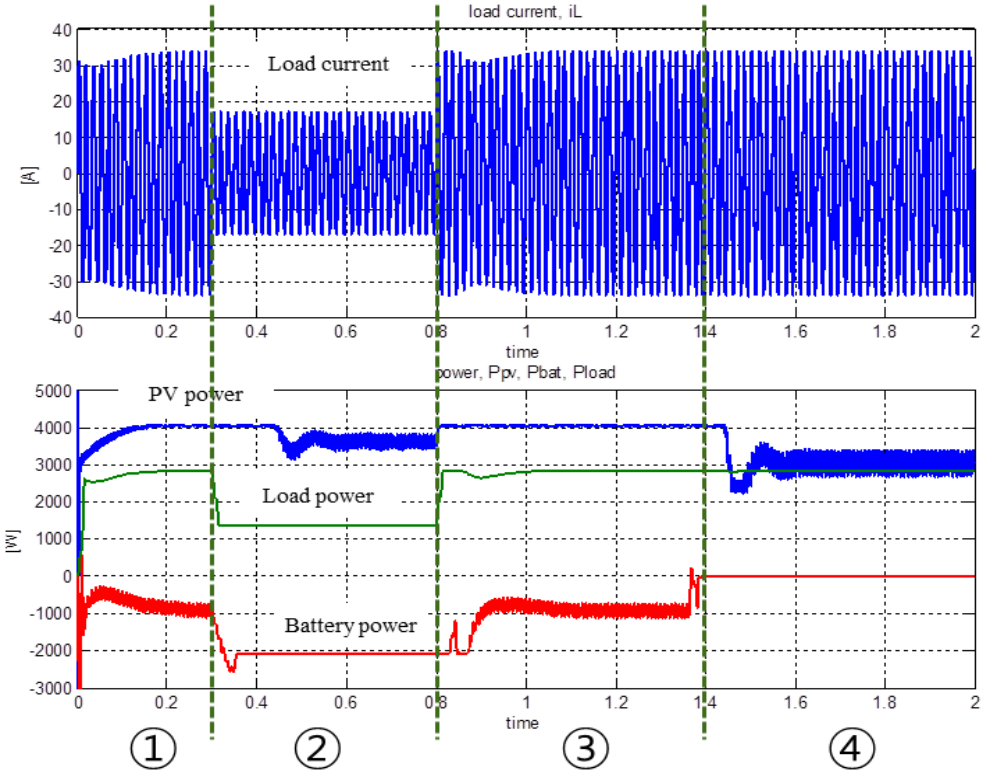

Figure 4.24 Simulation results with power weakening control operation-2

In this section, some conditions in the PV-battery system, which are not in favor of the MPPT operation, was pointed out. Unless unintended surplus power from PV modules is regulated and limited in these conditions, this induces the over-voltage in the dc bus, resulting in tripping the PV-battery system. The power weakening control (PWC) for the PV-battery system is proposed to regulate or weaken PV power as moving operation point from the maximum power point to the open circuit voltage in the PV curve, where excessive PV power can be controlled to meet power demand of the system consisting of

load power and battery power without overvoltage trip. The proposed PWC contains an extra dc voltage control loop, which is switched automatically by a hysteresis controller in excessive power conditions to guarantee stable operation by eliminating unintended surplus power. The performance of the PV-battery system using PWC at excessive power conditions was validated by MATLAB/Simulink simulations.

4.3 V2G applications

The concept of vehicle-to-grid (V2G) integration has recently emerged to incorporate electric vehicles into the power system as energy storage units [14]-[17]. In such applications, electric vehicles can be used to store excess energy from the grid when demand for power is low, and provide power back to the grid when demand for power is high. This results in enhanced reliability and performance of the power system by using a bidirectional power transfer topology instead of a unidirectional power transfer topology used conventionally.

Many papers have reviewed converter topologies and their characteristics for V2G applications being able to control bidirectional power flow [98], but only few papers have shortly introduced cycloconverter-type high frequency link (CHFL) converter in spite of some papers have asserted that CHFL converters have high potentials as future renewable energy converters [99], [100]. Typically bidirectional battery chargers for V2G applications have required high power density to reduce volume and weight, high efficiency and long life cycle. When these requirements are considered, CHFL converters can be attractive candidates because these reduce a power conversion stage by applying ac-ac conversion capability and it allow of removing high volume dc energy storages, thus resulting in high power density, high efficiency and long life cycle. Moreover, by engrafting the phase-shift PWM converter into the cycloconverter converter, the ac current ripple can be two times of the switching frequency, which reduces the size of ac output filter.

In this section, a power control method of the CHFL converter is proposed for V2G applications to secure active and reactive power control as well as to satisfy the power

quality requirements such as IEEE, SAE, IEC standards for interconnecting bidirectional battery chargers with power systems.

4.3.1 Cycloconverter-type high frequency link converter

The proposed battery charger using the CHFL converter for V2G is shown in Figure 4.25 and mainly consisted of three converters; 1) a synchronous converter keeps the dc-voltage constant from a variable battery voltage for supplying dc power to the dc-ac high frequency converter, 2) a dc-ac converter generates a high frequency bipolar ac-signal for ac-ac cycloconverter, and 3) an ac-ac cycloconverter switches are commutated primarily at line frequency when the polarities of output current and output voltage are the same and at high frequency when the polarities are opposite. This architecture supports bidirectional power flow capable of the four-quadrant operation shown in Figure 4.26 and Table 4.5 and reduces system complexity by removing the rectifier and the dc-link filter, resulting in the high efficiency and high power density. Also, galvanic isolation is achieved by embedding the transformer into the overall converter.

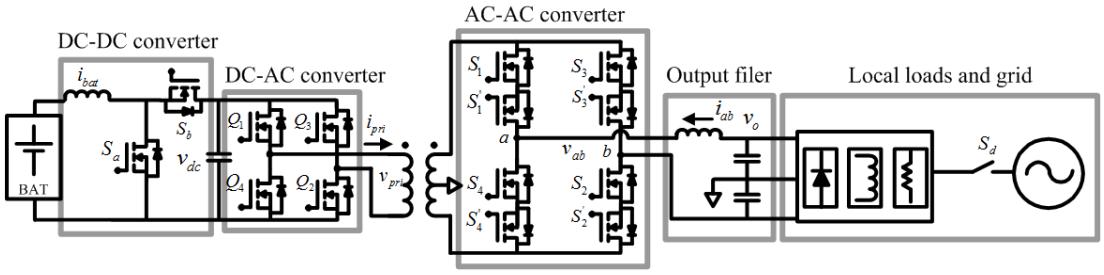

Figure 4.25 Cycloconverter-type high-frequency link converter for V2G.

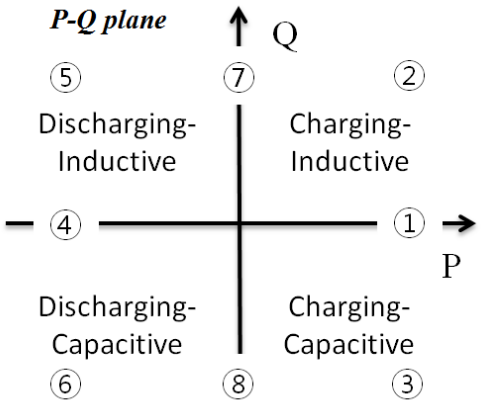

Figure 4.26 Four-quadrant operation of a bidirectional converter.

Table 4.5 Four-quadrant operation mode.

No.	Active (P)	Reactive (Q)	Operation mode
1	Positive	Zero	Charging
2	Positive	Positive	Charging-Inductive
3	Positive	Negative	Charging-Capacitive
4	Negative	Zero	Discharging
5	Negative	Positive	Discharging-Inductive
6	Negative	Negative	Discharging-Capacitive
7	Zero	Positive	Inductive
8	Zero	Negative	Capacitive

Figure 4.27 and Figure 4.28 show the switch signals and some key waveforms [99], [100]. Referring the analysis on the switching action and the voltage/current waveforms in previous slides, the principle of the CHFL operation can be induced as follows; 1) the phase-shifted PWM converter (ac-dc converter) generates the pulsating ac voltage

according to the dc-bus voltage, 2) this pulsating voltage are rectified by the cycloconverter (ac-ac converter). The rectified voltage can be negative or positive depending on the operation mode, 3) Thus, the dc pulsating output voltage of the cycloconverter is switched with on/off sequence, and 4) This pulsating output voltage can decrease or increase the output current according to the grid voltage, the duty ratio and inductance values (ac side inductance and series transformer leakage inductance). It should be noted that the frequency of the output current ripple is twice of the switching frequency. That is a major benefit of the CHFL converter topology, which can reduce amount of the current ripple compared to general ac-dc converters with the same inductance value.

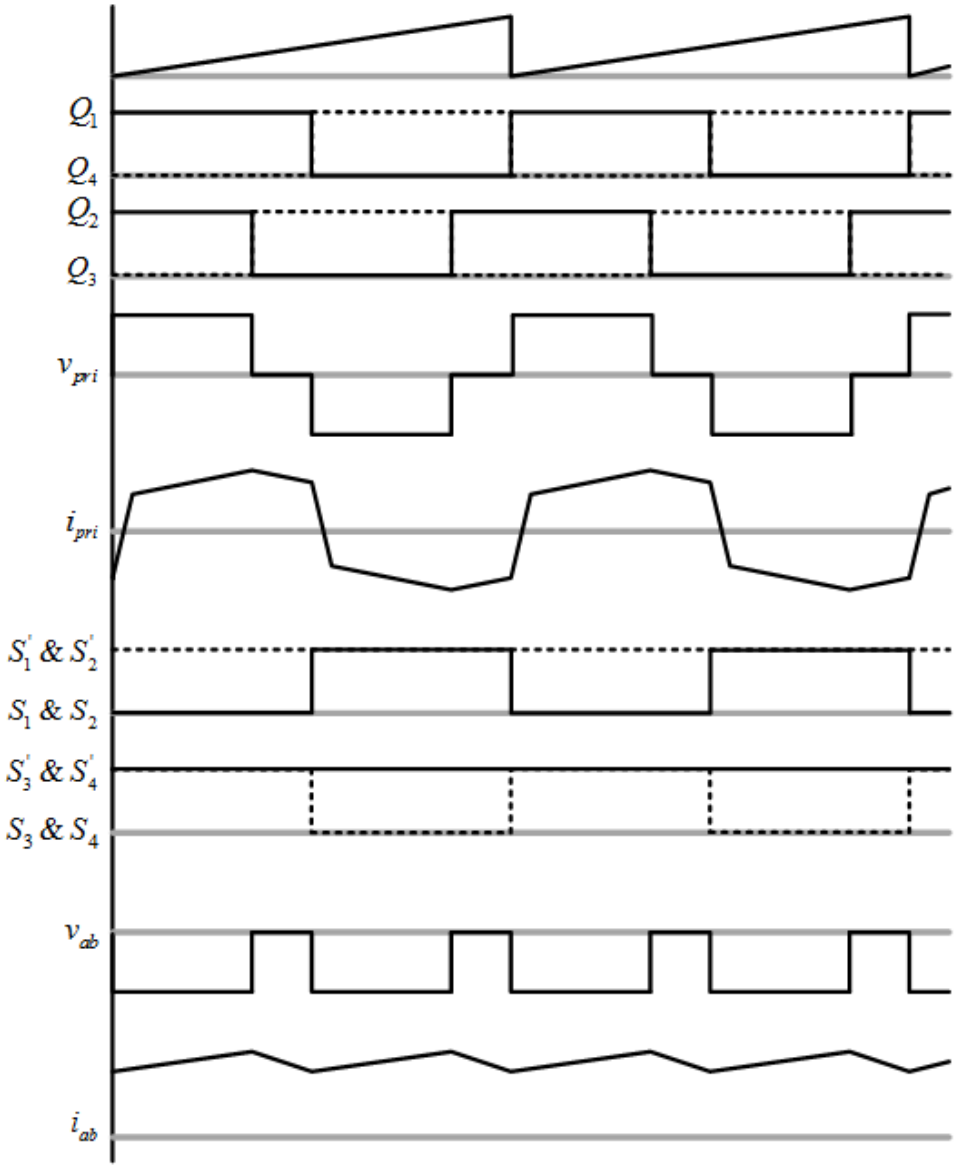

Figure 4.27 Key waveforms of the CHFL converters in exporting power mode (Positive current)

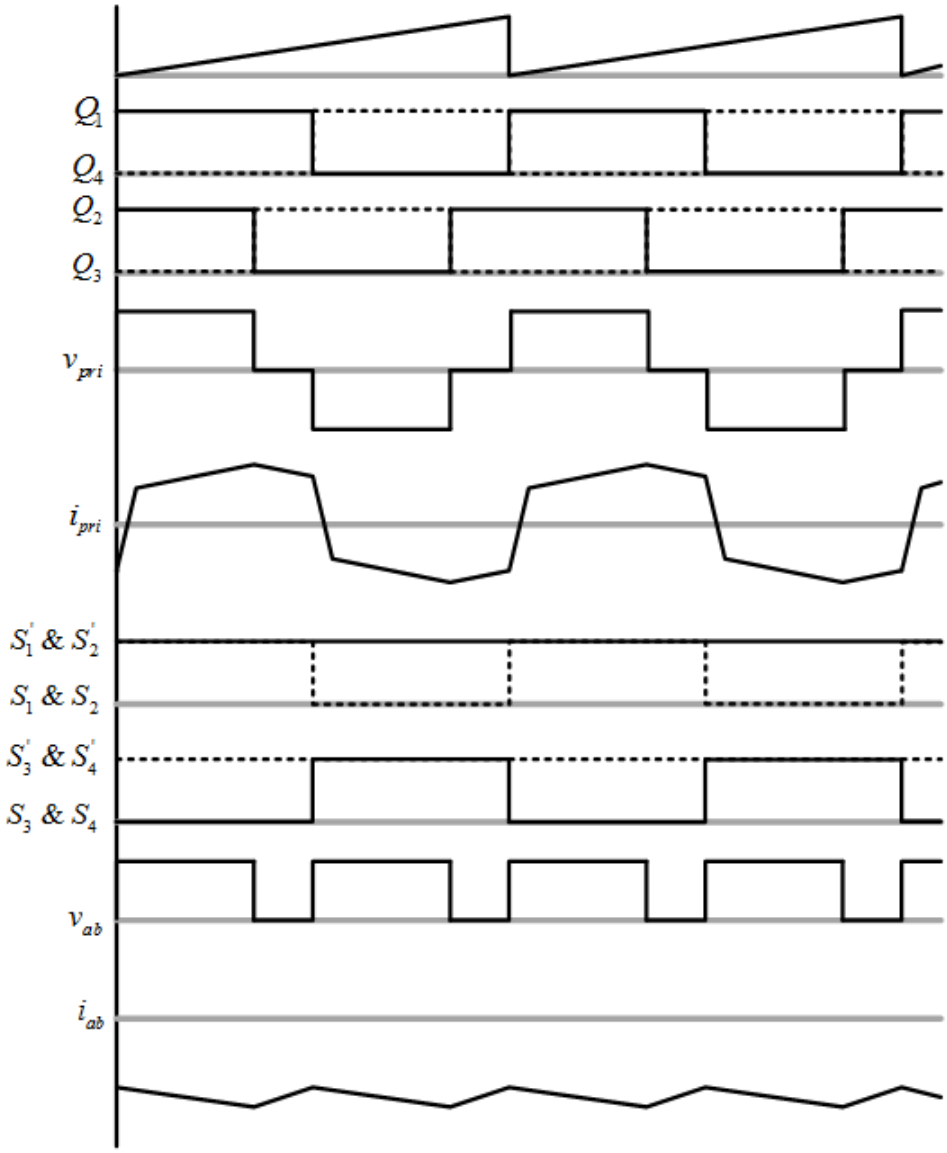

Figure 4.28 Key waveforms of the CHFL converters in exporting power mode (Negative current)

4.3.2 Control algorithms in V2G systems

Regardless of power circuit topologies, power control methods for active and reactive (P-Q) power commands at the grid-tied converter are necessary to yield output duty references. As a result, these output duty references are propagated to the pulse-width-modulation (PWM) generator, which will convert this information to PWM signals suited for specific converter topologies. This process is meant to control the output voltage of power devices in ac-dc power stages and then ultimately force the output current waveform to satisfy the power reference. Many control methods for active and reactive power generation have been well documented in literature [15], [98], [101], [102].

Figure 4.29 shows a classfication of PQ power control methods. In method A-1, the converter directly control both the magnitude (V_c)and phase (δ) of its outpu voltage by P-Q control loop where active and reactive power correspond to the following equations below,

$$P = \frac{V_s V_c}{X} \sin(\delta) \tag{4.36}$$

$$Q = \frac{V_s^2}{X}\left(1 - \frac{V_c}{V_s}\cos\delta\right) \tag{4.37}$$

This method is more suitable for a droop control at converter parallel operation. In method A-2, active and reactive power are controlled by converter currents expressed as,

$$P = V_s I_c \cos\theta \tag{4.38}$$

$$Q = V_s I_c \sin\theta \tag{4.39}$$

Where I_c and θ are a converter current magnitude and phase difference between a converter

voltage and current, respectively. This method is more general and popular method for grid-tied converters. The converter output current can be controlled on ac stationary frame (method B-1) or *αβ-dq* synchronous rotating frame (method B-2) and their overall control structures are shown in Figure 4.30. In single-phase power systems, the *β* component is not externally available and the virtual axis made by synthesizing a 90 degree phase-shift operation at the fundamental frequency need to be used. It will make the system more complex to implement, but PQ power can be controlled independently by d and q axis currents. Also designing the current controller is easier than method B-1 and the performance of the current tracking to references is improved. In method C, the current reference can be generated by open-loop (method C-1) or closed-loop (method C-2) methods as shown in Figure 4.31. The closed-loop method is more robust to disturbances, but requires accurate power calculation and compensators.

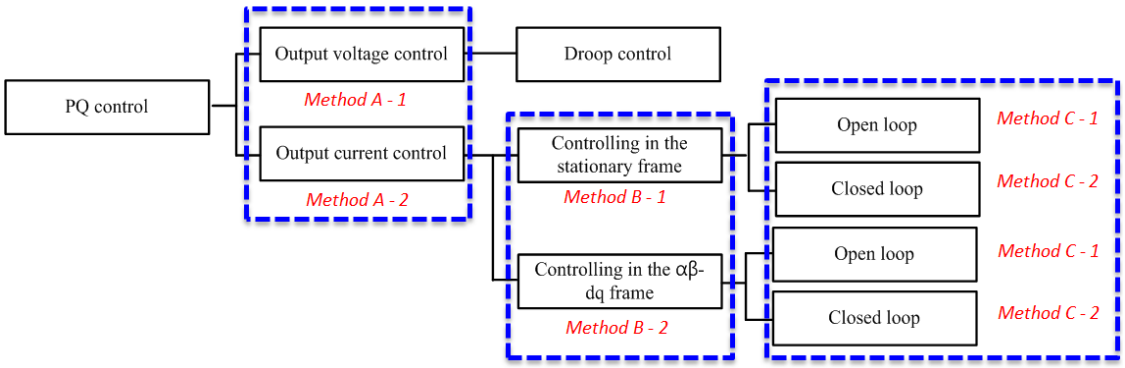

Figure 4.29 PQ control method classification for a bidirectional converter.

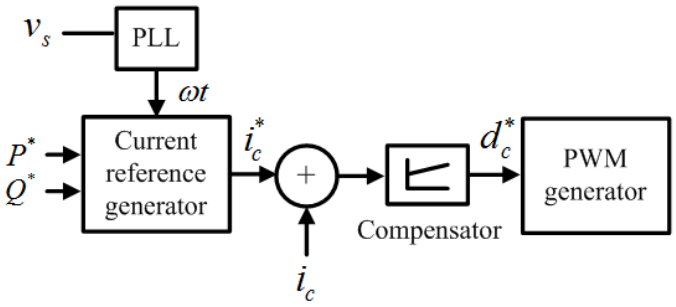

(a) Control method on the ac stationary frame

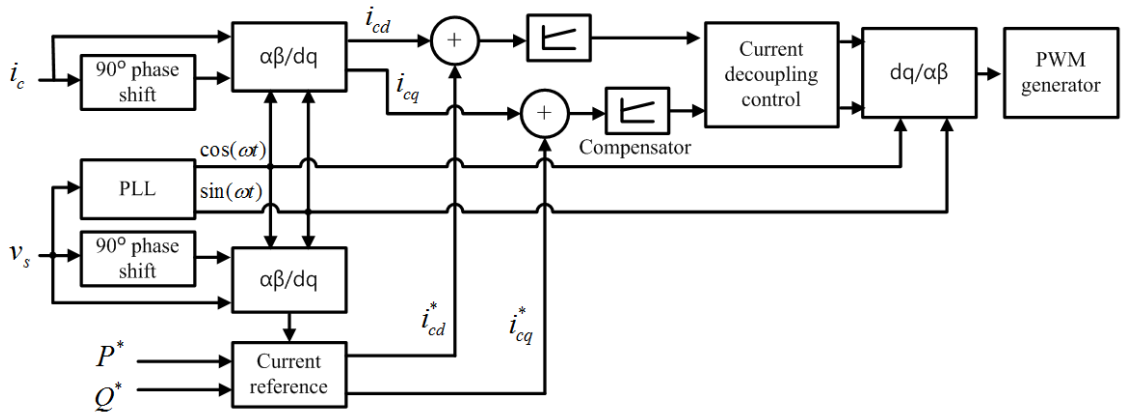

(b) Control method on the dq frame

Figure 4.30 Control methods according to the control frame (Method B)

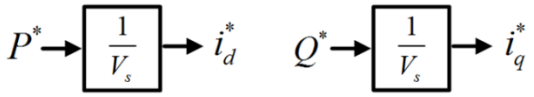

(a) Open-loop method

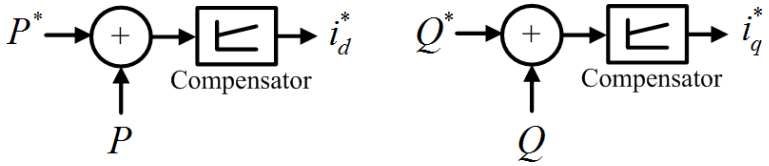

(b) Closed-loop method

Figure 4.31 Current magnitude reference generators (Method C)

Most conventional methods generate current references by utilizing a phase-based equation that commonly includes the grid, anti-islanding, and reactive power phase information, which are determined by phase-locked- loop (PLL) algorithms [103]-[105], anti-islanding algorithms [106]-[111], and active and reactive power references, respectively, resulting in increased computational burden. Whereas, the proposed method yields the trigonometric-based current references using the sine and cosine terms of the grid phase from existing PLL algorithms. Then the amplitudes of these sine and cosine terms are caluculated not only for active power control but also reactive power and anti-islanding algorithms, resulting in a reduced number of calculation steps and producing a simpler current reference generator. These advantages allow the use of fixed point digital signal processors rather than high cost, high performance digital signal processors in single phase bi-directional converter applications.

Figure 4.32 shows the proposed power control method of the CHFL converter mainly consisting of reference generator, current control, and PWM generator for grid-connected operation. Reference generator yields the current references by using a grid phase, power calculation, and anti-islanding algorithm. The current controller includes the general feedback proportional-integral (PI) control and feedforward controller. Finally, the PWM signals are fed to the individual phase-shifted PWM converter and cycloconverter.

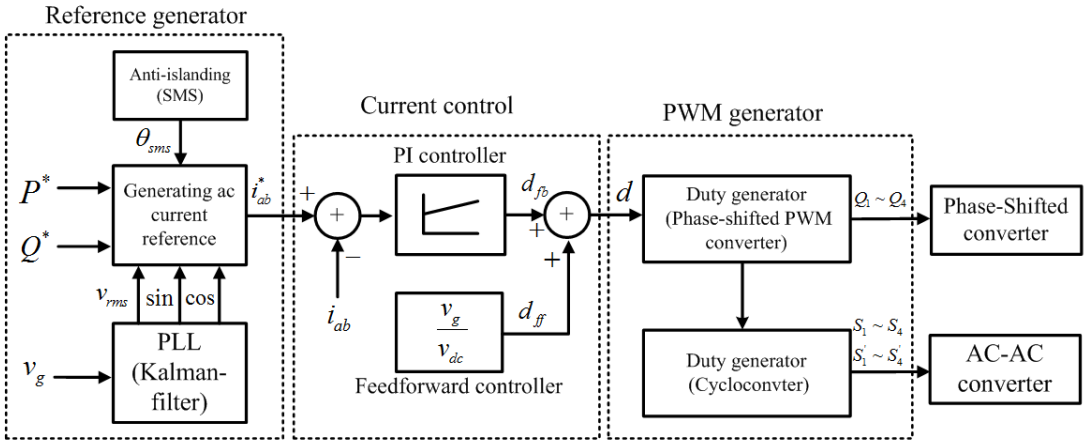

Figure 4.32 Proposed power control method of the CHFL converter.

a) Feedback and Feedforward current controller

To make sure the performance of the current controller theoretically, the current controller for the CHFL converter is designed using MATLAB. The CHFL converter in exporting power mode can be represented with the buck-converter model shown in Figure 4.33. Using the buck converter model in MATLAB, the plant transfer function, which is

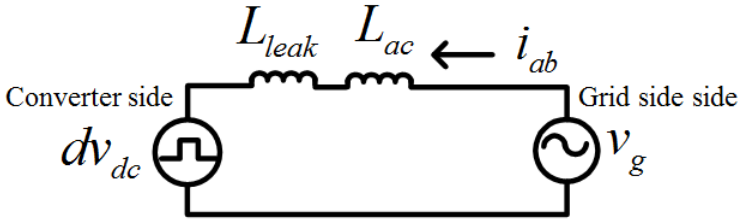

Figure 4.33 Simplified model of the CHFL converter.

duty to the output current, can be derived. Using SISO Tool in MATLAB, the PI current controller can be designed with the given plant model. After obtaining the PI current controller for the continuous time domain, this controller can be converted to discrete time domain for implementing a digital controller.

The feedforward controller improves the performance of the current controller by compensating the undesired input admittances. The relationship between converter voltage, v_{dc} and grid voltage, v_g, can be represented with respect duty cycle, d, as

$$v_g = (L_{leak} + L_{ac})\frac{di_{ab}}{dt} + dv_{dc} \tag{4.40}$$

$$d = \underbrace{-\frac{1}{v_{dc}}(L_{leak} + L_{ac})\frac{di_{ab}}{dt}}_{Feedback} + \underbrace{\frac{v_g}{v_{dc}}}_{Feedforward} \tag{4.41}$$

As investigated in Chapter 2, the current tracking performance can be improved by adding the feedforward duty to the feedback duty generated by the general PI current controller.

b) Current reference generator for anti-islanding algorithms

An islanding condition occurs when a part of a distributed utility system becomes isolated from the rest of the system and continues to operate to supply power to a location. For example, an islanding condition may occur if the energy from the power grid is interrupted, but the grid-connected converter continues to energize a load on the grid. When an islanding condition occurs unintentionally, continuing to power a load on the grid from the distributed source may create a hazard for utility workers or for the public by causing a line to remain energized when the line is assumed to have been disconnected from all energy sources. Furthermore, when an island is formed and isolated, the utility

may have no control over the current, voltage, and/or frequency in the island, creating the possibility of damaging electrical equipment in the island. As such, anti-islanding algorithms need be used in the bidirectional power converter to detect the occurrence of unintentional islanding and take the appropriate action (e.g., discontinue exporting power). There are many anti-islanding algorithms in recent literatures. Passive techniques are using information of the grid voltage or current or frequency and monitoring whether the voltage and frequency are under or over to normal conditions, whereas active techniques are introducing positive disturbances which leads to trigger under/over voltage and under/over frequency protection when the converter is in islanding operation, resulting in reducing non-detection zone.

Among active methods, a slip-mode frequency shift methods (SMS) [110],[111] is selected to utilize the proposed reference generator without generating current harmonics. In the SMS anti-islanding algorithm, the phase angle of the output current is controlled with respect to the frequency of the PCC voltage. For example, if the frequency of the PCC voltage is slightly increased after the grid disconnection, the phase angle of the current is increased, which reduces the time to the next zero crossing of the PCC voltage. This is interpreted by the controller as a frequency increase, so the phase angle of the current is increased again, and so on, until the over-frequency protection is triggered. Similarly, when the frequency of the PCC voltage decreases after the grid disconnection, the frequency is continuously decreased until the under-frequency protection is triggered.

The current reference for controlling instantaneous output current can be generated by active and reactive power references like method A-2. Since the output from the PLL

yields sine and cosine value of the grid voltage instead of phase angle, θ, itself, the current reference can be represented by the combination of sine and cosine terms. The sine coefficient and cosine coefficient can be derived as follows. Conventionally, current references with ac signal forms can be described with the magnitude and phase values and written as,

$$i_{ab}^{*} = I_{ref\_mag} \sin(\theta_{pll} - \theta_{reactive} + \theta_{sms}) \tag{4.42}$$

where,

$$I_{ref\_mag} = \frac{\sqrt{2} \cdot \sqrt{P_{ref}^2 + Q_{ref}^2}}{V_{grms}},\ \theta_{reactive} = \cos^{-1}\left(\frac{P_{ref}}{S_{ref}}\right),\ \theta_{sms} = \frac{2\pi}{360}\theta_m \sin\left(\frac{\pi}{2}\frac{f - f_g}{f_m - f_g}\right)$$

In (4.42), $\theta_m$is the maximum phase shift, f_m is the frequency at the maximum phase shift, and f is the output frequency of the power converter. Modified current reference form with the combination of sine and cosine components can be expressed as,

$$i_{ab}^{*} = k_1 \sin\omega t + k_2 \cos\omega t \tag{4.43}$$

To obtain the k_1 and k_2, the sine term of (4.42) can be re-written as,

$$\begin{aligned} &\sin(\theta_{pll} - \theta_{reactive} + \theta_{sms}) \\ &= \left(\sin\theta_{pll}\cos\theta_{reactive} - \cos\theta_{pll}\sin\theta_{reactive}\right)\cos\theta_{sms} \\ &\quad + \left(\cos\theta_{pll}\cos\theta_{reactive} + \sin\theta_{pll}\sin\theta_{reactive}\right)\sin\theta_{sms} \end{aligned} \tag{4.44}$$

Using (4.42) and (4.44), the current reference can be obtained and the k_1 and k_2 can be expressed as,

$$i_{ab}^{*} = \frac{\sqrt{2} \cdot S_{ref}}{V_{grms}} \begin{pmatrix} \left(\frac{P_{ref} \cos\theta_{sms} + Q_{ref} \sin\theta_{sms}}{S_{ref}} \right) \sin\theta_{pll} \\ -\left(\frac{Q_{ref} \cos\theta_{sms} - P_{ref} \sin\theta_{sms}}{S_{ref}} \right) \cos\theta_{pll} \end{pmatrix} \tag{4.45}$$

$$k_1 = \frac{\sqrt{2}}{V_{grms}} \left(P_{ref} \cos\theta_{sms} + Q_{ref} \sin\theta_{sms} \right) \tag{4.46}$$

$$k_2 = -\frac{\sqrt{2}}{V_{grms}} \left(Q_{ref} \cos\theta_{sms} - P_{ref} \sin\theta_{sms} \right) \tag{4.47}$$

Furthermore, since θ_{sms} is small, cos θ_{sms} and sin θ_{sms} approach 1 and θ_{sms}, respectively. Therefore, equations (4.46) and (4.47) for k_1 and k_2 can be more simplified.

$$k_1 = \left(\frac{\sqrt{2}}{V_{grms}} \right) \left(P_{ref} + Q_{ref} \theta_{sms} \right) \tag{4.48}$$

$$k_2 = -\left(\frac{\sqrt{2}}{V_{grms}} \right) \left(Q_{ref} - P_{ref} \theta_{sms} \right) \tag{4.49}$$

Finally, using (4.43), (4.48) and (4.49) the current reference can be expressed as,

$$i_{ab}^{*} = \left(\frac{\sqrt{2}}{V_{grms}} \right) \left(\left(P_{ref} + Q_{ref} \theta_{sms} \right) \sin\omega t - \left(Q_{ref} - P_{ref} \theta_{sms} \right) \cos\omega t \right) \tag{4.50}$$

If power references are commanded as P_{ref}=1.6-kW and Q_{ref}=0.3-kVar, actual power references are rely on the current grid frequency as shown in Figure 4.34. Thus, these reference changes accelerate the PCC frequency to be deviated from the nominal frequency (60Hz), resulting in triggering over/under frequency protections.

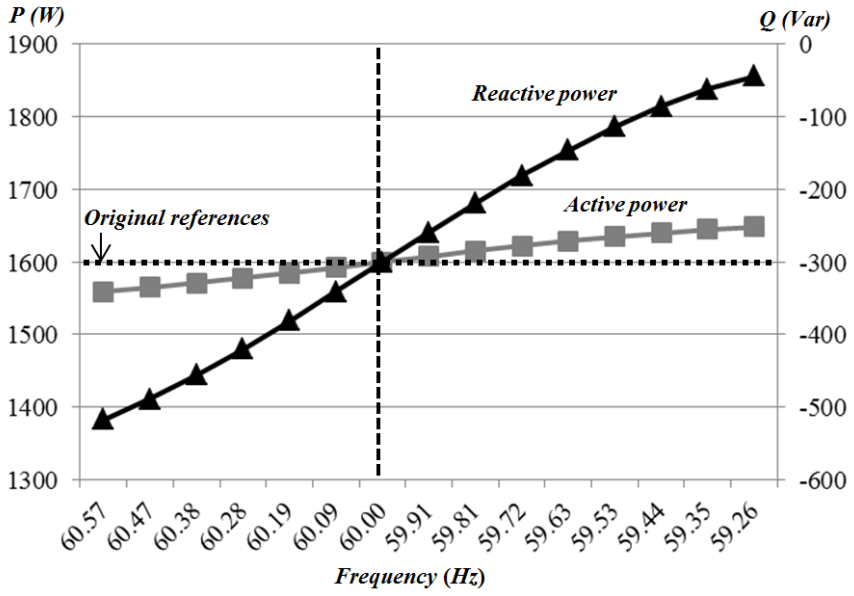

Figure 4.34 Power references variations according to grid frequency.

Figure 4.35 shows the experimental test bench for validating the effectiveness of the proposed control method. A 1.7 kW single-phase CHFL converter is used. The passive and electronic loads used are connected with the grid and converter at the PCC.

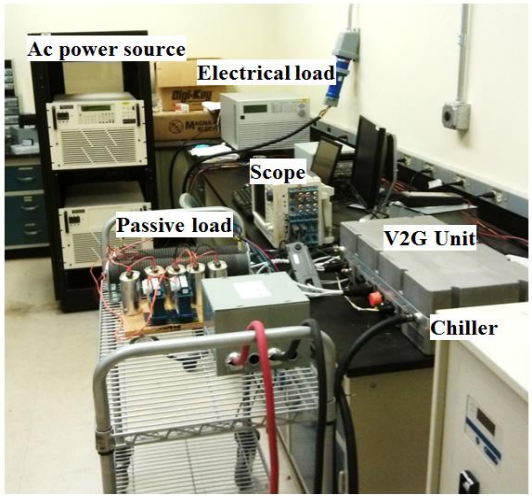

Figure 4.35 Test bench set-up for CHFL.

Figure 4.36 shows experimental results for grid-connected operation with four active power commands: 0W, 500W, 1000W, and 1600W. In Figure 4.36(a), the converter current is circulated and most of current flow from grid to load. In Figure 4.36(b) and 4.36(c), the active power from the converter is increased as power command increased. The amount of grid current is reduced and most of current for the load was provided from the V2G converter shown in Figure 4.36.

Figure 4.37 shows experimental results of anti-islanding algorithms, (a) with the passive method when $\Delta P >> 0$ and $\Delta Q >> 0$, (b) with the passive method $\Delta P \approx 0$ and $\Delta Q \approx 0$, and (c) with SMS method $\Delta P \approx 0$ and $\Delta Q \approx 0$. If the variations of active and reactive powers are large, the passive anti-islanding method provides correct response with respect to the grid condition. However, if the variations of active and reactive powers are small, the response of the passive anti-islanding method may not response. It can be observed in Figure 4.37 that the islanding operation could be detected by the active anti-islanding algorithms under the same condition where the passive method could not detect it. Since the SMS method injected power disturbances depending on the PCC frequency, the PCC frequency could be more deviated from the nominal frequency (60Hz), and it triggered the over-frequency protection.

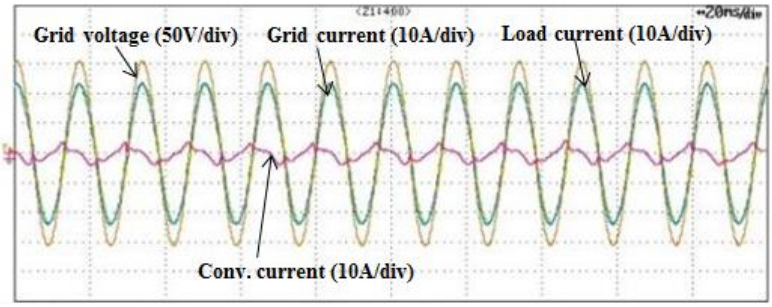

(a) P =0W

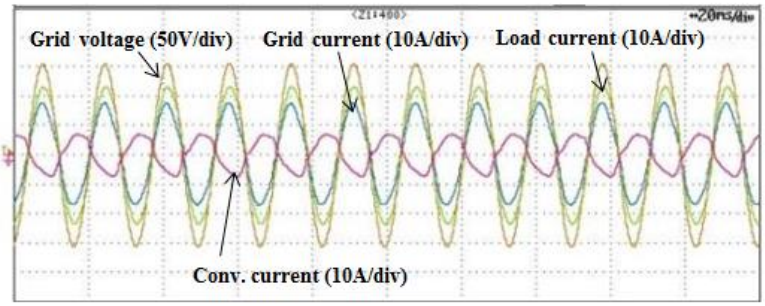

(b) P=500W

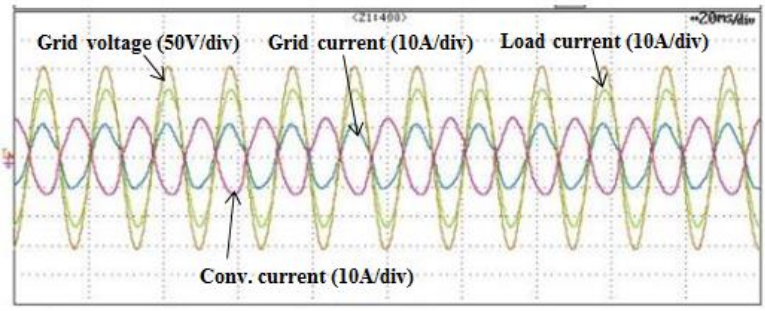

(c) P=1000W

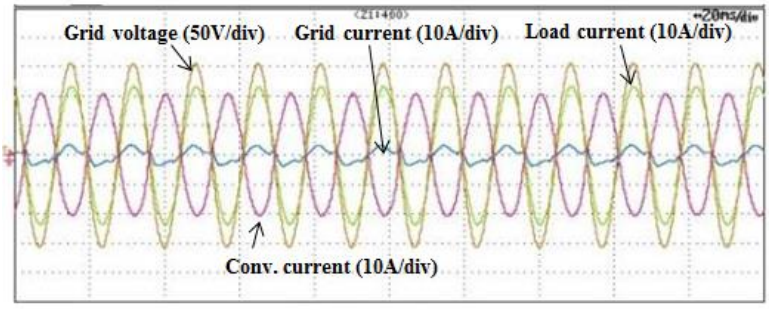

(d) P=1600W

Figure 4.36 Experimental results using the proposed power control method

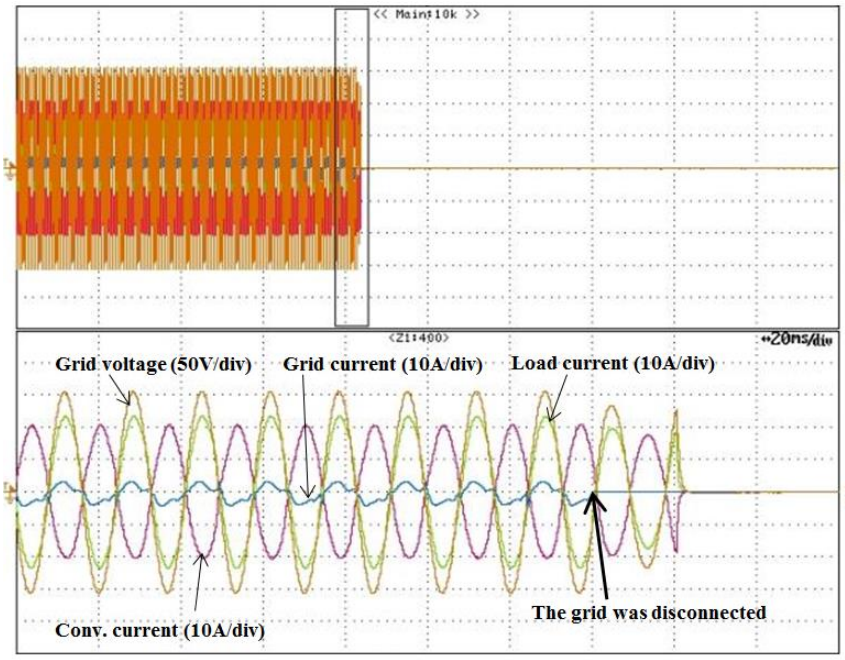

(a) with the passive method when $\Delta P>>0$ and $\Delta Q>>0$

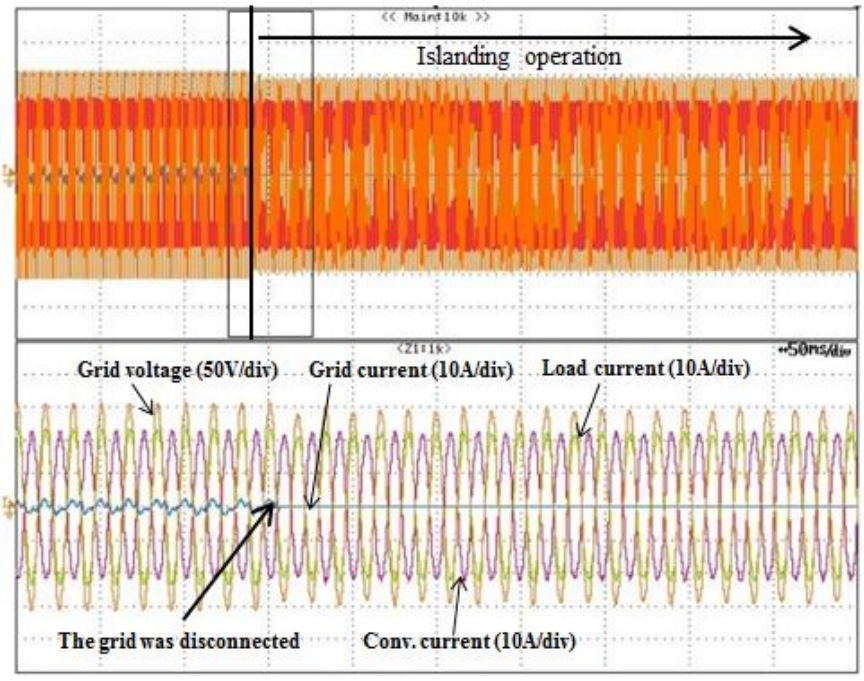

(b) with the passive method $\Delta P\approx 0$ and $\Delta Q\approx 0$

Figure 4.37 Experimental results of anti-islanding algorithms.

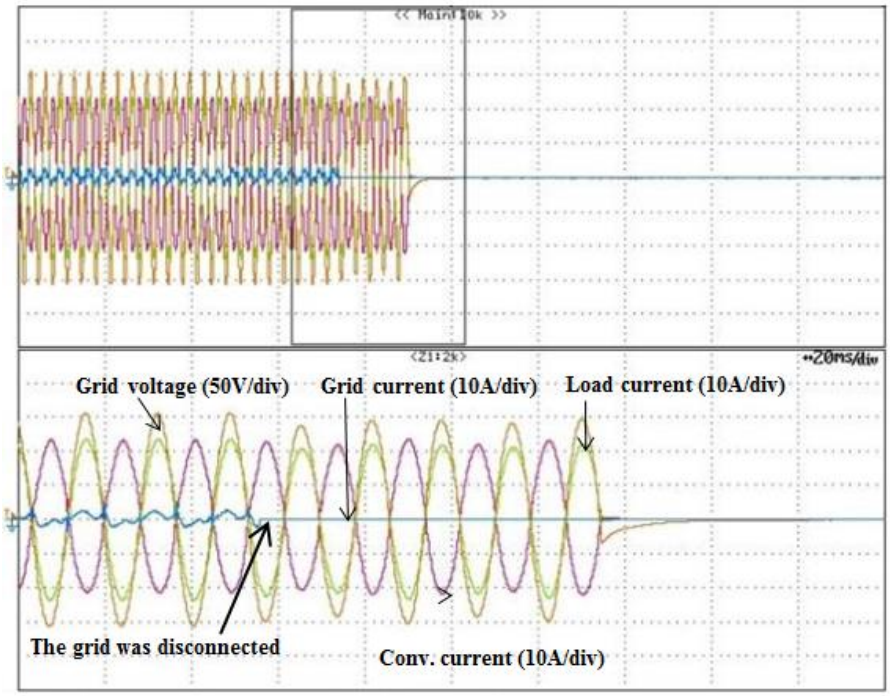

Figure 4.38 Experimental results of anti-islanding algorithms with SMS method $\Delta P \approx 0$ and $\Delta Q \approx 0$.

4.4 Summary

In this chapter, modeling approach and control method of general bidirectional converters in PV application and power control method of CHFL converters in V2G applications are proposed for residential DPSs.

1. A single-matrix-form state-space representation of the two converter stages is derived and used to achieve a better simulation strategy which can be extended to various converter topologies. Results show that the proposed state-space average model matches experiments and dynamic simulations. The proposed model also provides significant reduction in simulation runtime with aggregated inverters in addition to reduction in the simulation set-up time compared to the dynamic model. Larger step sizes were shown to be possible when using the average model to achieve both accurate and fast simulation convergence. The proposed model can be extended for other cascaded power electronic topologies.

2. Unless unintended surplus power from PV modules is regulated and limited in these conditions, this induces the over-voltage in the dc bus, resulting in tripping the PV-battery system. The power weakening control (PWC) for the PV-battery system is proposed to regulate or weaken PV power as moving operation point from the maximum power point to the open circuit voltage in the PV curve, where excessive PV power can be controlled to meet power demand of the system consisting of load power and battery power without overvoltage trip. The proposed PWC contains an extra dc voltage control loop, which is

switched automatically by a hysteresis controller in excessive power conditions to guarantee stable operation by eliminating unintended surplus power.

3. A power control method for bidirectional converters, especially for both PV and V2G systems is proposed. Most conventional methods generate current references by utilizing a phase-based equation that commonly includes the grid, anti-islanding, and reactive power phase information, which are determined by PLL algorithms, anti-islanding algorithms and active and reactive power references, respectively, resulting in increased computational burden. Whereas, the proposed method yields the trigonometric-based current references not only for active power control but also reactive power and anti-islanding algorithms, which utilize the sine and cosine terms of the grid phase from existing PLL algorithms, resulting in a reduced number of calculation steps and producing a simpler current reference generator. These advantages will allow the use of fixed point digital signal processors rather than high cost, high performance digital signal processors in single phase b-directional converter applications.

Chapter 5. Reactive power compensation in residential distributed power systems

5.1 Introduction

The smart grid can be considered as a modern electric power grid infrastructure for enhanced efficiency and reliability through sophisticated control methods for energy management, power electronics technology and modern communications infrastructure [112], [113] while microgrid is smaller scale such as building block and they can be independent of grid power system [114], [115]. Both refer to various efforts to control active and reactive power flexibly and efficiently. Their effectiveness in improvement of existing power systems have been demonstrated in field applications through many papers and reports. However, there are always economic feasibility issues in investing new infrastructures, which tend to be more discouraging than technical challenges. Therefore, it is necessary to find more cost-effective methods in this research area.

In this chapter, we aim to find a low cost solution for reactive power compensation for residential distributed power systems. Reactive power compensation along with the efficient usage of active power in residential applications is important not only for power system stability, but also energy efficient use of residential appliances. Since most power factor correction circuits in the commercial market utilize unidirectional ac-dc converter topologies, these converters have a high potential to significantly enhance the performance of load compensation and voltage regulation in ac power systems through reactive power compensation. However, reactive power compensation capabilities of unidirectional active power factor correction converters should be limited due to extended cusp distortion and

zero current distortion. These harmonic distortions can be solved by compensating harmonics from a bidirectional converter used for PV or V2G applications which will be available soon as their popularity increases. Through this process, these converters cooperatively generate reactive power locally without polluting the grid. MATLAB/ Simulink simulation results describe the performance of the proposed strategy of unidirectional and bidirectional converter control and operations.

5.2 System control

Figure 5.1 shows the overall proposed intelligent residential power system with free reactive power support, including bidirectional and unidirectional converters. Near future residential ac power systems will include: supervisory controllers that allow the utility to remotely monitor quality data and to control house loads, bidirectional and unidirectional converters as a means of achieving reliability and demand efficiencies for the utility as a whole. The supervisory controller can be embedded in either a smart meter or advanced metering interface. The unidirectional converters in our experiment will be represented by active front-end converter based loads such as heating air ventilation cooling systems (HVAC), electric vehicles, and digital appliances.

Our approach is to combine the reactive power capacities from the unidirectional converters to provide free, locally generated reactive power. Harmonics generated by the unidirectional converters will be compensated by the bidirectional converter. All commands will be issued by the supervisory controller. During this process, active power from the grid will still supply the house loads and unidirectional converters. The bidirectional converter as a renewable source will also provide active power to either the

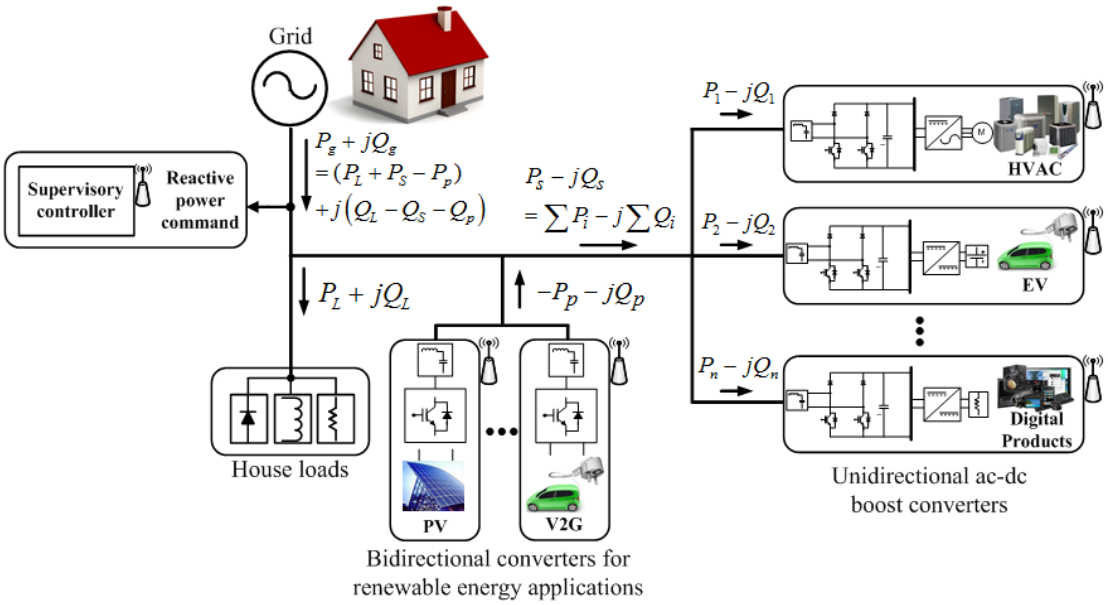

Figure 5.1 Overall proposed residential distributed power system.

unidirectional converters or house loads. Reactive power is circulated throughout the system and flows in both directions from the grid to loads and converters.

5.2.1. Unidirectional converter control

Figure 5.2 shows the control block diagram of the unidirectional ac-dc converter. Although there are many applications using the bidirectional ac-dc converters, the control method on the ac-dc converter are similar mostly whereas the control mehtod on the dc-dc converter or dc drives are different according to their applications. The main purpose is to regulate dc link output voltage while input current is made as sinusoidal as possible. Moreover, the reactive power command term from the supervisory controller is added, as

discussed in chapter 3, in order to provide reactive power. Then, through the feedback and feedforward controllers, the final duty is generated. The duty will be zero when the signs of the input voltage and current reference are opposite.

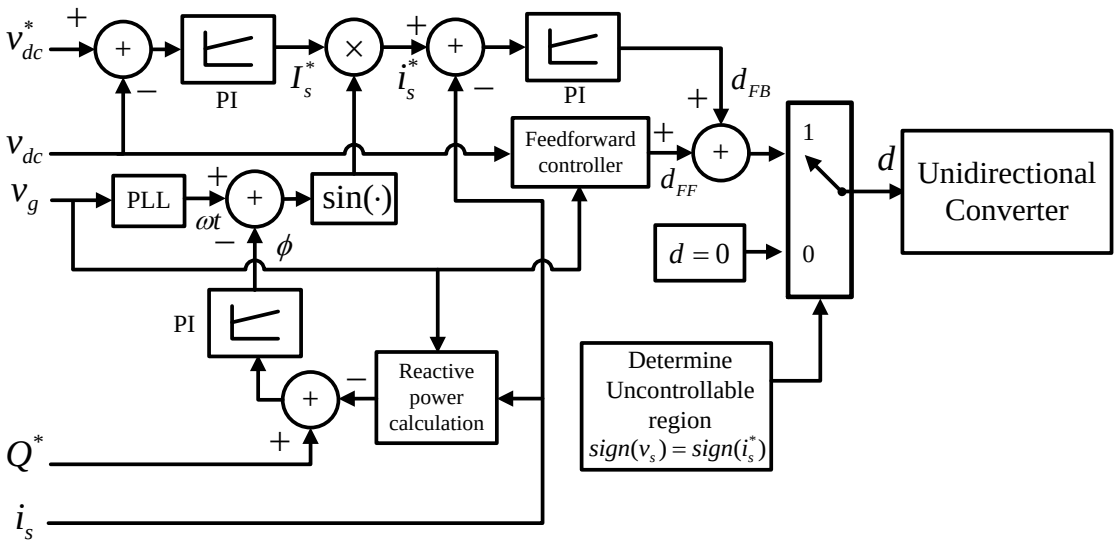

Figure 5.2 Control block of a unidirectional converter.

5.2.2. Bidirectional converter control

Bidirectional converter can be used for compensating harmonic current generated by unidirectional converters in reactive power compernsation mode. Figure 5.4 shows the power control block diagram of the bidirectional converter used for PV or V2G applications. Usually, it is comprised of two stages: a dc-dc converter that transfers active

power by extracting the maximum power point of photovoltaic panel and controlling the charging/discharging batttery current, and an ac-dc converter that transfers active power and reactive power with respect to the grid demands as discussed in chapter 4. Another role of this bidirectional ac-dc converter is to compensate harmonic currents from unidirecional converters, thus harmonic extraction terms are added in order to generate harmonic reference.

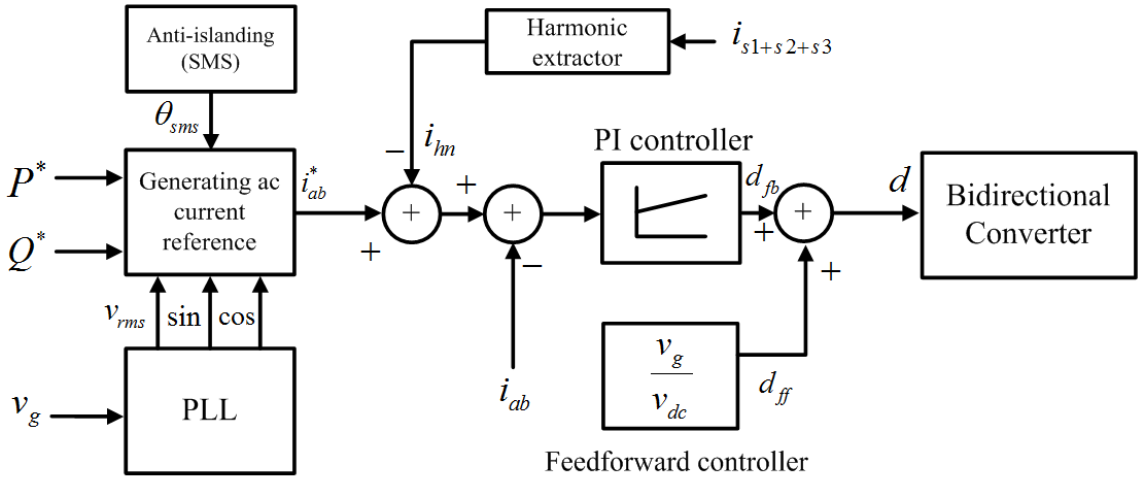

Figure 5.3 Control block of a bidirectional converter.

5.3 Simulation results

The proposed system was simulated in MATLAB/Simulink as shown in Figure 5.4. There are a bidirectional converter and three unidirectional converters along with house loads. Table 5.1 lists power rating specification of converters used for simulation model. Table 5.2 depicts five power conditions to show the capability of reactive power support from combination of the unidirectional and bidirectional converters.

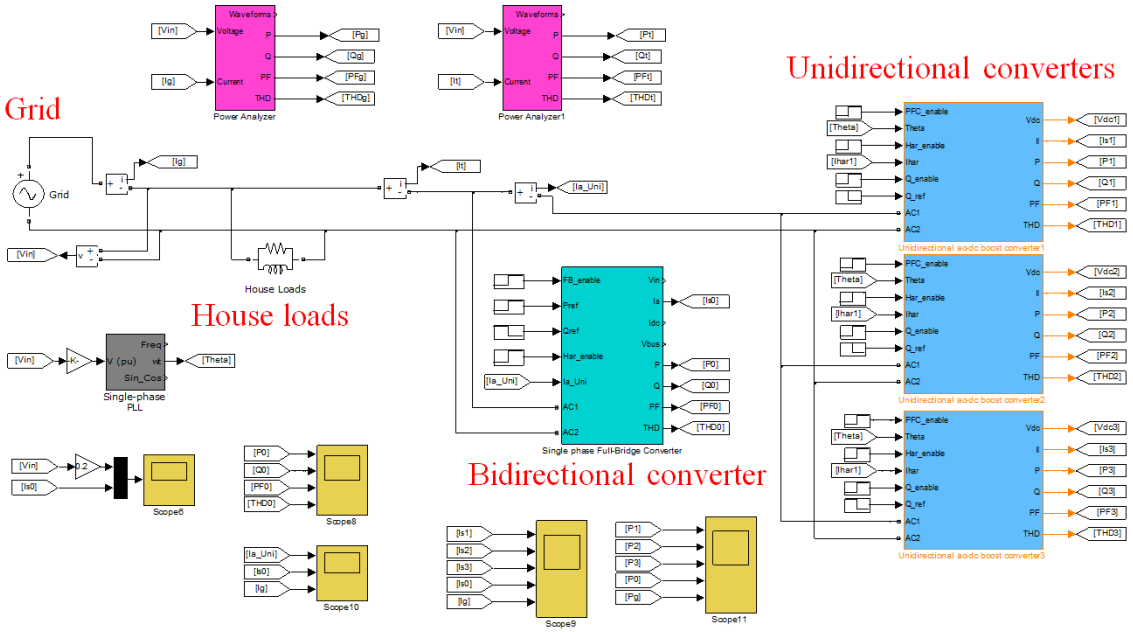

Figure 5.4 Simulation model for a residential distributed power system.

Table 5.1 List of converter power rating for simulation.

Items	*Rated Power*
AC Input Voltage	120 Vrms/60Hz
House loads (HL)	1.2-kW/ 0.9-kVar, PF:0.8
PV converter (BDG)	1.9-kVA (16A)
HVAC converter (UL#1)	1.4-kW (12A)
PHEV-EV charger 1 (UL#2)	1.9-kW (16A)
PHEV-EV charger 2 (UL#3)	1.9-kW (16A)

Table 5.2 Five different power conditions for simulation

	Grid(P + Q)	BDG(P + Q)	UL #1(P + Q)	UL #2(P + Q)	UL #3(P + Q)	HL(P + Q)
Cond. #1	3.7 kW +0.9 kVar	-1.8 kW + 0 Var	1.1 kW + 0 Var	1.5 kW + 0 Var	1.7 kW + 0 Var	1.2 kW +0.9 kVar
Cond. #2	3.7 kW +0.3 kVar	-1.8 kW -0.6 kVar	1.1 kW +0 Var	1.5 kW + 0 Var	1.7 kW + 0 Var	1.2 kW + 0.9 kVar
Cond. #3	3.7 kW +0 Var	-1.8 kW -0.6 kVar	1.1 kW -0.3 kVar	1.5 kW +0 Var	1.7 kW + 0 Var	1.2 kW +0.9 kVar
Cond. #4	3.7 kW -1 kVar	-1.8 kW -0.6 kVar	1.1 kW -0.3 kVar	1.5 kW -0.4 kVar	1.7 kW -0.6 k Var	1.2 kW +0.9 kVar
Cond. #5	3.7 kW -1 kVar	-1.8 kW -0.6 kVar	1.1 kW -0.3 k Var	1.5 kW -0.4 kVar	1.7 kW -0.6 k Var	1.2 kW +0.9 kVar

Below are short descriptions for each power condition.

- Condition 1: no reactive power support from any converters, and active power support from the BDG.

- Condition 2: active and reactive power support from the BDG.
- Condition 3: reactive power support from the BDG and UL #1, and active power support from the BDG.
- Condition 4: reactive powers support from the BDG and UL #1, 2, 3, and active power support from the BDG.
- Condition 5: the same as Condition #4, but with additional harmonic current compensation from the BDG.

Figure 5.5 shows overall current waveforms for the UL #1, #2, #3, BDG, HLs and grid system during all power conditions.

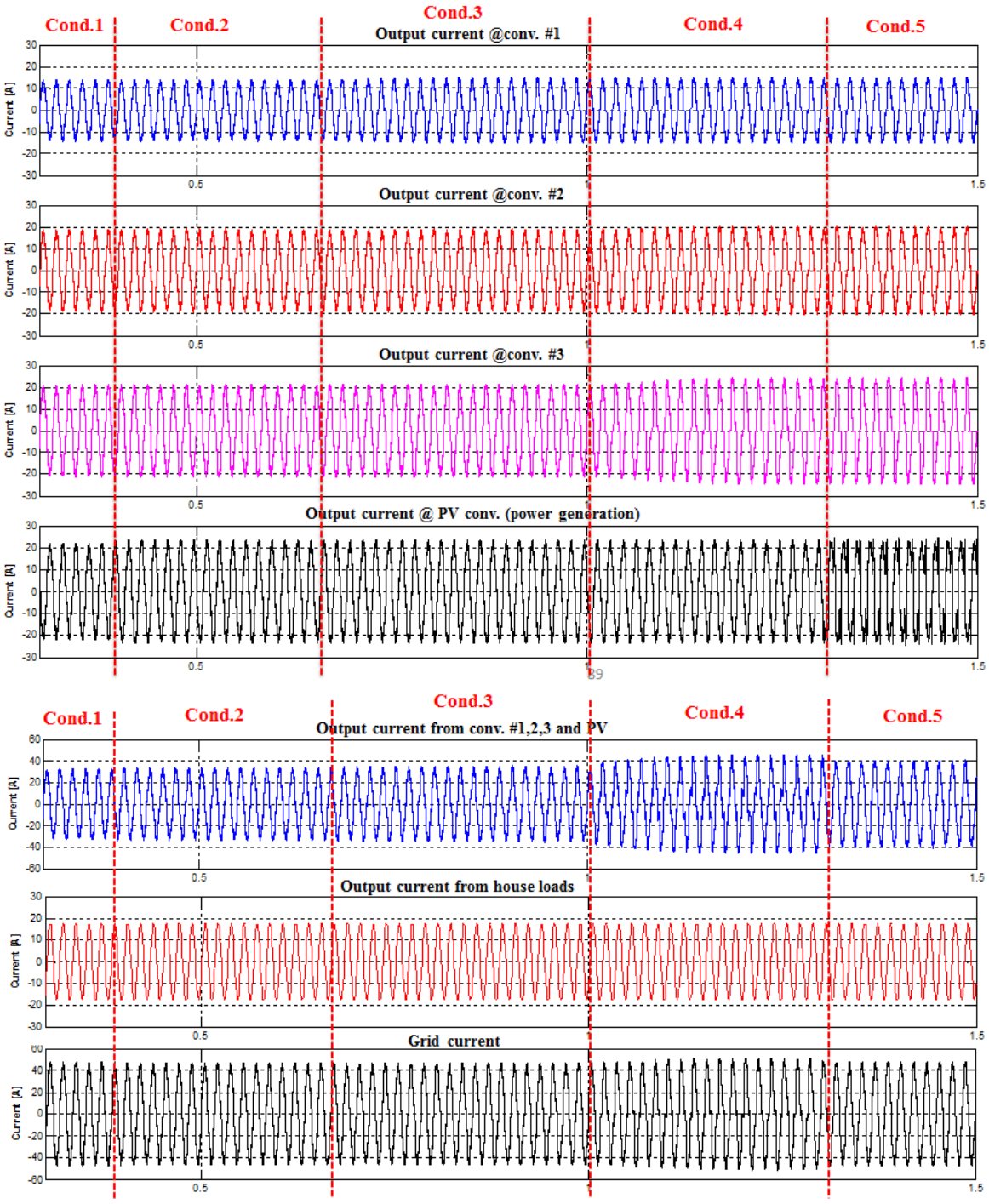

Figure 5.5 Overall current waveforms.

The detailed current waveforms in each condition are shown from Figure 5.6 to Figure 5.9. In Figure 5.6, since all ULs (#1, #2, #3) are operating at unity power factor mode and the BDG generates active power only in Condition 1, there is no harmonic distortion in the grid current lagged due to inductive house loads. When the BDG starts to provide reactive power (capacitive 600VA) during Condition 2, the PF of the grid current is improved slightly with reactive power compensation.

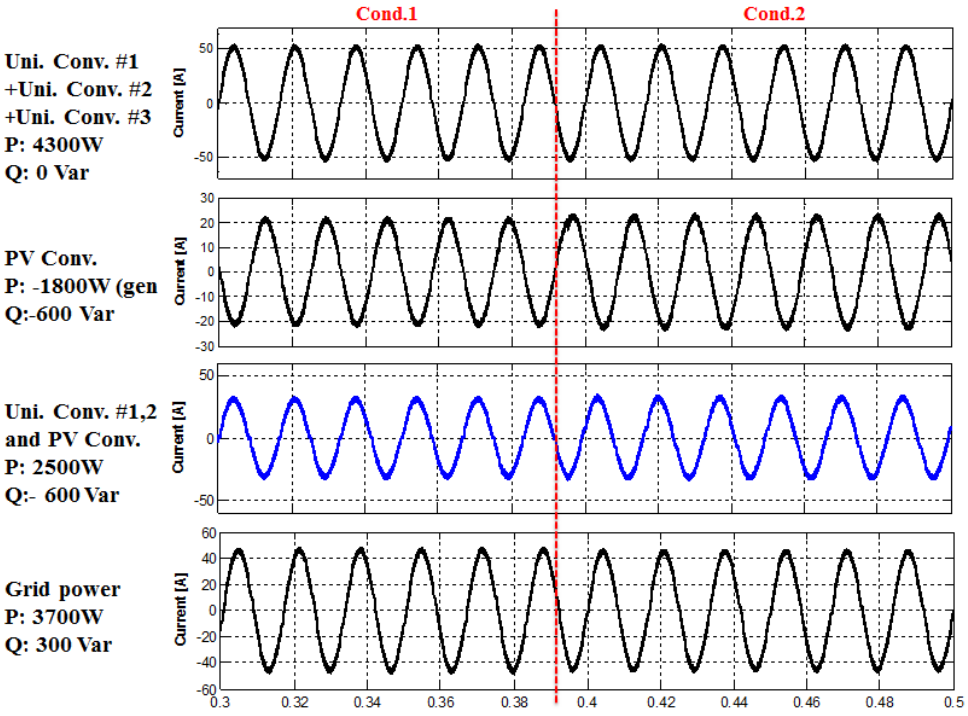

Figure 5.6 Simulation waveforms: left side - Conditions 1, right side - Conditions 2

In Figure 5.7, the UL #1 starts to generate reactive power (capacitive 300VA) along with 600VA from the BDG during Condition 3 because the grid current requires more reactive power compensation to satisfy the need of reactive power of the house load (inductive 900VA). As a result, the total reactive power of 900VA can be produced and the grid current has no displacement factor with the gird voltage. However, harmonics due to ULs #1 deteriorate the grid current slightly.

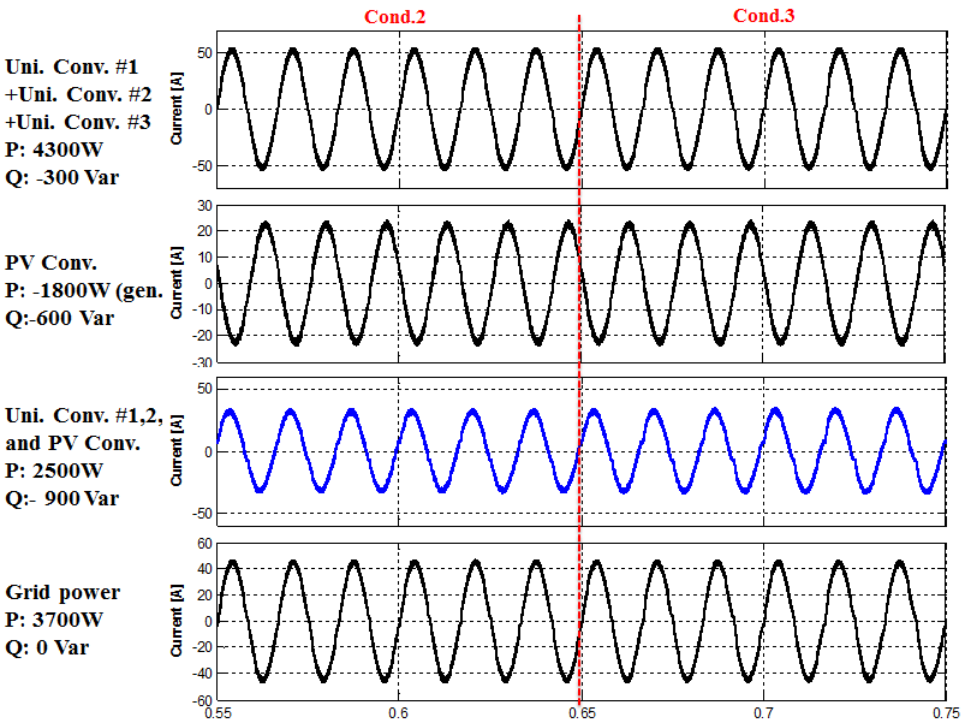

Figure 5.7 Simulation waveforms: left side - Conditions 2, right side - Conditions 3

The proposed system aims to improve overall voltage stability of the distribution power system through reactive power compensation. Not only for their internal system, but also it can provide more reactive power capability for nearby residential systems as long as the capacity remains. If there is extra reactive power demand of capacitive 1000VA from the supervisory controller for external power systems, the proposed system enables more unidirectional converters to provide reactive power. In Figure 5.8, the UL #2 and the UL #3 generate reactive power of 400 VA and 600VA during Condition 4, respectively, resulting in capacitive 1000VA, but the input current from unidirectional converters is severely distorted , which causes the grid current to be more polluted than Condition 3.

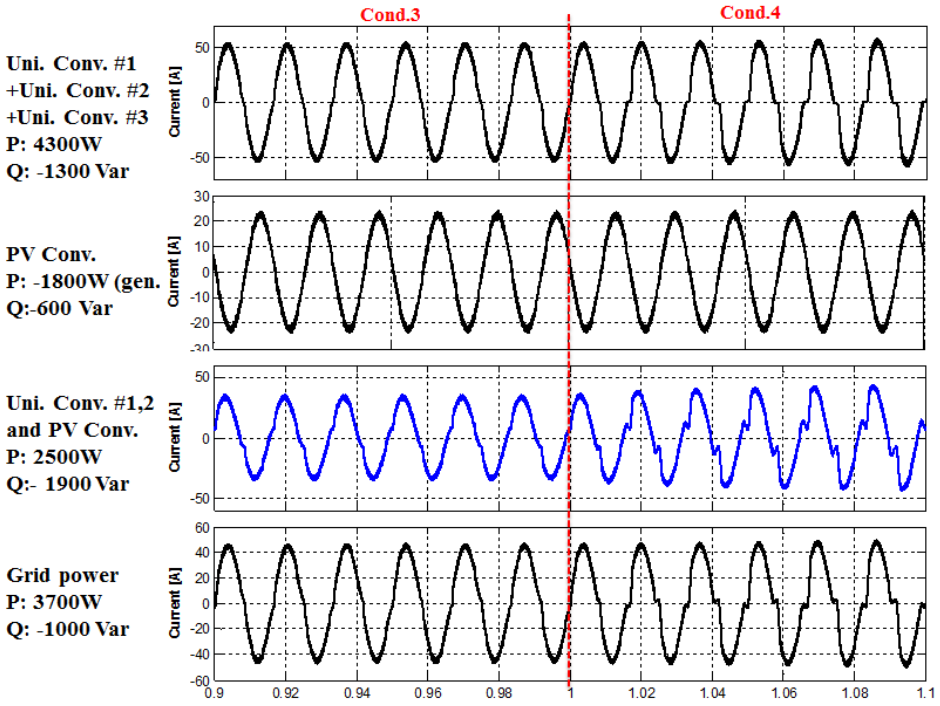

Figure 5.8 Simulation waveforms: left side - Conditions 3, right side - Conditions 4

In Condition 5, additional harmonic compensation by the BDG is enabled for cleaner grid current. Figure 5.9 shows that the output current of the BDG is intentionally distorted to compensate the harmonic current resulting in the clean grid current while the three ULs provide different amounts of active and reactive power, resulting in different current phase angles as shown in Figure 5.10. By maximizing ULs and BDG converters' reactive power and harmonic compensation capability, we enable cleaner grid current, and meet the demand for reactive power without the need for conventional reactive power compensation solutions.

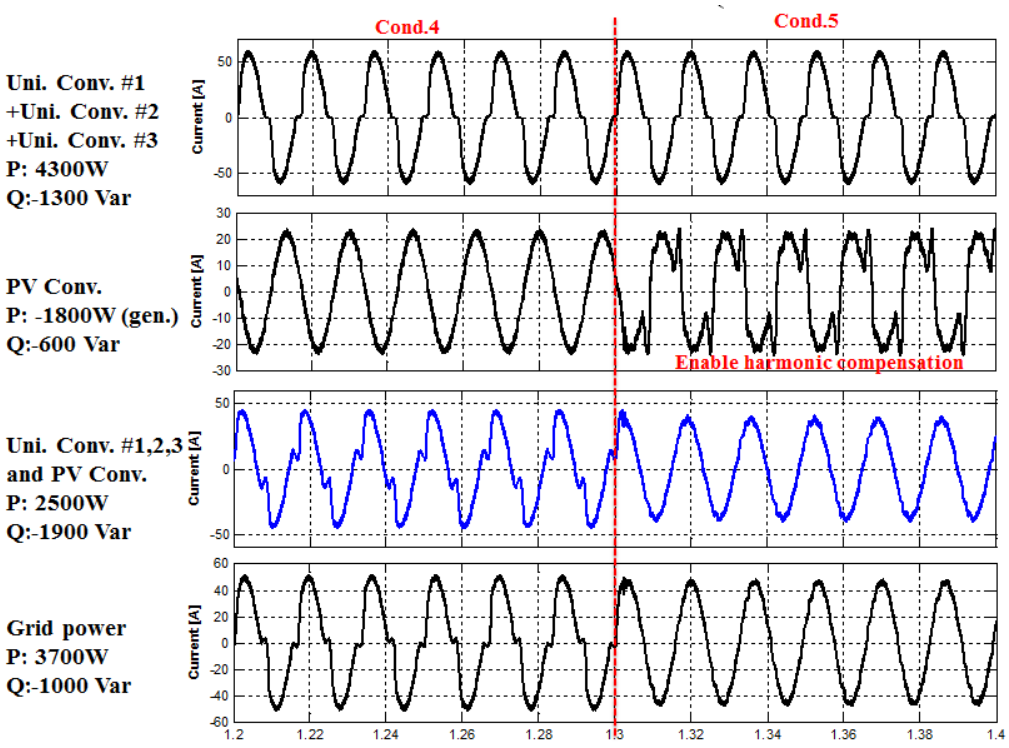

Figure 5.9 Simulation waveforms: left side - Conditions 4, right side - Conditions 5

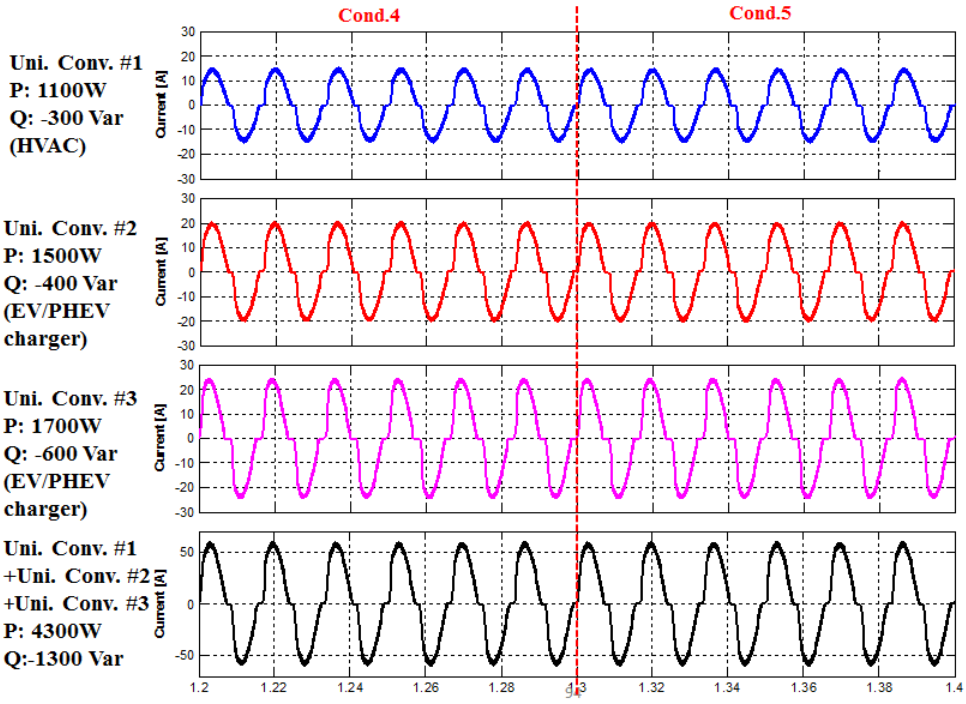

Figure 5.10 Simulation waveforms – current waveforms from three ULs

Figure 5.11 shows the active power and reactive power variations with respect to the five conditions. Reactive power compensation does not affect the primary function of feeding active power to dc loads or generating active power from a renewable energy source. Unity grid power factor as well as support for the reactive power demand is achieved by three ULs. Figure 5.12 shows the power factor and THD current variations with respect to the five conditions. Initially, the grid provides reactive power to the house load. Later, the grid absorbs the reactive power generated by the ULs. In Conditions 3 and 4, THD was increased due to the influence of the ULs. However, after enabling harmonic compensation from the BDG, the grid THD is decreased dramatically. Eventually, the proposed integration of ULs and BDGs effectively provide zero power pollution to the grid.

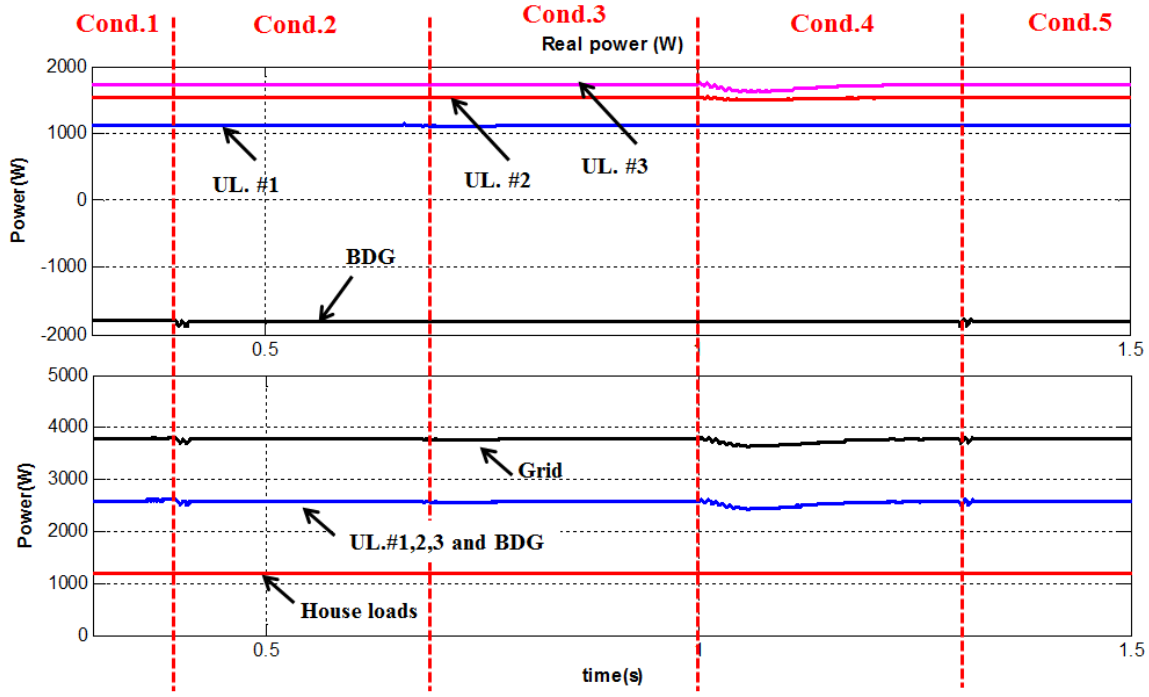

(a) Active power

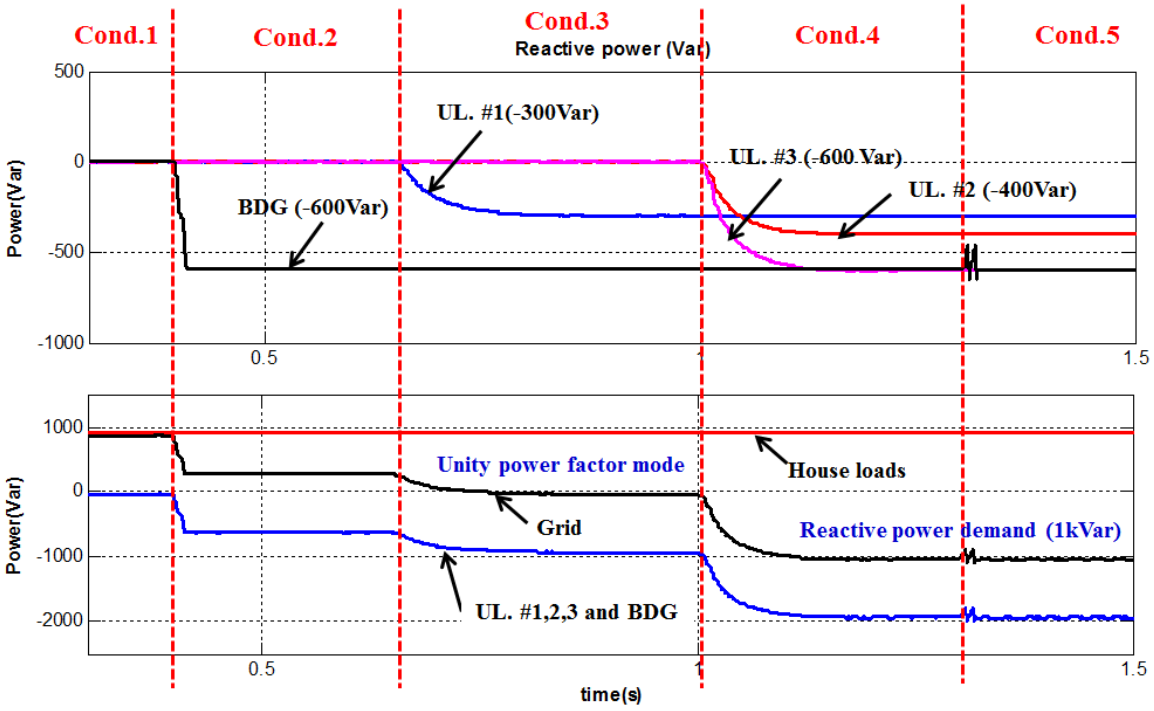

(b) Reactive power

Figure 5.11 Simulation waveforms: active power and reactive power.

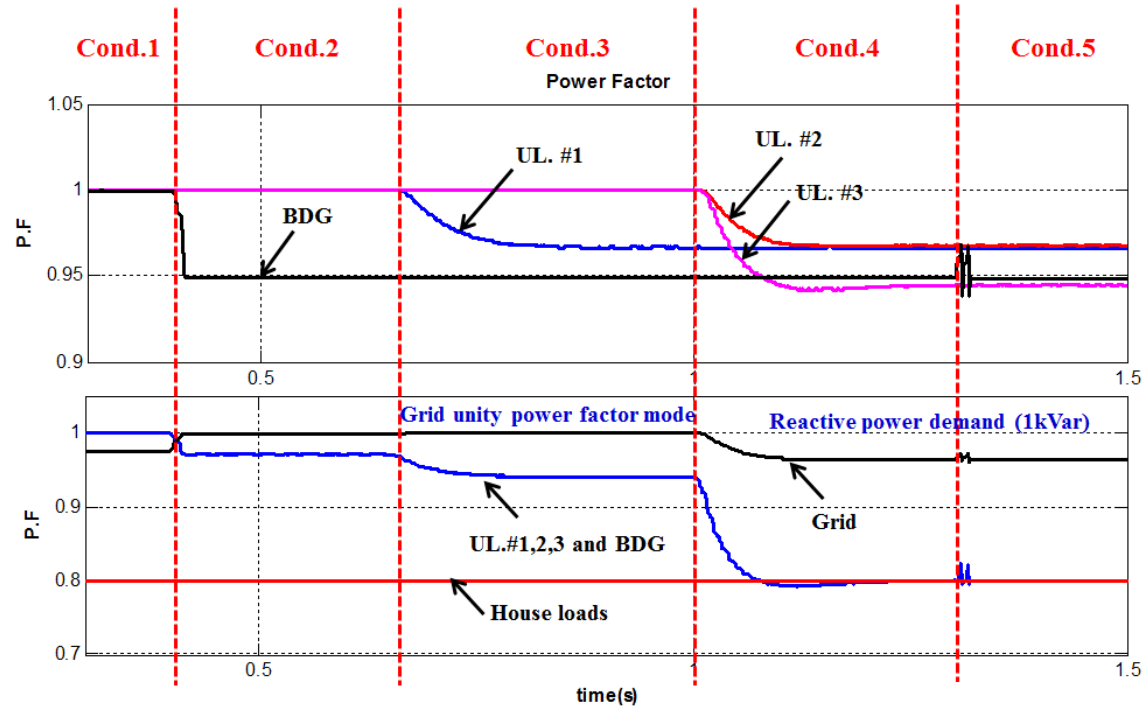

(a) Power factor

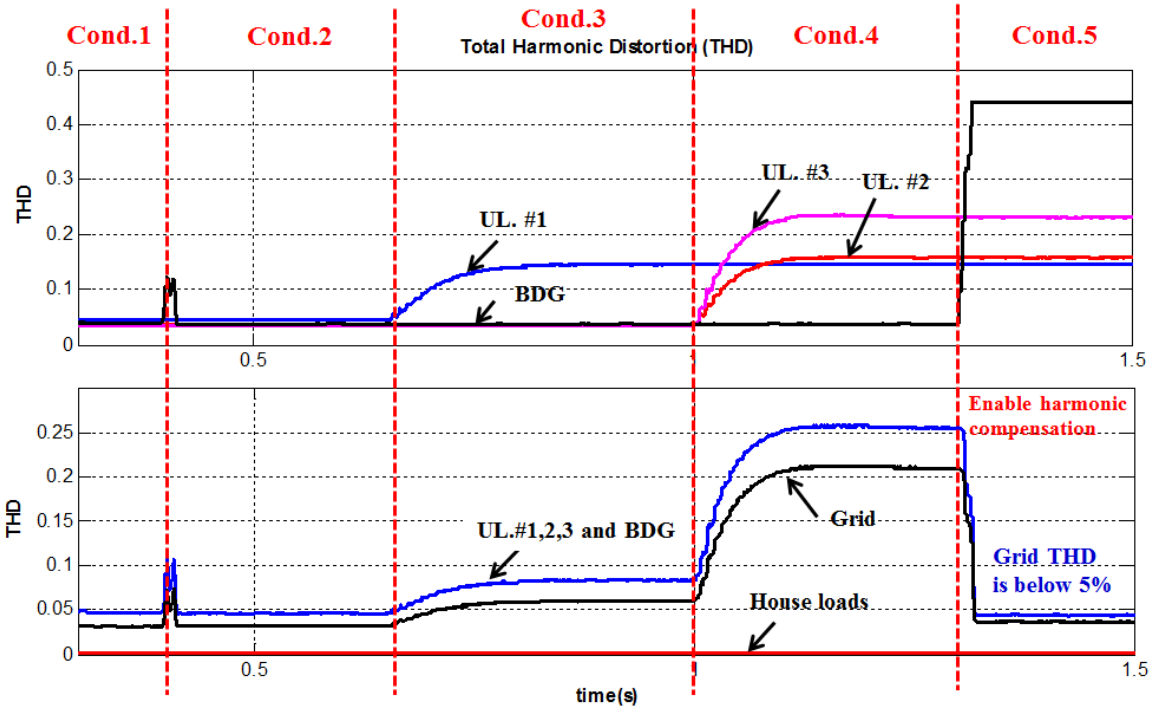

(b) THD

Figure 5.12 Simulation waveforms: PF and THD.

5.4 Summary

Full utilization of reactive power compensation capabilities in unidirectional converters was proposed by creating a system of converters, including a bidirectional converter. Using unidirectional power factor correction converters typically employed within electric vehicles or home appliances, significant reactive power could be generated, but the input currents were distorted due to the extended cusp distortion and zero current distortion as discussed in chapter 3. A bidirectional converter compensated the harmonic distortions. Eventually, these converters cooperatively generate reactive power locally without polluting the grid.

Chapter 6. Conclusion

6.1 Summary and contributions

This dissertation investigates control and integration strategies for bidirectional and unidirectional converters in residential distributed power systems to maximize reactive power support capabilities of existing aggregated unidirectional converters.

Usually, unidirectional power factor correction converters are utilized in many commercial applications as front-end circuitry in order to minimize the effects of harmonics distortion and poor power factor. Since these converters are commonly used, they have great potential as huge reactive power storages in distribution level power systems. However, the distortion of input current as a result of reactive power compensation cannot be avoided due to intrinsic topology limitations. This drawback can be mitigated by employing bidirectional converters which would be incorporated in electric vehicles and photovoltaic systems, which are becoming increasingly available as residential distributed generation systems.

In this dissertation, the current distortion of the unidirectional converter under reactive power compensation is analytically explained and the performance of unidirectional converters as an active power filter is evaluated. Control methods of bidirectional converters in photovoltaic and vehicle-to-grid systems are investigated. Finally, an integration strategy for controlling bidirectional and unidirectional converters is proposed. Even though unidirectional active PFC loads have limited reactive power generation capabilities due to the extended cusp distortion and zero current distortion, the proposed integration method enables reactive power support without any additional cost.

The outcome of this dissertation will contribute free reactive power support without harmonic pollution in residential distributed generation systems. The following contributions are drawn from the work.

- **Control method for unidirectional PFC converters ([J2],[C7], [C9])**
  1. Control methods for unidirectional PFC converters were studied through these papers and are utilized for describing state of the art control methods in unidirectional PFC converter applications.
  2. The conventional control scheme depends on only the performance of the current-loop compensator to eliminate lagging-phase effects. As a result, the converter encounters a non-unity power factor if the bandwidth of the current-loop compensator is limited.
  3. The input impedance and current (IIC) feedforward control method for the unidirectional PFC converter was proposed to solve the phase shift problems of the input current caused by lagging-phase admittances in low switching/sampling and high line frequency applications. The effectiveness of the proposed method was analyzed through small-signal input admittances, the distortion and contribution factors.
- **Active power filter functionalities in the unidirectional PFC converter ([J1], [C3])**
  1. Versatile control methods for unidirectional ac-dc boost converters were investigated for the purpose of mitigating grid power quality: harmonic current compensation, reactive power compensation and both harmonic current and reactive

power compensation modes simultaneously.

2. The framework for evaluation of the current distortion levels in unidirectional ac-dc boost converters was presented. Due to the inherent limitations of the unidirectional ac-dc boost converter, the grid current will be distorted unintentionally when operating in reactive power compensation mode where the THD of capacitive current is worse than that of the inductive current due to extended cusp distortions. Hence, the amount of reactive power injected from an individual converter to the grid should be restricted.

- **Control method for bidirectional converters in renewable energy applications ([P1], [C1], [C4], [C6], [C8])**

1. Control and modeling methods for bidirectional converters in PV applications were studied through these papers and will be utilized for control strategies along with a simple power control method for V2G applications in the dissertation.
2. The control algorithm for the PV-battery system was investigated. It allows the system to work in off-grid mode and seamlessly transition from off-grid to grid connected mode and vice versa, without changing the control algorithm when changing modes of operation.
3. Unless unintended surplus power from PV modules is regulated and limited in excessive power conditions, this induces the over-voltage in the dc bus, resulting in tripping the PV-battery system. To solve this problem a power weakening control (PWC) was proposed to regulate or weaken PV power by moving the operation point from the maximum power point to the open circuit voltage in the PV curve .

4. A single state-space representation of the two converter stages is used to achieve a better simulation strategy which can be extended to various converter topologies. The proposed model also provides significant reduction in simulation runtime with aggregated micro-inverters in addition to reduction in the simulation set-up time compared to the dynamic model. Larger step sizes were shown to be possible when using the average model to achieve both accurate and fast simulation convergence.
5. An active/reactive power control method of bidirectional converters in single-phase power systems based on the stationary ac current control is proposed. Since the proposed method employs trigonometric angles of the grid phase directly rather than the grid phase itself, the computation time for calculating angles is minimized.

- **Integration Strategy for bidirectional and unidirectional converters in residential distributed power systems ([C2])**

1. Full utilization of unidirectional converters for maximizing their reactive power compensation capabilities was proposed by creating a system of converters, including a bidirectional DG converter.

2. Even though unidirectional PFC converters have limited reactive power generation capabilities due to the extended cusp distortion and zero current distortion, the proposed integration method enables reactive power support without any additional cost.

6.2 Scholarly contributions

- **Patents**

[P1] **S.M. Park**, S.Y. Park, S. Ramsay, M. Kelley, M. Tarca, J. Thompson, D. Gellis, and T. Parsons, "Reference Current Generation in Bidirectional Power Converter" Invention disclosure, UConn case 14-049 (vehicle-to-grid collaboration with DRS)

[P2] **S.M. Park**, S.Y. Park, S. Ramsay, M. Kelley, M. Tarca, J. Thompson, D. Gellis, and T. Parsons, "Predictive Current Control in Bidirectional Power Converter" Invention disclosure, UConn case 14-049 (vehicle-to-grid collaboration with DRS)

- **Journal papers**

[J1] **S.M. Park** and S.Y. Park, "Versatile Control of Unidirectional AC-DC Boost Converter for Power Quality Mitigation," *IEEE Trans. Power Electron*, 2014, Accepted.

[J2] **S.M. Park**, S.Y. Park, and A.M. Bazzi, "Input Impedance and Current Feedforward Control of Single-Phase Boost PFC Converters," in *Journal of Power Electronics*, 2015, Accepted.

- **Conference papers**

[C1] **S.M. Park**, S.Y. Park, M. Kelley and M. Tarca, "Trigonometric Angle Based Active/Reactive Power Control of Cycloconverter-Type High-Frequency Link Converter for Vehicle-to-Grid Applications" *2015 IEEE Energy Conversion Congress and Exposition (ECCE 2015)*, Submitted.

[C2] J. Ivaldi, **S.M. Park**, S.Y. Park, "Integration Strategy for Bi-directional and Uni-directional Converters Aiming for Zero Power Pollution in Residential Applications", *ICPE 2015-ECCE Asia*, Accepted

[C3] **S.M. Park** and S.Y. Park, "Versatile Unidirectional AC-DC Converter with Harmonic Current and Reactive Power Compensation for Smart Grid Applications," *Applied Power Electronics Conference and Exposition (APEC)*, 2014 Twenty- Ninth Annual IEEE, pp.2163-2170, Mar. 2014.

[C4] **S.M. Park**, A.M. Bazzi, S.Y. Park and W. Chen, "A Time-Efficient Modeling and Simulation Strategy for Aggregated Multiple Microinverters in Large-Scale PV Systems," *Applied Power Electronics Conference and Exposition (APEC)*, 2014 Twenty- Ninth Annual IEEE, pp.2754-2761, Mar. 2014.

[C5] **S.M. Park**, S.Y. Park, P. Zhang, P. Luh, M. Rakotomavo and C. Serna, "Life Cycle Cost Analysis of Hardening Options for Critical Loads," *5th Innovative Smart Grid Technologies Conference (ISGT)*, 2014 IEEE PES, pp.1-5, Feb. 2014.

[C6] **S.M. Park** and S.Y. Park, "Power weakening control of the photovoltaic-battery system for seamless energy transfer in microgrids," *Applied Power Electronics Conference and Exposition (APEC)*, 2013 Twenty-Eighth Annual IEEE , pp. 2971-2976, Mar. 2013.

[C7] **S.M. Park** and S.Y. Park, "Input impedance and current feedforward control for leading-lagging phase admittance cancellation in the AC-DC boost converter," *Applied Power Electronics Conference and Exposition (APEC)*, 2013 Twenty-Eighth Annual IEEE , pp. 1912-1919, Mar. 2013.

[C8] L. Arnedo, S. Dwari, V. Blasko and **S.M. Park**, "80 kW hybrid solar inverter for standalone and grid connected applications," *Applied Power Electronics Conference and Exposition (APEC)*, 2012 Twenty-Seventh Annual IEEE , pp. 270-276, Feb. 2012.

[C9] **S.M. Park**, Y.D. Lee and S.Y. Park, "Voltage sensorless feedforward control of a dual boost PFC converter for battery charger applications," *Energy Conversion Congress and Exposition (ECCE)*, 2011 IEEE , pp. 1376-1380, 17-22 Sep. 2011.

Reference

[1] A. von Jouanne, P.N. Enjeti and B. Banerjee, "Assessment of ride-through alternatives for adjustable-speed drives," *IEEE Trans. Ind. Appl*., vol. 35, no. 4, pp.908-916, Jul/Aug 1999.

[2] Ross Ignall Dranetz, Power Quality Analysis Teams with Energy Audits to Enhance Facility Uptime, [Online]. Available; http://www.utilityproducts.com/

[3] N.G. Hingorani, "Power electronics in electric utilities: Role of power electronics in future power systems," *Proc. IEEE*, vol. 76, no. 4, pp. 481– 482, Apr. 1988.

[4] N.G. Hingorani, "Flexible AC transmission," *IEEE Spectr*., vol. 30, no. 4, pp. 40–45, Apr. 1993.

[5] N.G. Hingorani and L. Gyugyi, "Understanding FACTS: concepts and technology of flexible AC transmission systems", IEEE press, 2000.

[6] P. S. Sensarma, K.R. Padiyar and V. Ramanarayanan, "Analysis and performance evaluation of a distribution STATCOM for compensating voltage fluctuations," *IEEE Trans. Power Delivery*, vol. 16, no. 2, pp.259-264, Apr. 2001.

[7] ABB Flexible Alternating Current Transmission System, [Online] Available; http://new.abb.com/facts

[8] B. Singh, K. Al-Haddad, and A. Chandra, "A review of active filters for power quality improvement," *IEEE Trans. Ind. Electron.*, vol. 46, no. 5, pp. 960–971, Oct. 1999.

[9] M. El-Habrouk, M. K. Darwish, and P. Mehta, "Active power filters: A review," *Proc. Inst. Elect. Eng.—Electr. Power Appl.*, vol. 147, no. 5, pp. 403–413, Sep. 2000.

[10] S. Chowdhury, S.P. Chowdhury and P. Crossley, "*Microgrids and Active Distribution Networks*", IET, 2009.

[11] Delta APF Series Active Power Filter, [Online] Available; http://www.delta.com.tw/

[12] M. Singh, V. Khadkikar, A. Chandra and R.K. Varma, "Grid Interconnection of Renewable Energy Sources at the Distribution Level With Power-Quality Improvement Features," *IEEE Trans. Power Delivery*, vol. 26, no. 1, pp.307-315, Jan. 2011.

[13] R. I. Bojoi, L. R. Limongi, D. Roiu, and A. Tenconi, "Enhanced power quality control strategy for single-phase inverters in distributed generation systems," *IEEE Trans. Power Electron*., vol. 26, no. 3, pp. 798–806, Mar. 2011.

[14] W. Kempton and E. L. Steven, "Electric vehicles as a new source of power for electric utilities," *Transp. Res.*, vol. 2, no. 3, pp. 157–175, 1997.

[15] M.C. Kisacikoglu, B. Ozpineci and L.M. Tolbert, "EV/PHEV Bidirectional Charger Assessment for V2G Reactive Power Operation," *IEEE Trans. Power Electro*n., vol. 28, no. 12, pp. 5717-5727, Dec. 2013.

[16] Kai-Wei Hu and Chang-Ming Liaw, "On a Bidirectional Adapter With G2B Charging and B2X Emergency Discharging Functions," *IEEE Trans. Ind. Electron*, vol. 61, no. 1, pp.243-257, Jan. 2014.

[17] M. Yilmaz and P.T. Krein, “Review of Battery Charger Topologies, Charging Power Levels, and Infrastructure for Plug-In Electric and Hybrid Vehicles,” *IEEE Trans. Power Electron*, vol. 28, no. 5, pp.2151-2169, May. 2013.

[18] B. Singh, B. N. Singh, A. Chandra, K. Al-Haddad, A. Pandey, and D. P. Kothari, “A review of single-phase improved power quality ac-dc converters,” *IEEE Trans. Ind. Electron*., vol. 50, no. 5, pp. 962–981, Oct. 2003.

[19] M. M. Jovanovic and Y. Jang, “State-of-the-art, single-phase, active power-factor-correction techniques for high-power applications—An overview,” *IEEE Trans. Ind. Electron*., vol. 52, no. 3, pp. 701–708, Jun. 2005.

[20] Y. Li and T. Takahashi, “A digitally controlled 4-kW single-phase bridge-less PFC circuit for air conditioner motor drive applications,” *in Proc. CES/IEEE 5th IPEMC*, Aug. 2006, vol. 1, pp. 1–5.

[21] A. Murray and Yong Li, "Motion Control Engine Achieves High Efficiency with Digital PFC Integration in Air Conditioner Applications," *in Proc. IEEE Int. Symp. Elect. And Envir*., 2006, pp.120-125.

[22] L. Huber, Y. Jang, and M. M. Jovanovic, “Performance evaluation of bridgeless PFC boost rectifiers,” *IEEE Trans. Power Electron*., vol. 23, no. 3, pp. 1381–1390, May 2008.

[23] N.R. Hamzah, M.K. Hamzah, A.S. Abu Hasim, and N.F.A.A. Rahman, “Single-phase shunt active power filter using single-switch incorporating boost circuit,” *in Proc. IEEE Int. Pow. And Ener. Conf. (PECon)*, 2008, pp. 1112-1117.

[24] M. A. Fasugba and P. T. Krein, “Gaining vehicle-to-grid benefits with unidirectional electric and plug-in hybrid vehicle chargers,” *in Proc. IEEE Veh. Power and Propulsion Conf*., Sep. 2011, pp. 1–6.

[25] Surya Santoso, *Fundamentals of Electric Power Quality*, Scotts Valley, CA: CreateSpace, 2012.

[26] IEC 1000-3,*Electromagnetic Compatibility Part 3:Limits*, Mar. 1995.

[27] ″Electromagnetic compatibility (EMC) part 3-2: Limits for harmonic cur-rent emissions (equipment input current≤16A per phase),” EN 61000-3-2,2006.

[28] G.G. Park, K.Y. Kwon, and T.W. Kim, “PFC Dual Boost Converter Based on Input Voltage Estimation for DC Inverter Air Conditioner,” *Journal of Power Electronics*, vol. 10,no. 3, May 2010.

[29] [Online] Available; www.electronicdesign.com

[30] [Online] Available; www.silabs.com

[31] B. Singh, B. N. Singh, A. Chandra, K. Al-Haddad, A. Pandey, and D. P. Kothari, “A review of single-phase improved power quality ac-dc converters,” *IEEE Trans. Ind. Electron*., vol. 50, no. 5, pp. 962–981, Oct. 2003.

[32] B. Singh and S. Singh, “Single-phase power factor controller topologies for permanent magnet brushless DC motor drives,” *IET Power Electron*., vol. 3, no. 2, pp. 147–175, Mar. 2010.

[33] J.G Kassakian and T.M. Jahns, "Evolving and Emerging Applications of Power Electronics in Systems," *IEEE Journal of Emerging and Selected Topics in Power Electron.*, vol. 1, no. 2, pp. 47-58, Jun. 2013.

[34] D. Maksimovi´ c, Y. Jang, and R. W. Erickson, “Nonlinear-carrier control for high-power-factor boost rectifiers,” *IEEE Trans. Power Electron*., vol. 11, no. 4, pp. 578–584, Jul. 1996.

[35] Y. Notohara, T. Suzuki, T. Endo, H. Umeda, A. Okuyama, Y. Funayama, and K. Tamura, “Controlling power factor correction converter for single-phase AC power source without line voltage sensor,” in *Proc. Int. Power Elect. Conf. (IPEC*),Jun. 2010, pp. 431-436.

[36] B.A. Mather and D. Maksimović, "A Simple Digital Power-Factor Correction Rectifier Controller," *IEEE Trans. Power Electron., vol. 26, no. 1, pp. 9-19, Jan. 2011.*

[37] J. Chiang, B. Liu, and S. Chen, “A simple implementation of nonlinear-carrier control for power factor correction rectifier with variable slope ramp onfield-programmable gate array,”*IEEE Trans. Ind. Informat.*, vol. 9, no. 3, pp. 1322–1329, Aug. 2013.

[38] J. Chen, A. Prodic´, R. W. Erickson, and D. Maksimovic´, “Predictive digital current programmed control,” *IEEE Trans. Power Electron.*, vol. 18, no. 1, pt. Part 2, pp. 411–419, Jan. 2003.

[39] P. Athalye, D. Maksimovic, and R. W. Erickson, “DSP implementation of a single-cycle predictive current controller in a boost PFC rectifier,” in *Proc. IEEE Appl. Power Electron. Conf. Expo*., 2005, pp. 837–842.

[40] L. Roggia, F. Beltrame, J.E Baggio, and J Renes Pinheiro, "Digital current controllers applied to the boost power factor correction converter with load variation," *IET Power Electron*., vol. 5, no. 5, pp.532-541, May 2012.

[41] K. P. Louganski and J.-S. Lai, “Current phase lead compensation in single-phase PFC boost converters with a reduced switching frequency to line frequency ratio,” *IEEE Trans. Power Electron*., vol. 22, no. 1, pp. 113–119, Jan. 2007.

[42] S.Y. Park, C.L. Chen, J.-S. Lai, and S.R. Moon, "Admittance Compensation in Current Loop Control for a Grid-Tie LCL Fuel Cell Inverter," *IEEE Trans. Power Electron*., vol. 23, no. 4, pp. 1716-1723, Jul. 2008

[43] D. M. Van de Sype, K. De Gusseme, A. P. M. Van den Bossche, and J. A. Melkebeek, “Duty-ratio feedforward for digitally controlled boost PFC converters,” *IEEE Trans. Ind. Electron.*, vol. 52, no. 1, pp. 108–115, Feb. 2005.

[44] Min Chen and Jian Sun, “Feedforward current control of boost single-phase PFC converters” *IEEE Trans. Power Electron*, vol. 21, no. 2, pp. 338- 345, Mar. 2006.

[45] K.I. Hwu, H.W. Chen, and Y.T. Yau, "Fully Digitalized Implementation of PFC Rectifier in CCM Without ADC," *IEEE Trans. Power Electron* , vol. 27, no. 9, pp. 4021-4029, Sept. 2012.

[46] Y.H Cho and J.S. Lai, "Digital Plug-In Repetitive Controller for Single-Phase Bridgeless PFC Converters," *IEEE Trans. Power Electron.*, vol. 28, no. 1, pp. 165-175, Jan. 2013.

[47] V.M. Lopez, F.J. Azcondo, A. de Castro, and R. Zane, "Universal Digital Controller for Boost CCM Power Factor Correction Stages Based on Current Rebuilding Concept," *IEEE Trans. Power Electron.*, vol. 29, no. 7, pp. 3818-3829, Jul. 2014.

[48] A. Sanchez, A. de Castro, V.M. Lopez, F.J. Azcondo, and J. Garrido, "Single ADC Digital PFC Controller Using Precalculated Duty Cycles," *IEEE Trans. Power Electron.*, vol. 29, no. 2, pp. 996-1005, Feb. 2014.

[49] M. Pahlevani, P. Shangzhi, S. Eren, A. Bakhshai, and P. Jain, "An Adaptive Nonlinear Current Observer for Boost PFC AC/DC Converters," *IEEE Trans. Ind. Electron.*, vol. 61, no. 12, pp. 6720-6729, Dec. 2014.

[50] C.L. Nguyen, H.H. Lee, and T.W. Chun, "A Simple Grid Voltage-Sensorless Control Scheme for PFC Boost Converters," *Journal of Power Electronics*, Vol. 14, No. 4, pp. 712-721, Jul. 2014.

[51] H.J. Kim, G.S. Seo, B.H. Cho, and H.S. Choi, "A Simple Average Current Control With On-Time Doubler for Multiphase CCM PFC Converter," *IEEE Trans. Power Electron.*, vol. 30, no. 3, pp. 1683-1693, Mar. 2015.

[52] AC-DC Converter having an improved power factor' US Patent Publication No. US 4412277 A, 25/10/1983

[53] F. Musavi, W. Eberle, and W. G. Dunford, "A high-performance single-phase bridgeless interleaved PFC converter for plug-in hybrid electric vehicle battery chargers," *IEEE Trans. Ind. Appl.*, vol. 47, no. 4, pp. 1833–1843, Jul./Aug. 2011.

[54] J. Sun, "Input impedance analysis of single-phase PFC converters," *IEEE Trans. Power Electron*., vol. 20, no. 2, pp. 308–314, Mar. 2005.

[55] R. Majumder, "Reactive Power Compensation in Single-Phase Operation of Microgrid," *IEEE Trans. Ind. Electron.*, vol. 60, no. 4, pp.1403-1416, Apr. 2013.

[56] J. Dixon, L. Moran, J. Rodriguez, and R. Domke, "Reactive power compensation technologies: State-of-the-art review," *Proc. IEEE*, vol. 93, no. 12, pp. 1244–1264, Dec. 2005.

[57] J. W. Kolar and T. Friedli, "The Essence of Three-Phase PFC Rectifier Systems—Part I," *IEEE Trans. Power Electron*., vol. 28, no. 1, pp. 176-198, Jan. 2013.

[58] D. Boroyevich, I. Cvetkovic, R. Burgos, and D. Dong, "Intergrid: A Future Electronic Energy Network?," *IEEE J. Emerging Sel. Topics Power Electron.*, vol. 1, no. 3, pp. 127-138, Sep. 2013.

[59] J. Sun, "On the zero-crossing distortion in single-phase PFC converters," *IEEE Trans. Power Electron*., vol. 19, no. 3, pp.685–692, May 2004.

[60] S. Sivakumar, K. Natarajan, and R. Gudelewicz., "Control of power factor correcting boost converter without instantaneous measurement of input current," *IEEE Trans. Power Electron*., vol. 10, no. 4, pp. 435-445, Jul. 1995.

[61] V.M Rao, A.K. Jain, K.K Reddy and A. Behal, "Experimental Comparison of Digital Implementations of Single-Phase PFC Controllers," *IEEE Trans. Ind. Electron*., vol. 55, no. 1, pp. 67-78, Jan. 2008.

[62] Recommended Practices and Requirements of Harmonic Control in Electrical Power Systems, IEEE Std. 519-1992, 1994

[63] S.B. Kjaer, J.K. Pedersen and F. Blaabjerg, "A review of single-phase grid-connected inverters for photovoltaic modules," *IEEE Trans. Ind. Appl.*, vol. 41, no. 5, pp. 1292-1306, Sep./Oct. 2005.

[64] Yaosuo Xue, Liuchen Chang, Sren Baekhj Kjaer, J. Bordonau and T. Shimizu, "Topologies of single-phase inverters for small distributed power generators: an overview," *IEEE Trans. Power Electron.*, vol. 19, no. 5, pp. 1305-1314, Sep. 2004.

[65] K.A. Kim, S. Lertburapa, Chenyang Xu and P.T. Krein, "Efficiency and cost trade-offs for designing module integrated converter photovoltaic systems," *in Proc. IEEE PECI*, 2012, pp. 1-7.

[66] R.W. Erickson and A.P. Rogers, "A Microinverter for Building-Integrated Photovoltaics," in *Proc. Annu. IEEE Appl. Power Electron. Conf.*, 2009, pp. 911-917.

[67] C. Trujillo Rodriguez, D. Velasco de la Fuente, G. Garcera, E. Figueres and J.A. Guacaneme Moreno, "Reconfigurable Control Scheme for a PV Microinverter Working in Both Grid-Connected and Island Modes," *IEEE Trans. Ind. Electron.*, vol. 60, no. 4, pp. 1582-1595, Apr. 2013.

[68] R.D. Middlebrook, "Small-signal modeling of pulse-width modulated switched-mode power converters," *Proc. IEEE*, vol. 76, no. 4, pp. 343-354, Apr. 1988.

[69] N. Mohan, W.P. Robbins, T.M. Undeland, R. Nilssen and O. Mo, "Simulation of power electronic and motion control systems-an overview," *Proc. IEEE*, vol. 82, no. 8, pp.1287-1302, Aug. 1994.

[70] D. Maksimovic, A. M. Stankovic, V. J. Thottuveil, and G. C. Verghese, "Modeling and simulation of power electronic converters," *Proc. IEEE*, vol. 89, no. 6, pp. 898–912, Jun. 2001.

[71] Jian Sun, D.M. Mitchell, M.F. Greuel, P.T. Krein and R.M. Bass, "Averaged modeling of PWM converters operating in discontinuous conduction mode," *IEEE Trans. Power Electron.*, vol. 16, no. 4, pp. 482-492, Jul. 2001.

[72] A. Davoudi and J. Jatskevich, "Parasitics Realization in State-Space Average-Value Modeling of PWM DC–DC Converters Using an Equal Area Method," *IEEE Trans. Circuits Syst. I, Reg. Papers*, vol. 54, no. 9, pp. 1960-1967, Sep. 2007.

[73] V. Vorperian,"Simplified analysis of PWM converters using the model of PWM switches, Part I: Continuous conduction mode," *IEEE Trans. Aerosp. Electron. Syst*., vol. AES-26, pp. 490–496, May 1990.

[74] E. van Dijk, J.N. Spruijt, D.M. O'Sullivan, and J.B. Klaassens, "PWM-switch modeling of DC-DC converters," *IEEE Trans. Power Electron.*, vol. 10, no. 6, pp. 659-665, Nov. 1995.

[75] Robert W. Erickson and Dragan Maksimovic. *Fundamentals of power electronics*. Springer, 2001.

[76] A. Emadi, "Modeling and analysis of multiconverter DC power electronic systems using the generalized state-space averaging method," *IEEE Trans. Ind. Electron*, vol. 51, no. 3, pp.661-668, Jun. 2004.

[77] T. Suntio, "Unified average and small-signal modeling of direct-on-time control," *IEEE Trans. Ind. Electron*, vol. 53, no. 1, pp.287-295, Feb. 2006.

[78] A. Davoudi, J. Jatskevich and T. De Rybel, "Numerical state-space average-value modeling of PWM DC-DC converters operating in DCM and CCM," *IEEE Trans. Power Electron.*, vol. 21, no. 4, pp. 1003-1012, Jul. 2006.

[79] A. Abramovitz, "An Approach to Average Modeling and Simulation of Switch-Mode Systems," *IEEE Trans. Education*, vol. 54, no. 3, pp. 509-517, Aug. 2011.

[80] F.H. Dupont, C. Rech, R. Gules and J.R. Pinheiro, "Reduced-Order Model and Control Approach for the Boost Converter With a Voltage Multiplier Cell," *IEEE Trans. Power Electron.*, vol. 28, no. 7, pp. 3395-3404, Jul. 2013.

[81] P.T. Krein, J. Bentsman, Richard M. Bass and B.C. Lesieutre, "On the use of averaging for the analysis of power electronic systems," *IEEE Trans. Power Electron.*, vol. 5, no. 2, pp.182-190, Apr. 1990.

[82] A. Emadi, "Modeling of power electronic loads in AC distribution systems using the generalized State-space averaging method," *IEEE Trans. Ind. Electron*, vol. 51, no. 5, pp.992-1000, Oct. 2004.

[83] M.Y. Bina and A. K S Bhat, "Averaging Technique for the Modeling of STATCOM and Active Filters," *IEEE Trans. Power Electron.*, vol. 23, no. 2, pp. 723-734, Mar. 2008.

[84] E. Figueres, G. Garcera, J. Sandia, F. Gonzalez-Espin and J.C. Rubio, "Sensitivity Study of the Dynamics of Three-Phase Photovoltaic Inverters With an LCL Grid Filter," *IEEE Trans. Ind. Electron.*, vol. 56, no. 3, pp.706-717, Mar. 2009.

[85] D. Meneses, F. Blaabjerg, O. García and J.A. Cobos, "Review and Comparison of Step-Up Transformerless Topologies for Photovoltaic AC-Module Application," *IEEE Trans. Power Electron.*, vol. 28, no. 6, pp. 2649-2663, Jun. 2013.

[86] Chihchiang Hua, Jongrong Lin and Chihming Shen, "Implementation of a DSP-controlled photovoltaic system with peak power tracking," *IEEE Trans. Ind. Electron.*, vol. 45, no. 1, pp. 99-107, Feb 1998.

[87] C. Rodriguez and G.A.J. Amaratunga, "Analytic Solution to the Photo-voltaic Maximum Power Point Problem," *IEEE Trans. Circuits Syst. I, Reg. Papers* , vol. 54, no. 9, pp. 2054-2060, Sep. 2007.

[88] Y. Riffonneau, S. Bacha, F. Barruel and S. Ploix, "Optimal Power Flow Management for Grid Connected PV Systems With Batteries," *IEEE Trans. Sustainable Energy*, vol.2, no.3, pp.309-320, July 2011.

[89] W.A. Omran, M. Kazerani and M.M.A. Salama, "Investigation of Methods for Reduction of Power Fluctuations Generated From Large Grid-Connected Photovoltaic Systems," *IEEE Trans. Energy. Conv.*, vol.26, no.1, pp.318-327, March 2011.

[90] Blaabjerg, F.; Teodorescu, R.; Liserre, M.; Timbus, A.V.; , "Overview of Control and Grid Synchronization for Distributed Power Generation Systems," *IEEE Trans. Ind. Electron.*, vol.53, no.5, pp.1398-1409, Oct. 2006.

[91] Chen Zhe; J.M. Guerrero and F. Blaabjerg, "A Review of the State of the Art of Power Electronics for Wind Turbines," *IEEE Trans. Power Electron.*, vol.24, no.8, pp.1859-1875, Aug. 2009.

[92] E. Serban and H. Serban, "A Control Strategy for a Distributed Power Generation Microgrid Application With Voltage- and Current-Controlled Source Converter," *IEEE Trans. Power Electron.*, vol.25, no.12, pp.2981-2992, Dec. 2010.

[93] T. Esram and P.L. Chapman, "Comparison of Photovoltaic Array Maximum Power Point Tracking Techniques," *IEEE Trans. Energy. Conv.*, vol.22, no.2, pp.439-449, June 2007.

[94] S. Jain and V. Agarwal, "Comparison of the performance of maximum power point tracking schemes applied to single-stage grid-connected photovoltaic systems," *IET Elec. Power Appl.*, vol.1, no.5, pp.753-762, Sep. 2007.

[95] R. Gules, J. De Pellegrin Pacheco, H.L. Hey and J. Imhoff, "A Maximum Power Point Tracking System With Parallel Connection for PV Stand-Alone Applications," *IEEE Trans. Ind. Electron.*, vol.55, no.7, pp.2674-2683, July 2008.

[96] S. Kuszmaul, S. Gonzalez, A. Ellis and E. Serban, "Commanding inverters to establish coordinated μgrid functionality at Sandia National Laboratories," *Proc. IEEE 34th IEEE Photovoltaic Spec.* Conf., pp. 1513–1518, Jun. 2009.

[97] Lin Ma, Kai Sun, R. Teodorescu, J.M. Guerrero, and Xinmin Jin, "An integrated multifunction DC/DC converter for PV generation systems," *Industrial Electronics (ISIE),* pp.2205-2210, Jul. 2010.

[98] Monfared, M.; Sanatkar, M.; Golestan, S., "Direct active and reactive power control of single-phase grid-tie converters," *IET Power Electron.*, vol.5, no.8, pp.1544-1550, Sep. 2012.

[99] S.K. Mazumder, R.K. Burra, Rongjun Huang, M. Tahir, and K. Acharya, "A Universal Grid-Connected Fuel-Cell Inverter for Residential Application," *IEEE Trans. Ind. Electron.*, vol.57, no.10, pp.3431-3447, Oct. 2010.

[100] P.T. Krein, R.S. Balog, and Xin Geng, "High-frequency link inverter for fuel cells based on multiple-carrier PWM," *IEEE Trans. Power Electron.*, vol.19, no.5, pp. 1279-1288, Sep. 2004.

[101] Khajehoddin, S.A.; Karimi-Ghartemani, M.; Bakhshai, A.; Jain, P., "A Power Control Method With Simple Structure and Fast Dynamic Response for Single-Phase Grid-Connected DG Systems," *IEEE Trans. Power Electron.*, vol.28, no.1, pp.221,233, Jan. 2013.

[102] S. Samerchur, S. Premrudeepreechacharn,Y. Kumsuwun, and K. Higuchi, "Power control of single-phase voltage source inverter for grid-connected photovoltaic systems," *IEEE/PES Power Systems Conference and Exposition (PSCE*), pp.1-6, Mar. 2011.

[103] R.M. Santos Filho, P.F. Seixas, P.C Cortizo, L. A B Torres, and A.F. Souza, "Comparison of Three Single-Phase PLL Algorithms for UPS Applications," *IEEE Trans. Ind. Electron.*, vol. 55, no. 8, pp.2923-2932, Aug. 2008.

[104] S. Golestan, M. Monfared, F.D. Freijedo, and J.M. Guerrero, "Design and Tuning of a Modified Power-Based PLL for Single-Phase Grid-Connected Power Conditioning Systems," *IEEE Trans. Power Electron.*, vol. 27, no. 8, pp.3639-3650, Aug. 2012.

[105] D. Yazdani, A. Bakhshai, and P.K. Jain, "Grid synchronization techniques for converter interfaced distributed generation systems," *IEEE Energy Conversion Congress and Exposition*, pp.2007-2014, Sep. 2009.

[106] Zhihong Ye, A. Kolwalkar, Y. Zhang, Pengwei Du and R. Walling, "Evaluation of anti-islanding schemes based on nondetection zone concept," *IEEE Trans. Power Electron.*, vol. 19, no. 5, pp.1171-1176, Sep. 2004.

[107] V. John, Zhihong Ye and A. Kolwalkar, "Investigation of anti-islanding protection of power converter based distributed generators using frequency domain analysis," *IEEE Trans. Power Electron.*, vol. 19, no. 5, pp.1177-1183, Sep. 2004.

[108] R.S. Kunte, and Wenzhong Gao, "Comparison and review of islanding detection techniques for distributed energy resources," *Power Symposium (40th North American),* pp.1-8, Sep. 2008.

[109] D. Velasco, C. Trujillo, G Garcera, and E. Figueres, "An Active Anti-Islanding Method Based on Phase-PLL Perturbation," *IEEE Trans. Power Electron.*, vol. 26, no. 4, pp.1056-1066, Apr. 2011.

[110] A. Yafaoui, Wu Bin, and S. Kouro, "Improved Active Frequency Drift Anti-islanding Detection Method for Grid Connected Photovoltaic Systems," *IEEE Trans. Power Electron.*, vol.27, no.5, pp.2367-2375, May 2012.

[111] F. Liu, Y. Kang, Y. Zhang, S. Duan, and X. Lin, "Improved SMS islanding detection method for grid-connected converters," *IET Renewable Power Generation*, vol. 4, no. 1, pp.36-42, Jan. 2010.

[112] R.F. Arritt and R.C. Dugan, "Distribution System Analysis and the Future Smart Grid," *IEEE Trans. Ind. Appl.*, vol.47, no.6, pp.2343-2350, Nov.-Dec. 2011.

[113] V.C Gungor, D. Sahin, T. Kocak, S. Ergut, C. Buccella, C. Cecati, and G.P. Hancke, "Smart Grid Technologies: Communication Technologies and Standards," *IEEE Trans. Ind. Informatics,* vol. 7, no. 4, pp.529-539, Nov. 2011.

[114] G. Venkataramanan and C. Marnay, "A larger role for microgrids," *IEEE Power and Energy Magazine,* vol. 6, no. 3, pp.78-82, May-June 2008.

[115] R.H. Lasseter, J.H. Eto, B. Schenkman, J. Stevens, H. Vollkommer, D. Klapp, E. Linton, H. Hurtado, and J. Roy, "CERTS Microgrid Laboratory Test Bed," *IEEE Trans. Power Delivery*, vol. 26, no. 1, pp.325-332, Jan. 2011.

This page internationally left blank.